Ocean Acoustic Uncertainty for Submarine Applications

by

Matthew Michael Swezey

B.S., United States Naval Academy (2009)

Submitted to the Department of Mechanical Engineering
in partial fulfillment of the requirements for the degrees of

Master of Naval Architecture and Marine Engineering

and

Master of Mechanical Engineering

at the

MASSACHUSETTS INSTITUTE OF TECHNOLOGY

June 2016

Author .....
Department of Mechanical Engineering
May 18, 2016

Certified by .....
Dr. Pierre F. J. Lermusiaux
Associate Professor
Thesis Supervisor

Accepted by Rohan Abeyaratne .....
Dr. Rohan Abeyaratne
Chairman, Committee on Graduate Students

Ocean Acoustic Uncertainty for Submarine Applications

by

Matthew Michael Swezey

Submitted to the Department of Mechanical Engineering
on May 18, 2016, in partial fulfillment of the
requirements for the degrees of
Master of Naval Architecture and Marine Engineering
and
Master of Mechanical Engineering

Abstract

The focus of this research is to study the uncertainties forecast by multi-resolution ocean models and quantify how those uncertainties affect the pressure fields estimated by coupled ocean models. The quantified uncertainty can then be used to provide enhanced sonar performance predictions for tactical decision aides.

High fidelity robust modeling of the oceans can resolve various scale processes from tidal shifts to mesoscale phenomena. These ocean models can be coupled with acoustic models that account for variations in the ocean environment and complex bathymetry to yield accurate acoustic field representations that are both range and time independent. Utilizing the MIT Multidisciplinary Environmental Assimilation System (MSEAS) implicit two-way nested primitive-equation ocean model and Error Subspace Statistical Estimation scheme (ESSE), coupled with three-dimensional-in-space (3D) parabolic equation acoustic models, we conduct a study to understand and determine the effects of ocean state uncertainty on the acoustic transmission loss.

The region of study is focused on the ocean waters surrounding Taiwan in the East China Sea. This region contains complex ocean dynamics and topography along the critical shelf-break region where the ocean acoustic interaction is driven by several uncertainties. The resulting ocean acoustic uncertainty is modeled and analyzed to quantify sonar performance and uncertainty characteristics with respect to submarine counter detection. Utilizing cluster based data analysis techniques, the relationship between the resulting acoustic field and the uncertainty in the ocean model can be characterized. Furthermore, the dynamic transitioning between the clustered acoustic states can be modeled as Markov processes. This analysis can be used to enhance not only submarine counter detection aides, but it may also be used for several applications to enhance understanding of the capabilities and behavior of uncertainties of acoustic systems operating in the complex ocean environment.

Thesis Supervisor: Dr. Pierre F. J. Lermusiaux
Title: Associate Professor

Acknowledgments

I would like to thank first my advisor, Professor Pierre Lermusiaux for the knowledge and guidance that he has provided me over the course of the last year and a half. I appreciate your willingness to take the time to talk me through difficult problems or serve as the sounding board for ideas. No matter how busy you were your door was always open and you always had time for the students you advised.

This thesis would not have been possible without the help of Dr. Pat Haley. Pat your expertise and advice enabled me to overcome some of most difficult hurdles I encountered during this project.

I am also grateful to Dr. Kevin Heaney and Dr. Richard Campbell of Ocean Acoustical Service and Instrumentation Systems, Inc. Dr. Campbell thank you for resolving any question I had within minutes of me asking. I enjoyed having the opportunity to learn about and use the Peregrine model and hope to see it again in the future.

It was an honor to be a part of the MSEAS group. I enjoyed our group meetings and occasional birthday celebration. Deepak, thank you for your numerous lessons and explanations. Sydney, Chris, John and Jing thanks for your support and friendship. To all the new group members; Abhinav, Arkopal, Chinmay, Corbin, Florian and Johnathan, I wish you the best of luck it has been a pleasure getting to know you and learning from you.

I am very grateful to the United States Navy for funding my education. The 2N Naval Construction and Engineering Program has provided me with an amazing opportunity to develop academically and professionally.

Finally, I would like to thank my family. Thank you, Mom and Dad for always encouraging me to pursue my academic career. To my wife, Bridget, thank you for always offering your support and patience through many long nights of studying and work. Having you by my side through our time together in Boston has been a blessing and I can not thank you enough for everything you do.

Contents

List of Figures

List of Tables

Chapter 1

Introduction

> *"We are in the midst of a computational revolution that will change science and society as dramatically as the agricultural and industrial revolution did. The discipline of computational science is significantly affecting the way we do hard and soft science. Supercomputers with ultrafast, interactive visualization peripherals have come of age and provide a mode of working that is coequal with laboratory experiments and observations and with theory and analysis. We can now grapple with nonlinear and complexly intercoupled phenomena in a relatively short time and provide insight for quantitative understanding and better prediction."* (Zabusky, 1987)

The implementation of advanced numerical methods to model the ocean acoustic environment has greatly advanced with growing computational power; however, this is not a mature field. The Multidisciplinary Simulation, Estimation, and Assimilation Systems (MSEAS) group at MIT is researching techniques to enhance and employ numerical methods that accurately model oceans systems at various scales. Accurate ocean models such as the Primitive Equation ocean model employed by the MSEAS group can be coupled with acoustic models to provide more realistic simulations of the ocean sound propagation. Examples of such coupled ocean-physics and acoustic modeling include (Colin et al., 2013, Duda et al., 2014a, 2011, 2014b, Lam et al., 2009,

Robinson and Lermusiaux, 2004, Xu et al., 2008), several of which involved coupled uncertainties (Abbot and Dyer, 2002, Emerson et al., 2015, Goff et al., 2006, Heaney and Cox, 2006, Lermusiaux et al., 2010, Lermusiaux and Chiu, 2002, Lermusiaux et al., 2002, Robinson et al., 2002).

Understanding the interaction of coupled ocean and acoustic models and being able to accurately model ocean environments, assimilate data, quantify uncertainty and describe the effects on submarine counter-detection is the ultimate goal of this thesis. First we will conduct a thorough investigation into the assumptions, physics and numerical methods employed in the MSEAS ocean modeling (Haley and Lermusiaux, 2010, Haley et al., 2015). This investigation will highlight the sources of uncertainty in the ocean modeling program. Second, a review of acoustic models that have been used in conjunction with ocean models to predict sound propagation in various ocean environments will be conducted. The acoustic model employed in this research is the Peregrine model developed by the Ocean Acoustical Services and Instrumentation Systems Inc., which features a 3D parabolic equation acoustic model (Heaney and Campbell, 2013). Finally, the uncertainty and performance predictions of the coupled MSEAS ocean model and the OASIS acoustic model will be conducted in order to realistically predict acoustic vulnerabilities. The validity of these acoustic vulnerabilities is determined by the quantification of the uncertainty of the model estimates. The advanced acoustic forecasting can be utilized in tactical decision aids for the planning of submarine operations in a variety of ocean environments.

The study requires a coupled ocean acoustic simulation in order to allow for realistic uncertainty analysis. The ocean acoustic uncertainty study will employ ocean models that have been generated during the 2008 Quantifying, Predicting and Exploiting Uncertainty study as reviewed by (Gawarkiewicz et al., 2011) and discussed in (Lermusiaux et al., 2010, Lin et al., 2010). The ocean models were forecast through the use of the MSEAS primitive equation model. Real-time data was collected during the experiment and assimilated with the ocean model in order to accurately model the ocean properties. The ocean models were perturbed several times in their initial and boundary conditions and through stochastic forcing (Lermusiaux, 2006, Rixen et al.,

2012). This process generates an ensemble of ocean states, which were each then dynamically simulated over the course of several days. The ensembles of ocean states then represent realistic dynamic ocean fields. The ocean simulation is then coupled with the Peregrine 3D parabolic equation acoustic model. The acoustic model parameters are set to ensure the resulting acoustic field uncertainties will be representative of the uncertainties due to the ocean state. An in depth 2D and 3D analysis of the resulting acoustic states will be conducted. The region of the acoustic study will be primarily focused along the dynamic shelf-break region in the waters surrounding the North Mien-Hua Canyon. This region is an area that exhibits complex ocean states and acoustic properties.

A comprehensive data analysis of the resulting acoustic fields generated from the ensemble of ocean states will be conducted. The 2D and 3D acoustic fields will be analyzed using a cluster based reduced order modeling technique (Kaiser et al., 2014, Östh et al., 2015). The data will be first clustered using a k-means analysis to reduce the number of representative states. The time series of cluster transitions will then be modeled as a Markov process. The variation in the acoustic field due to the uncertainties in the ocean state can be used to provide information which can be incorporated into the probability of detection plots used for a counter-detection tactical decision aid. The ocean acoustic uncertainty analysis employed here in the dynamic shelf break region can be used to provide increased fidelity and understanding for a number of applications.

1.1 Motivation

The capabilities of the undersea forces are derived from developments that originated to counter a different adversary then they face today. The current platforms and systems were designed for open ocean operations. The focus of operations has shifted from deep water to the littorals. The littoral regions contain new and evolving threats including modern quiet platforms and threats due to the proliferation of technology. The littoral regions pose challenging problems due to complex sound propagation,

high vessel traffic, and closer proximity to adversaries. Asymmetric threats can be countered with the employment of increased computing power and networks to improve situational awareness of the battle-space. Sensors and networks will enable command and control of multiple platforms and vehicles (Task Force, 2004). The ability to plan and coordinate off-ship sensors and vehicles requires a high fidelity picture of the environmental features effecting acoustic propagation.

Anti-Submarine warfare effectiveness is determined by the ability to detect, classify, target and attack a threat and survive a counterattack. Additionally, it may be necessary to avoid detection all together in order to prevent hostilities. Tactical control of these situations is achieved by the integration and understanding of the environmental features, the ship status and threats in the region. The fusion of data from off hull support and organic sensors can be integrated effectively to provide a more robust tactical picture for the operators to navigate through complex situations. The ability to exploit environmental features to hide from or detect threats will impact future operations. Responsive mission planning and in situ analysis of the acoustic environment is crucial especially as the threat environment is drastically changing due to unmanned systems and sensors.

The shift in the dynamics of the undersea domain places a greater importance on stealth. The radiated noise from a vessel can be detected if it exceeds the background noise level present in the environment. The background noise level is affected by ambient noise in the ocean, noise generated by ocean traffic, or biological noise. The radiated noise can vary over a range of magnitudes and is therefore measured by pressure level intensity (Crocker, 1998).

$$\mathrm{dB} = 20 \log \left(\frac{p}{p_{ref}} \right) \tag{1.1}$$

The radiated noise is expressed as decibels relative to 1 micropascal at 1 yard for spherical spreading. The radiated noise from a vessel is referred to as the ship's signature. The ship's signature is dependent on platform and varies over the course of the vessels life. The ship signature must be constantly monitored and to maintain

stealth and understand the tactical implications of the signature. The ability to detect a vessel acoustically is based on the signal to noise ratio of the radiated noise. The passive sonar equation is used to describe this ratio, which is also referred to as the detection threshold is displayed in Equation 1.2 (Kuperman and Roux, 2007). The variables of this equation are described in Table 1.1.

Table 1.1: Passive Sonar Equation

Variable	Description
SNR	Signal to Noise Ratio (dB)
SL	Source Level - Radiated Noise
TL	Transmission Loss (Absorbtion, Scattering, Spreading)
NL	Noise Level (Ambient and Self Noise)
DI	Directivity Index (Sensitivity of Receiver)

$$\text{SNR} = \text{SL - TL - (NL - DI)} \tag{1.2}$$

The acoustic signature requirements must be taken into account during the design phase of undersea vehicles to minimize the probability of detection. Additionally, throughout the course of the vessels life the baseline radiated noise can fluctuate and must be monitored to understand the change in the signal to noise ratio. Various operations and evolutions can also produce high levels of radiated noise. In order to operate in a tactically prudent manner knowledge of the environment and the acoustic propagation is vital to understand.

The accurate prediction of uncertainties in the ocean environment can provide significant insight into the potential acoustic field characteristics (Lermusiaux et al., 2006). This knowledge could display a greatly increased or decreased vulnerability to detection, which would be useful tactical information for planning purposes. The focus of this study along the shallow water shelf break region of the littorals is an area of increasing significance and the dynamics of this region are complex. The quantification and display of this ocean and acoustic uncertainty can provide the operator useful information necessary for operating in this complex region.

Chapter 2

Ocean Modeling Background

2.1 Ocean Modeling

The ocean is a complex medium for sound propagation. The sound speed in the ocean is predominantly driven by the density of the seawater, which varies with pressure, temperature and salinity. The fluctuations of these parameters with time, whether that is a daily or seasonal change further complicates ocean modeling. Additionally, Mesoscale effects such as currents and internal waves can also have a large impact on the acoustical environment (Jensen et al., 2011). The range of ocean modeling processes can be seen in Table 2.1 with the respective time scale of each process. The major Pacific Gyres are illustrated in Figure 2-1 for reference.

Ocean acoustic model complexity is increased due to the multiple effects that

Table 2.1: Ocean Processes

Process	Time Scale
Turbulence	Seconds
Internal Waves	Minutes
Tides	Hours
Fronts	Days
Eddies	Weeks
Currents	Seasons
Gyres	Years

take place along the boundary. At the upper boundary near the surface waves and thermal layers develop. At the lower boundary various geographic features exhibit vastly differing acoustic characteristics. In the ever changing ocean environment a dynamic model is required to forecast the state of these variables.

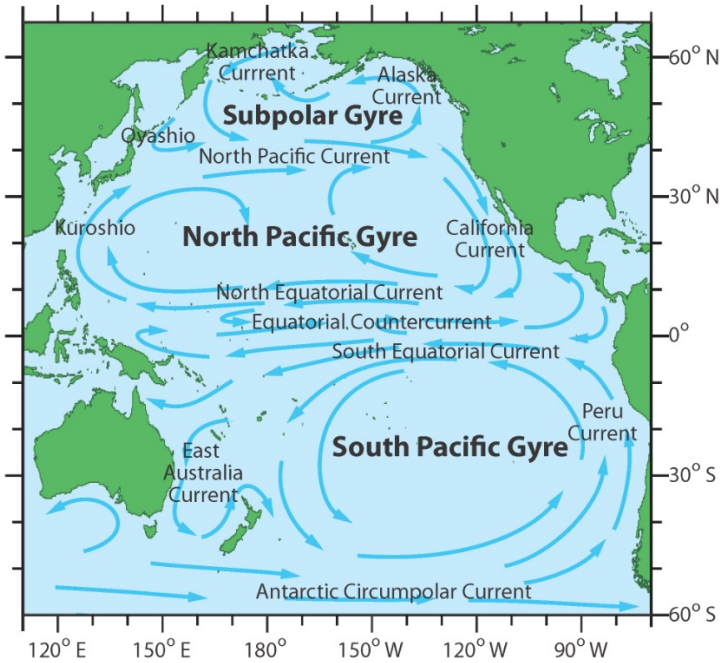

Figure 2-1: Pacific Ocean Gyres (Byfield, 2016)

The ocean environment is defined by several nonlinear interactions driven by complex bathymetry and boundary effects. To accurately model this dynamic environment a powerful numerical scheme is required to capture these effects across various scales. The governing equations for ocean modeling are derived from the Navier-Stokes Equations. These equations support acoustic modes and nonlinearities, which requires simplifications to make the equations tractable for solving numerically across longer time scales. The simplifications to these equations can be made without significantly affecting accuracy in order to reduce the computational cost when employing these equations. The resulting equations are the primitive equations, which are the basis for most fluid circulation models.

2.1.1 Primitive Equations

The MSEAS Primitive Equation Ocean Model is derived from the Navier-Stokes equation with hydrostatic and Boussinesq approximations. The Primitive Equations combine the conservation of mass, conservation of momentum equations, equations of state and energy equations and are displayed below. These equations govern the velocity, density, pressure, temperature and salinity of the ocean and are summarized in the following sections. This ocean model is capable of generating high fidelity realizations of the ocean environment (Haley and Lermusiaux, 2010).

$$\text{Conservation of Mass: } \nabla \cdot u + \frac{\partial w}{\partial z} = 0 \tag{2.1}$$

$$\text{Conservation of Horizontal Momentum: } \frac{Du}{Dt} + f\hat{k} \times u = -\frac{1}{\rho_0}\nabla p + F \tag{2.2}$$

$$\text{Conservation of Vertical Momentum: } \frac{\partial p}{\partial z} = -\rho g \tag{2.3}$$

$$\text{Conservation of Heat: } \frac{DT}{Dt} = F^T \tag{2.4}$$

$$\text{Conservation of Salt: } \frac{DS}{Dt} = F^S \tag{2.5}$$

$$\text{Equation of State: } \rho = \rho(z, T, S) \tag{2.6}$$

2.1.2 Conservation of Mass

For ocean modeling a necessary condition that must be satisfied is that mass must be conserved. The continuity equation is the partial differential equation for the conservation of mass.

$$\frac{\partial \rho}{\partial t} + \frac{\partial}{\partial x}(\rho u) + \frac{\partial}{\partial y}(\rho v) + \frac{\partial}{\partial z}(\rho w) = 0 \tag{2.7}$$

$$\frac{\partial \rho}{\partial t} + \nabla \cdot (\rho \mathbf{U}) = 0 \tag{2.8}$$

If an acoustic source is located within the infinitesimal volume then a source term would be added to this equation, which is used for acoustic modeling (Ziomek, 1994).

$$\frac{\partial \rho}{\partial t} + \nabla \cdot (\rho \mathbf{U}) = \rho Q \tag{2.9}$$

2.1.3 Momentum Equations

The governing equations for fluid flows are the momentum equations in the x, y, and z directions in the Cartesian coordinate system. Derived from Newtons equations of motion the momentum equations with a modified acceleration term due to Earth's rotation represent the Navier-Stokes equations for ocean flow (Cushman-Roisin and Beckers, 2011).

$$\sum F = ma = \rho \mathrm{V} a \tag{2.10}$$

$$\rho a = \frac{\sum F}{\mathrm{V}} \tag{2.11}$$

$$x : \rho\Big(\frac{du}{dt} + f_* w - f v\Big) = -\frac{\partial p}{\partial x} + \frac{\partial \tau^{xx}}{\partial x} + \frac{\partial \tau^{xy}}{\partial y} + \frac{\partial \tau^{xz}}{\partial z} \tag{2.12}$$

$$y : \rho\Big(\frac{dw}{dt} + f u\Big) = -\frac{\partial p}{\partial y} + \frac{\partial \tau^{yx}}{\partial x} + \frac{\partial \tau^{yy}}{\partial y} + \frac{\partial \tau^{yz}}{\partial z} \tag{2.13}$$

$$z : \rho\Big(\frac{dw}{dt} - f_* u\Big) = -\frac{\partial p}{\partial z} - \rho g + \frac{\partial \tau^{zx}}{\partial x} + \frac{\partial \tau^{zy}}{\partial y} + \frac{\partial \tau^{zz}}{\partial z} \tag{2.14}$$

Coriolis Parameter

The Earth is an oblate spheroid that revolves about its axis, which drives the ocean movement. Mesoscale phenomena such as ocean currents and tides are inherently affected by the rotation of the earth. The effects of this rotation are mathematically accounted for in an earth fixed rotating reference frame by the Coriolis term, which appears in Equations (2.12, 2.13, 2.14). The absolute velocity of the fluid is simply the sum of the rotation of the reference frame and the relative velocity (Cushman-

Roisin and Beckers, 2011). The unit vectors of the fixed and rotating reference frames

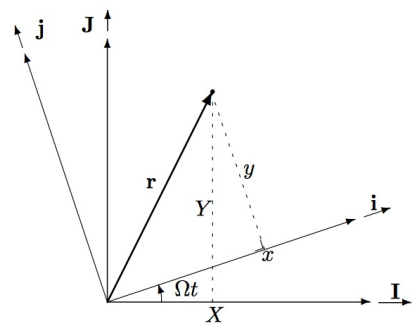

Figure 2-2: Rotating Frame of Reference (Cushman-Roisin and Beckers, 2011)

can be related with the following equations:

$$I = \mathrm{i}\cos\Omega t - \mathrm{j}\sin\Omega t \tag{2.15}$$

$$J = \mathrm{i}\sin\Omega t + \mathrm{j}\cos\Omega t \tag{2.16}$$

$$\Omega = \frac{2\pi}{T} \tag{2.17}$$

To correctly account for the relative change of the coordinates with respect to the rotating frame and the rotation of the absolute frame, the relative velocity and absolute velocity in the inertial reference frame must be determined.

$$x = X\cos\Omega t + Y\sin\Omega t \tag{2.18}$$

$$y = -X\sin\Omega t + Y\cos\Omega t \tag{2.19}$$

The relative and absolute velocities are related with the following equalities:

$$\text{Relative Velocity: } \mathbf{u} = \frac{dx}{dt}\mathrm{i} + \frac{dy}{dt}\mathrm{j} = u\mathrm{i} + v\mathrm{j} \tag{2.20}$$

$$\text{Absolute Velocity: } \mathbf{U} = \frac{dX}{dt}\mathrm{I} + \frac{dY}{dt}\mathrm{J} = U\mathrm{i} + V\mathrm{j} \tag{2.21}$$

The relative and absolute accelerations can be reduced to the subsequent equations.

$$\mathbf{a} = \frac{d^2x}{dt^2}\mathrm{i} + \frac{d^2y}{dt^2}\mathrm{j} = \frac{du}{dt}\mathrm{i} + \frac{dv}{dt}\mathrm{j} = a\mathrm{i} + b\mathrm{j} \tag{2.22}$$

$$\mathbf{A} = \frac{d^2X}{dt^2}\mathrm{I} + \frac{d^2Y}{dt^2}\mathrm{J} = \left(\frac{d^2X}{dt^2}\cos\Omega t + \frac{d^2Y}{dt^2}\sin\Omega t\right)\mathrm{i} + \left(\frac{d^2Y}{dt^2}\cos\Omega t - \frac{d^2X}{dt^2}\sin\Omega t\right)\mathrm{j} \tag{2.23}$$

which can be simplified to the subsequent relations.

$$\mathbf{A} = A\mathrm{i} + B\mathrm{j} \tag{2.24}$$

$$A = a - 2\Omega v - \Omega^2 x \tag{2.25}$$

$$B = b + 2\Omega u - \Omega^2 y \tag{2.26}$$

The absolute acceleration differs from the relative by two factors the Coriolis acceleration and the centrifugal acceleration respectively. The centrifugal term can be accounted for by the gravitational acceleration, due to the oblate spheroid shape of the earth. The resultant vector of the centrifugal acceleration and the gravitational acceleration is normal to the surface of the oblate spheroid shaped Earth. Neglecting the centrifugal term and substituting the Coriolis factor $f = 2\Omega$ yields the acceleration equation.

$$\frac{du}{dt} - fv = 0 \tag{2.27}$$

$$\frac{dv}{dt} + fu = 0 \tag{2.28}$$

In 3D coordinates the Coriolis parameter is $f = 2\Omega\sin\varphi$ and the reciprocal Coriolis parameter is $f_* = 2\Omega\cos\varphi$, where φ represents the latitude. The components of the acceleration; therefore, is represented by the following equations, which are applied in the momentum equations:

$$A_x : \frac{du}{dt} + 2\Omega\cos\varphi w - 2\Omega\sin\varphi v = \frac{du}{dt} + f_* w - fv \tag{2.29}$$

$$A_y : \frac{dv}{dt} + 2\Omega \sin\varphi u = \frac{dv}{dt} + fu \tag{2.30}$$

$$A_z : \frac{dw}{dt} - 2\Omega \cos\varphi u = \frac{dw}{dt} - f_* u \tag{2.31}$$

2.1.4 Equations of State

Equations of state are utilized to describe the changing density used in the momentum equations. In the ocean environment the density of seawater is affected by pressure, temperature and salinity. The density of seawater is inversely proportional to the local temperature and proportional to the salinity content and depth. Salinity concentrations can exhibit large variations near river outlets and sea ice interfaces,, which can have substantial effects on density. The equation of state used in the primitive equations is a function of depth, temperature and salinity.

$$\rho = \rho(z, T, S) \tag{2.32}$$

If the assumption of incompressibility is used then the depth can be neglected and the factors of temperature and salinity can describe the density.

$$\rho = \rho_0[1 - \alpha_T(T - T_0) + \beta_S(S - S_0)] \tag{2.33}$$

Where α_T and β_S are the coefficients of expansion and contraction respectively (Griffies and Adcroft, 2008).

$$\alpha_T = -\left(\frac{\partial ln\rho}{\partial T}\right)_{p,S} \tag{2.34}$$

$$\beta_S = -\left(\frac{\partial ln\rho}{\partial S}\right)_{p,T} \tag{2.35}$$

Since the temperature and salinity variables have been introduced additional equations must be used. The local salinity content in the ocean is conserved and varies based on the diffusion effects. The diffusive processes are governed by the equation

below (Haley and Lermusiaux, 2010).

$$\frac{DS}{Dt} = F^s \tag{2.36}$$

F^s represents the diffusive processes that take place on the sub grid scale.

2.1.5 Energy Equations

The equation used to account for the temperature variable is the conservation of energy. The ocean is not a closed system and energy is transferred through evaporative and dissipative effects.

$$\frac{De}{Dt} = C_v \frac{DT}{Dt} = Q - W = \left(\frac{k_T}{\rho}\nabla^2 T\right) - \left(p\frac{D\frac{1}{\rho}}{Dt}\right) \tag{2.37}$$

This equation can be reduced under the assumption of conservation of mass to equation 2.38 (Cushman-Roisin and Beckers, 2011).

$$\rho C_v \frac{DT}{Dt} = k_T \nabla^2 T \tag{2.38}$$

Similar to the salinity budget the energy budget is represented by sub grid scale processes F^T for the primitive equation model (Haley and Lermusiaux, 2010).

$$\frac{DT}{Dt} = F^T \tag{2.39}$$

2.1.6 Boussinesq Approximation

In order to simplify the previous governing equations for ocean flow the Boussinesq approximations are made. The Boussinesq approximations are based on the fact that the fluid density of the ocean does not vary significantly from a mean value.

$$\rho' << \bar{\rho} \tag{2.40}$$

Due to the small fluctuations in density it can be assumed that the horizontal momentum equations can be simplified and reduced to the following equation.

$$\frac{D\mathbf{u}}{Dt} + f\hat{k} \times \mathbf{u} = -\frac{1}{\rho_0}\nabla p + \nu\nabla^2\mathbf{u} \tag{2.41}$$

2.2 Ocean Modeling Uncertainty

Due to the size and dynamics of the ocean an exact deterministic representation across all scales is not possible. As shown in Table 2.1 there are a number of scale processes that occur simultaneously and their interactions are nonlinear. The simplifications necessary to enable modeling of the ocean that represent these processes introduce uncertainty. Uncertainty can be represented by a probability density function of the possible deviations of the estimated field from the actual field.

The sources of uncertainty in ocean modeling are a result of several factors. The limited temporal and spatial scale dictates which processes will be modeled mathematically and the unknown characteristics of these ocean processes introduce uncertainties (Nihoul and Djenidi, 1998). The ocean data measurements are limited and the initial starting ocean field is uncertain. Boundary conditions, whether that is the sea-atmosphere interface or the bathymetry are also uncertain and can influence the resulting field. Additionally, numerical errors inherent in mathematical models are present (Lermusiaux et al., 2006). Finally, the exact ocean field is unknown due to the size of the ocean and the complexity of obtaining accurate measurements. Therefore, the real and unknown ocean field varies from the ocean field that is generated through the approximate mathematical model. The use of ocean measurements can be assimilated with the models to reduce the degree of uncertainty (Lermusiaux, 2006). This method enables dynamical models to increase their fidelity by incorporating data measurements that are weighted inversely with respect to the relative error of the measured data (Robinson and Lermusiaux, 2002). Data assimilation provides estimates that are more accurate than a model or measurements can produce individually.

Data assimilation and uncertainty quantification techniques are a growing field that are essential for improving ocean modeling. Deterministic models that output the same result for a given input are useful for modeling well understood processes. However, when the input fields or model processes are not well known stochastic models can be employed to account for this variability. Stochastic models can represent more comprehensively processes that are not captured by deterministic models. Methods of accounting for these uncertainties include introducing variability into the input parameters. Substantial work has been done in the field of incorporating the effects of uncertainty in the input parameters for stochastic processes. Monte Carlo simulations, although computationally expensive and inefficient, have been employed to model the stochasticity of input parameters. Furthermore, advanced methods such as the generalized Polynomial Chaos method (Ghanem and Spanos, 1991, Xiu and Karniadakis, 2002), and Proper Orthogonal Decomposition methods have been employed (Berkooz et al., 1993, Gay and Ray, 1995). This method of representing the variability solely within the input parameters can fail to represent the full variability across multiple processes if those processes are changing across differing time frames.

One method that has been employed to capture the uncertainty of a system is the Error Subspace Statistical Estimation (ESSE) scheme. The ESSE scheme is used to determine an error subspace that evolves in time and space and tracks the dominant error fields that can be used for nonlinear data assimilation, filtering and smoothing based on an ensemble of Monte Carlo forecasts. The error subspace is a determined though a singular decomposition of the error covariance matrix (Lermusiaux and Robinson, 1999). This method was used to perform efficient real time data assimilation for North Atlantic Treaty Organization (NATO) operations in the Strait of Sicily and simulations in the Levantine intermediate waters (Lermusiaux, 1997). In order to model the evolution of uncertainty stochastic partial differential equations can also be employed. External stochastic forcing is modeled by modifying the governing dynamical equation of the system to include stochastic terms. A more recent advance in uncertainty quantification involves the use of dynamically orthogonal stochastic partial differential equations.

A closed set of dynamically orthogonal field equations were derived to determine the evolution of the dominant uncertainty fields of nonlinear systems that are described by stochastic partial differential equations. The equations describe the evolution of the mean field, the stochastic coefficients and the evolving deterministic orthonormal stochastic fields. The Karhunen-Loeve expansion is used to represent the time varying and dynamically evolving stochastic components (Sapsis and Lermusiaux, 2009, Ueckermann et al., 2011). The dynamically orthogonal field equations have been used to describe double gyre wind driven circulation, and lid driven cavity flow in a basin (Sapsis and Lermusiaux, 2012).

The ocean models developed using the MSEAS ocean model employ stochastic forcing and enhanced data assimilation techniques to represent multi-scale ocean processes. These high fidelity forecast ocean models are coupled with advanced acoustic models to provide accurate forecasts of acoustic field simulations that incorporate and represent the uncertainty contained within the ocean models.

Chapter 3

Ocean Acoustic Modeling Background

3.1 Ocean Acoustic Modeling

Ocean acoustic modeling efforts began during World War II to determine sound propagation in the ocean for anti-submarine warfare operations. The fundamental equation that was used then and is still used today in ocean acoustic modeling is the wave equation. A brief description and classification of the acoustic modeling techniques derived from the wave equation will be reviewed.

3.1.1 Wave Equation

The acoustic wave equation is a hyperbolic second order time dependent partial differential equation used to determine the one dimensional motion of fluid particles:

$$\nabla^2\Phi - \frac{1}{c^2}\frac{\partial^2\Phi}{\partial t^2} = 0 \tag{3.1}$$

This equation when transformed into spherical coordinates can be more easily used to represent omni-directional sounds sources in the ocean.

$$\frac{\partial^2(r\Phi)}{\partial r^2} - \frac{1}{c^2}\frac{\partial^2(r\Phi)}{\partial t^2} = 0 \tag{3.2}$$

The general solution of this differential equation yields to following equation (Crocker, 1998)

$$\Phi = \frac{1}{r} f_1(ct - r) + \frac{1}{r} f_2(ct + r) \tag{3.3}$$

This solution can be used to characterize the simple harmonic wave motion by utilizing the harmonic function below where ϕ is time independent.

$$\Phi = \phi e^{-i\omega t} \tag{3.4}$$

The hyperbolic wave equation shown above can be reduced to the elliptic wave equation, which is more commonly referred to as the Helmholtz Equation. Acoustic modeling is defined by the various applicable solutions of the Helmholtz equation. The classification of acoustic modeling techniques is dependent on the theoretical approach taken to solve the Helmholtz Equation 3.5.

$$\nabla^2 \phi + k_0^2 n^2 \phi = 0 \tag{3.5}$$

There are five standard solutions to the wave equation: ray theory, normal mode, multi-path expansion, fast field and parabolic equation techniques. The solutions can be grouped together based on there range dependence. Normal mode, multi-path expansion and fast field are all range independent, meaning that these solutions assume a homogeneous waveguide that varies only with depth. Ray theory and parabolic equation techniques assume range dependence and are better suited for complex ocean waveguides that vary with range from the source location. Therefore, both ray theory and parabolic equation techniques will be described here in further detail.

3.1.2 Ray Theory

When the fluid properties are nonuniform and changing in space and time the use of ray acoustics to quantify acoustic propagation is advantageous. When acoustic waves propagate through a varying medium the wavefront speed is not constant, which induces variance in the position of the wave front. The line normal to the wave front

is know as a ray, which is bent due to these variations of the wavefront (Jensen et al., 2011). This acoustical ray bending is analogous to the refraction of light as it travels from air to water due to the variation in the density of the medium. The fundamental equation describing rays is defined by the eikonal $\tau(x, y, z)$. The eikonal represents the surface of a wavefront, for example a constant eikonal value would describe the surface of a sphere. Solving the Helmholtz equation can be used to derive a ray equation in terms of the eikonal number (Jensen et al., 2011).

$$\nabla^2\Phi + \frac{\omega^2}{c^2(x)}\Phi = -\delta(x - x_0) \tag{3.6}$$

For ray theory it is assumed that the solution of the Helmholtz equation takes the form of the ray series as seen in Equation 3.7.

$$.\Phi(x) = e^{i\omega\tau(x)} \sum_{j=0}^{\infty} \frac{A_j(x)}{(i\omega)^j} \tag{3.7}$$

By solving the Helmholtz equation with the ray series solution and retaining only the first term in the series the eikonal equation and transport equations are derived. The eikonal equation results from grouping the $O(\omega^2)$ terms as seen in Equation 3.8.

$$|\nabla\tau|^2 = \frac{1}{c^2(x)} \tag{3.8}$$

The transport equations result from the remainder of the equations in the series (Jensen et al., 2011).

$$2\nabla\tau \cdot \nabla A_0 + (\nabla^2\tau)A_0 = 0 \tag{3.9}$$

The real terms contained in the eikonal equation describe the geometry of the rays as they travel through the waveguide and the imaginary terms contained in the transport equations describe the wave amplitudes. The ray tracing techniques are solved for a series of initial angles to determined the possible ray paths. The eigenrays that represent the path of the rays generally fall into four categories: direct path, refracted-surface reflected, refracted bottom reflected and refracted-surface-bottom reflected as

shown in Figure 3-1.

These paths can intersect and interfere constructively or destructively. To account

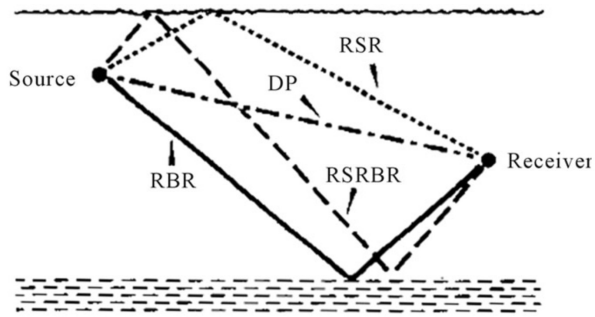

Figure 3-1: Eigenray Paths (Etter, 2013)

for multiple rays paths at a single point coherent and incoherent transmission loss calculation methods are used (Etter, 2013).

$$\text{Incoherent: TL} = -10\log\left[\sum[(\text{Re}P_i)_1^2 + (\text{Im}P_i)_1^2 + (\text{Re}P_i)_2^2 + (\text{Im}P_i)_2^2]\right] \quad (3.10)$$

$$\text{Coherent: TL} = -10\log\left[\left(\sum[(\text{Re}P_i)_1 + (\text{Re}P_i)_2]\right)^2 + \left(\sum[(\text{Im}P_i)_2 + (\text{Im}P_i)_2]\right)^2\right] \quad (3.11)$$

The ray theory techniques are computationally expensive and difficulties arise in the regions where caustics are formed by the focusing of acoustic rays. These effects can be mitigated through the use of Gaussian beam tracing techniques; however, these representations are generally utilized for only 1D and 2D models. Ray tracing techniques were used extensively in the early days of ocean acoustic research and are still used operationally today. However, these techniques have given way within the research community to the range dependent parabolic equation techniques.

3.1.3 Parabolic Equation Models

The parabolic equation method originated out of the application of the parabolic equation to radio wave propagation (Leontovich and Fock, 1946). This method was subsequently employed in the ocean acoustic field (Hardin and Tappert, 1973). The application of the parabolic wave equation has been used in 2D and 3D ocean acoustic

propagation models and its use continues to grow due to the fact that computational power has greatly increased in the recent years.

The elliptic Helmholtz equation is derived from the hyperbolic wave equation. From the Helmholtz equation the parabolic wave equation can be derived. Typically, elliptic equations describe steady state systems and hyperbolic equations are used in propagation problems varying spatially and temporally with the unknown characterized by a second order time variable resulting in an oscillating solution. The parabolic equation is employed in propagation problems that vary in space and time with the variable characterized by a first order derivative in time (Chapra and Canale, 1998). Numerical methods employed to solve the elliptic equation must be simultaneously solved in range and depth. Whereas, the parabolic equation can be efficiently solved using range marching numerical techniques allowing for more efficient solvers.

The Helmholtz equation is an elliptic equation that can be reduced in cylindrical coordinates to a parabolic equation. The following derivation is adapted from the works of (Jensen and Krol, 1975) and (Etter, 2013) and shown to provide insight into the assumptions of the resulting parabolic equation. The cylindrical Helmholtz equation can be seen in equation 3.12.

$$\frac{\partial^2 \phi}{\partial r^2} + \frac{1}{r}\frac{\partial \phi}{\partial r} + \frac{\partial^2 \phi}{\partial z^2} + k_0^2 n^2 \phi = 0 \tag{3.12}$$

One solution of the Helmholtz equation is represented by ϕ below.

$$\phi = \Psi(r, z) S(r) \tag{3.13}$$

The first and second order partial derivatives of the solution are shown in the following equations.

$$\frac{\partial(\Psi, S)}{\partial r} = S\frac{\partial \Psi}{\partial r} + \Psi\frac{\partial S}{\partial r} \tag{3.14}$$

$$\frac{\partial^2(\Psi, S)}{\partial r^2} = \left[\frac{\partial S}{\partial r}\frac{\partial \Psi}{\partial r} + S\frac{\partial^2 \Psi}{\partial r^2}\right] + \left[\frac{\partial S}{\partial r}\frac{\partial \Psi}{\partial r} + \Psi\frac{\partial^2 S}{\partial r^2}\right] \tag{3.15}$$

$$\frac{\partial(\Psi, S)}{\partial z} = S\frac{\partial \Psi}{\partial z} \tag{3.16}$$

$$\frac{\partial^2(\Psi, S)}{\partial z^2} = S\frac{\partial^2\Psi}{\partial z^2} \tag{3.17}$$

Using the separation of variables technique, plugging the partial derivatives into equation 3.12 and rearranging the following equation is obtained.

$$\Psi\left[\frac{\partial^2 S}{\partial r} + \frac{1}{r}\frac{\partial S}{\partial r}\right] + S\left[\frac{\partial^2\Psi}{\partial r^2} + \frac{\partial^2\Psi}{\partial z^2} + \left(\frac{2}{S}\frac{\partial S}{\partial r} + \frac{1}{r}\right)\frac{\partial\Psi}{\partial r} + k_0^2 n^2\Psi\right] = 0 \tag{3.18}$$

The separation constant k_0^2 is used for the left hand side of equation 3.18.

$$\left[\frac{\partial^2 S}{\partial r} + \frac{1}{r}\frac{\partial S}{\partial r}\right] = -Sk_0^2 \tag{3.19}$$

$$\frac{\partial^2 S}{\partial r} + \frac{1}{r}\frac{\partial S}{\partial r} + Sk_0^2 = 0 \tag{3.20}$$

Equation 3.20 is a zero order Bessel equation whose solution is the Hankel function of the first kind.

$$S = H_0^{(1)}(k_0 r) \tag{3.21}$$

Where the Hankel function of the first kind is defined by the relation.

$$H_0^{(1)}(k_0 r) = J_0(k_0 r) + iY_0(k_0 r) \tag{3.22}$$

Using the far field assumption that $k_0 r >> 1$ then the zero order Hankel Function of the first kind can be approximated as the following equations.

$$J_0(k_0 r) = \sqrt{\frac{2}{\pi(k_0 r)}}\cos\left((k_0 r) - \frac{\pi}{4}\right) \tag{3.23}$$

$$Y_0(k_0 r) = \sqrt{\frac{2}{\pi(k_0 r)}}\sin\left((k_0 r) - \frac{\pi}{4}\right) \tag{3.24}$$

The right hand side of equation 3.18 is now solved using the separation constant k_0^2.

$$\left[\frac{\partial^2\Psi}{\partial r^2} + \frac{\partial^2\Psi}{\partial z^2} + \left(\frac{2}{S}\frac{\partial S}{\partial r} + \frac{1}{r}\right)\frac{\partial\Psi}{\partial r} + k_0^2 n^2\Psi\right] = \Psi k_0^2 \tag{3.25}$$

Using the solution of S to find the partial derivative with respect to range $\frac{\partial S}{\partial r}$ can be determined and used to simplify equation 3.25. Substituting $\frac{\partial S}{\partial r}$ into the right hand side and using the narrow angle or paraxial approximation:

$$\frac{\partial^2 \Psi}{\partial r^2} << 2k_0 \frac{\partial \Psi}{\partial r} \tag{3.26}$$

the equation can be simplified to the narrow angle form of the parabolic wave equation.

$$\frac{\partial^2 \Psi}{\partial z^2} + 2ik_0 \frac{\partial \Psi}{\partial r} + k_0^2(n^2 - 1)\Psi = 0 \tag{3.27}$$

The primary advantage of using the parabolic form of the wave equation is that the numerical solution can be solved for using range marching schemes. The range marching scheme employed is a split-step Pade scheme. This method was first used to solve the parabolic narrow angle equation method by Tappert in 1977 (Tappert, 1977). Further improvements included using a variation of the Pade coefficients to account for wide angle propagation by Thompson and Chapman in 1983 (Thomson and Chapman, 1983). The numerical solution to this equation was advanced through the use of higher order methods that conserved energy in the Range Dependent Acoustic Model (RAM) that was developed by Collins (Collins and Westwood, 1991). These methods of solving the parabolic equation are capable of outputting the deterministic 3D acoustic field. The parabolic equation is a powerful method enabling efficient numerical methods to determine the acoustic field propagation through the complex ocean waveguide. The ocean variability is accounted for utilizing a frozen medium assumption. The input ocean field is assumed to change over a much larger time interval than is required for the acoustic energy to propagate through the medium and the small scale fluctuations in the environment are neglected. The mathematical assumptions and frozen ocean assumption generate uncertainty in the acoustic field solution. The study and development of accurate ocean acoustic models is an area of study that continues to progress to this day.

3.2 Ocean Acoustic Modeling Literature Review

The study of coupled Ocean Acoustic models has been an ongoing endeavor. Significant progress has been made with both ocean models and acoustic models in terms of accuracy and robustness. There has also been progress made in the effort to combine ocean modeling with acoustic propagation models.

The first large scale effort to integrate ocean and acoustic models was during the study of the Mid-Atlantic Bight shelfbreak region. In the 1997 Mid Atlantic Bight study data collection for ocean and acoustic modeling was integrated (Lynch et al., 1997). The Mid Atlantic Bight study involved the examination of the azimuthal coupling of the environment on the acoustic propagation. To determine the sediment properties for this exercise core samples were taken on the shelf and ocean environmental data was provided by towing a SeaSoar sensor and was used to determine slices of temperature and salinity data along given paths (Gawarkiewicz et al., 2001). For this study a 3D acoustic eigenray code was employed and compared to a 2D eigenray model. The 3D ray code used for this study was modified from the Hamiltonian Ray Tracing Program (HARPO) (Jones et al., 1986, Smith et al., 2002). Additionally, a 3D parabolic equation model was also compared. The ocean and acoustic models in this study; however, were not coupled.

Coupled ocean acoustic forecast experiments have since been performed on multiple occasions. The first of these experiments was performed in the Tyrrhenian Sea for the Focused Acoustic Forecasting exercise in 2005. This exercise utilized the Harvard Ocean Prediction System (HOPS) with Error Subspace Statistical Estimation (ESSE) for the ocean predictions. This ocean study was used to help determine optimal path planning for autonomous underwater vehicles. The acoustic program employed was the Range Dependent Acoustic Model (RAM), which was used to determine propagation paths in the littoral regions and evaluate acoustic inversion and tomography (Wang et al., 2009).

Subsequent studies have implemented coupled ocean and acoustic propagation models. These coupled systems are referred to as End-to-End systems that incorpo-

rate data assimilative models of non-linear interdisciplinary processes across multiple scales. Systems that incorporated ocean physics, sediment physics, ocean acoustic propagation and sonar systems in littoral environments are discussed in detail in review by Robinson and Lermusiaux (Lermusiaux et al., 2004). These coupled ocean acoustic forecasts employing data assimilation techniques have been performed in several at sea experiments. In 2007 real time coupled ocean acoustic forecasts were generated using data assimilative techniques for the Battlespace Preparation exercise off the coast of the island of Elba, Italy. This experiment coupled 3D ocean forecasts with 2D acoustic models to generate simulations of the ocean acoustic environment (Lam et al., 2009).

With the operational focus continuing to shift toward the littoral regions, and the expanding use of long duration autonomous vehicles the need to have accurate 3D ocean acoustic forecasts will continue to grow. The 4D ocean fields that are used in this thesis come from the data obtained during the 2008 Quantifying, Predicting and Exploiting Uncertainty (QPE 2008) exercise conducted in the regions surrounding Taiwan. The coupled ocean acoustic program used to simulate the ensemble of acoustic fields is the Peregrine model. The peregrine model is a C-language adaptation of the Range Dependent Acoustic Model that can interface with 4D ocean fields and generate Nx2D acoustic slices and fully 3D acoustic fields (Heaney and Campbell, 2013). The coupled 4D MSEAS ocean model assimilated with data obtained during the QPE 2008 exercise and 3D Peregrine acoustic model will be employed to perform an analysis of the relationship between the uncertainties in the ocean fields and the transmission of those uncertainties to the resulting acoustic field ensembles. Through the use of a cluster based analysis technique these variations will be used to provide higher fidelity probability of detection assessments along the dynamic shelfbreak region.

Chapter 4

Dynamical Cluster Analysis

Cluster-based reduced order modeling is a technique which seeks to systematically resolve complicated features of dynamical systems. Cluster-based reduced-order modeling (CROM) was first employed in the modeling of dynamic fluid mixing layers. Additionally, clustering analysis has been used in adaptive ocean sampling (Cococcioni et al., 2015). This technique is similar to the Ulam-Galerkin method, which is an approximation of the Perron-Frobenius operator (Kaiser et al., 2014). The Ulam-Galerkin method employs the process of proper orthogonal decomposition, which reduces the dimensionality of the state space through a projection method to a lower dimensional subspace. Subsequently the proper orthogonal decomposition coefficients can be represented through evolution equations to describe the dynamics of the system. Similarly, the CROM method reduces the order of dimensionality in a complex system using a clustering technique and then models the dynamic transitions between the reduced number of states. The CROM method first reduces the dimensionality of the problem through a k-means cluster analysis of an ensemble of system states. Then a Markov model is developed to describe the transitions between clustered states. Both the clustering technique and the Markov process will be explained in further detail to describe how these techniques will be applied in the ocean acoustic field analysis.

4.1 Clustering

The first component of the CROM analysis is to reduce the order of the data through clustering. Cluster analysis is a technique that has been used in data mining and machine learning. The goal of cluster analysis is to partition data into groups of similar characteristics in order to attempt to reveal structures within the data. Two relevant clustering techniques that have been used for data analysis are hierarchical clustering and k-means clustering. Hierarchical clustering algorithms group data sets into clusters based on the distance between individual observations and clusters and displays the results in a graphical dendrogram. The second method is k-means clusters which groups observations into preallocated number of clusters based on their euclidean distance from the cluster. Cluster analysis techniques have been used extensively in business and finance applications for determining market segmentation and pricing strategies (Shmueli et al., 2007). Comparatively k-means clustering is much less computationally expensive than hierarchical clustering and is typically used for large datasets. For this reason k-means clustering techniques were chosen to analyze the large ocean acoustic data sets generated by the ensemble of ocean acoustic runs.

The method of classifying clusters is through determining a distance measure d_{ij}. The distance measure is used to classify each data point, vector or matrix with p elements. The euclidean distance is a common measure for determining the distance measure.

$$d_{ij} = \sqrt{(x_{i1} - x_{j1})^2 + (x_{i2} - x_{j2})^2 + \cdots + (x_{ip} - x_{jp})^2} \tag{4.1}$$

The Euclidean distance technique measures the dissimilarity between data points that determines the centroid of each cluster as the mean of the points in each cluster. This method is highly dependent on the scale of the data and outliers can have a large effect on the analysis. Another measure that is frequently used is the similarity based correlation measure, which was employed in the the ocean acoustic analysis. The correlation measure r_{ij} is defined by the subsequent equation.

$$r_{ij} = \frac{\sum_{m=1}^{p} (x_{im} - \bar{x}_m)(x_{jm} - \bar{x}_m)}{\sqrt{\sum_{m=1}^{p} (x_{im} - \bar{x}_m)^2 \sum_{m=1}^{p} (x_{jm} - \bar{x}_m)^2}} \tag{4.2}$$

The correlation measure is related to the euclidean distance by the following relation.

$$d_{ij} = 1 - r_{ij}^2 \tag{4.3}$$

The correlation coefficient represents a similarity measure between the data points. The data points for correlation based analysis are centered, normalized to a zero mean and unit standard deviation, which is then used to determine the centroid as component wise mean of the data in the cluster. Once the distance measure is determined the k-means optimization can be computed to perform the cluster analysis.

The k-means algorithm developed originally by Lloyd in 1957 uses the designated distance measure to maximize intra-cluster similarity and minimize inter-cluster similarity (Lloyd, 1957). In order to accomplish this each dataset is placed into the group with the closest centroid and the centroids are then re-computed. This process is recursively performed until the optimization of the variance within each cluster is minimized and the variance between clusters is maximized. The cluster centroid c_k is defined by the relation (Östh et al., 2015):

$$c_k = \frac{1}{n_k} \sum_{u_m \in c_k} u_m \tag{4.4}$$

Where n_k represents the number of realizations within the each cluster and u_m is the data realization. The formula for the cluster variance J is described by the relation (Östh et al., 2015):

$$J\Big(c_1 \dots c_k\Big) = \sum_{k=1}^{K} \sum_{u_m \in c_k} ||u_m - c_k||^2 \tag{4.5}$$

For k-means analysis the optimal number of clusters must be determined. Typi-

cally, the optimal number of clusters is much smaller than the number of realizations. The clusters should also be representative of homogeneous groupings of the data set. The elbow criterion has been used in machine learning applications to determine the optimal number of clusters. This criteria is determined by comparing the cumulative sum of distances for various k-valued clusters to identify a knee in the curve. The knee in the curve would represent a point at which the optimum cluster value is most efficiently representing the dataset being evaluated. This technique is formalized using the gap statistic criterion, which is further explained in the subsequent chapter.

The vectorized 2D acoustic transmission loss data can be clustered using the k-means algorithm. Furthermore, the 3D transmission loss data matrices can be reshaped in order to employ the same cluster analysis techniques. Once the acoustic fields have been clustered appropriately the dominant effects of the ocean field uncertainties on the resulting acoustic field can be displayed effectively and utilized in enhanced probability of detection plots. Additionally, the second component of the CROM analysis is to determine the analysis of nonlinear dynamical systems through the use of modeling the system as a Markov process.

4.2 Markov Process

A stochastic process that can be classified as memoryless is referred to as a Markov process. A Markov process exhibits the Markov property, which is satisfied if each future state of the process is independent of all previous states. A discrete time Markovian process can be described mathematically in the following equation:

$$P(X_t = x_t | X_0 = x_0, X_1 = x_1, ..., X_{t-1} = x_{t-1}) = P(X_t = x_t | X_{t-1} = x_{t-1}) \tag{4.6}$$

Equation 4.6 shows that the conditional probability of a Markov process is dependent only upon the current state of the system. Therefore, knowledge of the previous states is irrelevant to the prediction of the future state of the system. The diagram in Figure 4-1 illustrates the various potential trajectories of a Markov process. The

process uses information only from time T_N and can then determine probabilistic predictions of various trajectories of the dynamical process. The predictions are based on the probability of the transitions between states C_k, C_{k+1} and C_{k+2} for each path. Using the knowledge of the state transitions and the potential temporal trajectories of the process a model can be developed that describes the dynamic evolution of an ensemble of realizations. Markov processes can be used to describe numerous physical

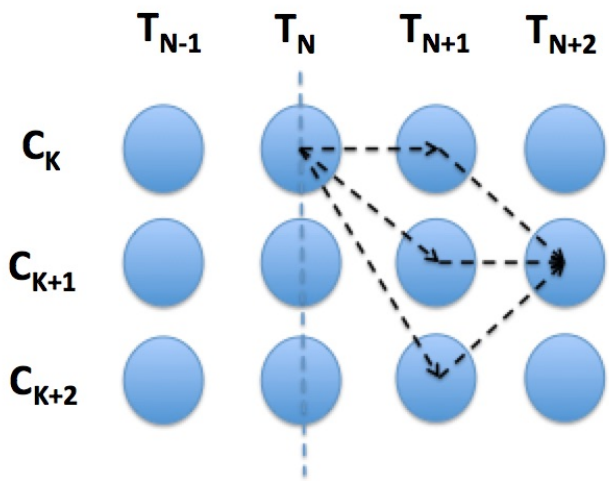

Figure 4-1: Markov Process Diagram

applications in the fields of biology, chemistry and even speech recognition.

The dynamical analysis of the cluster based reduced order modeling technique outlined by Kaiser in 2014 utilizes the statistics of the transitions between cluster states (Kaiser et al., 2014). The probability of each realization being contained within a specific cluster is determined by the weighted average of the realizations contained within the cluster, where q_k is the probability of a realization falling within a certain cluster.

$$q_k = \frac{n_k}{p} \tag{4.7}$$

The probability of transitioning between clusters or staying within the same cluster at each time step is then evaluated to determine the cluster transition matrix. The cluster transition matrix defines the single step probabilities of the transition from one cluster state to the next. The transition from one cluster to the next is tracked

with the variable n_{jk}:

$$n_{jk} = \sum_{t=1}^{T} F_k^t F_j^{t+1} \tag{4.8}$$

Where F_k^t is a function that equals 1 if the realization is contained within the cluster k at time t, otherwise the function equals 0. The matrix n_{jk} will represent the summation of the cluster transitions from c_j to c_k with relation to each time step. With the cluster transitions temporal relationship established the cluster transition matrix can be defined.

$$P_{jk} = \frac{n_{jk}}{n_k} \tag{4.9}$$

There are two properties of the cluster transition matrix. The first is that each column of the matrix sums to 1 and second property is that all the elements are non-negative. The cluster transition matrix represents the probability of each transition between or within a cluster state as represented by the arrows in Figure 4-2. The

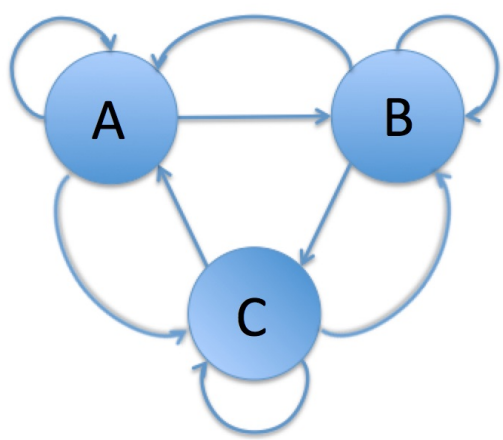

Figure 4-2: Cluster Transition Diagram

diagonal elements along the trace of the cluster transition matrix are represented by the arrows that return to the same cluster state. The cluster transition matrix provides a compact representation of the dynamics of the system. The knowledge of each cluster transition probability describes the system evolution. This methodology will be used for the analysis of the variations in the acoustic field generated from the

ensemble of ocean states.

4.3 Ocean Acoustic Cluster Based Reduced Order Modeling Methodology

For the ocean acoustic model runs an ensemble of realizations at each time step will be generated. For each time interval the generated fields will be clustered to determine a reduced state space. From this information a cluster transition matrix will be derived to describe the dynamical evolution of the system. Applying the dynamical model an enhanced probability of detection plot can be generated for the forecast ocean states and resulting acoustic fields that incorporates the uncertainties within the ocean field.

Chapter 5

2D Ocean Acoustic Uncertainty Analysis

Sound propagation in the ocean is subject to phenomena such as attenuation, absorption and scattering due to the variability of the undersea environment. The sea bed composition, surface variations, temperature and salinity are all contributing factors to the uncertainty in the acoustic field determination. Uncertainties in ocean field temperature and salinity cause variations to the speed of sound throughout the ocean field. This uncertainty in the ocean field is then transferred to the modeled acoustic field. Using ocean predictions and coupled acoustic models that factor account for uncertainty a more accurate picture of the tactical acoustic environment can be determined for operational planning.

To develop a useful counter detection decision aid that utilizes, forecast ocean states and corresponding acoustic field representations an understanding of the ocean variability and transmission of these variabilities must be understood and conveyed effectively.

The most common method of determining the uncertainty in the acoustic field has been through the use of a Monte-Carlo approach, which analyzes a large ensemble of data to complete a statistical analysis of the uncertainty. To determine the ocean variability 19 ocean state perturbations were generated from varying initial conditions and these states were dynamically evolved in time over approximately a three day

period. The data used in this study was generated for the 2008 Quantifying, Predicting and Exploiting Uncertainty experiment. For the various ocean states acoustic propagation along the shelf edge was deterministically calculated and modeled using 2D and 3D representations.

5.1 Quantifying, Predicting and Exploting Uncertainty

The data gathered during the 2008 Quantifying, Predicting and Exploiting Uncertainty (QPE 2008) experiment was used to develop the ocean models for this study. The study area for this experiment was located in the region off the North East coast of Taiwan in the East China Sea. The 2008 study focused on three areas, acoustics, ocean dynamics and bathymetric effects.

The acoustics portion of the experiment was focused on the region to the Northeast of Taiwan. This region covers the shelf break region separating the littorals from the deep water region, which is an area of high uncertainty due to variable bathymetry and uncertain ocean dynamics. The acoustic study for the QPE project utilized the SACLANTCEN normal mode propagation loss model (C-SNAP) (Ferla et al., 1993). The study evaluated several paths along and across the shelf break region to predict the propagation loss due to the cold dome effects. In the QPE study the effects due to the ocean waveguide were studied while the bathymetry and sediment properties were kept constant. Acoustic sources of 300hz, 600hz and 900hz were simulated at depths of 50m to represent upslope and downslope propagation losses.

The ocean models were generated using 4D realizations employing Error Subspace Statistical Estimation data assimilation techniques and uncertainty analysis predictions utilizing dynamically orthogonal equations with the MSEAS ocean model (Lermusiaux et al., 2010). As described earlier the MSEAS ocean model utilizes the primitive equations with hydrostatic and Boussinesq approximations while also accounting for free surface effects. The data inputs to the MSEAS ocean model included

atmospheric forcing effects, atmospheric heat flux and high resolution bathymetry models. During the exercise the ocean realizations were supplied as inputs to acoustic models. Additionally, the ocean dynamics portion of the QPE 2008 pilot study evaluated the advection of tracers in the East China Sea surrounding Taiwan. The bathymetry of this region is depicted in Figure 5-1. The ocean models evaluated the effect of advection and diffusion on the location of tracer mooring sites. These results were used to determine adequate sites for testing where currents and shelf dynamics would exhibit strong characteristics.

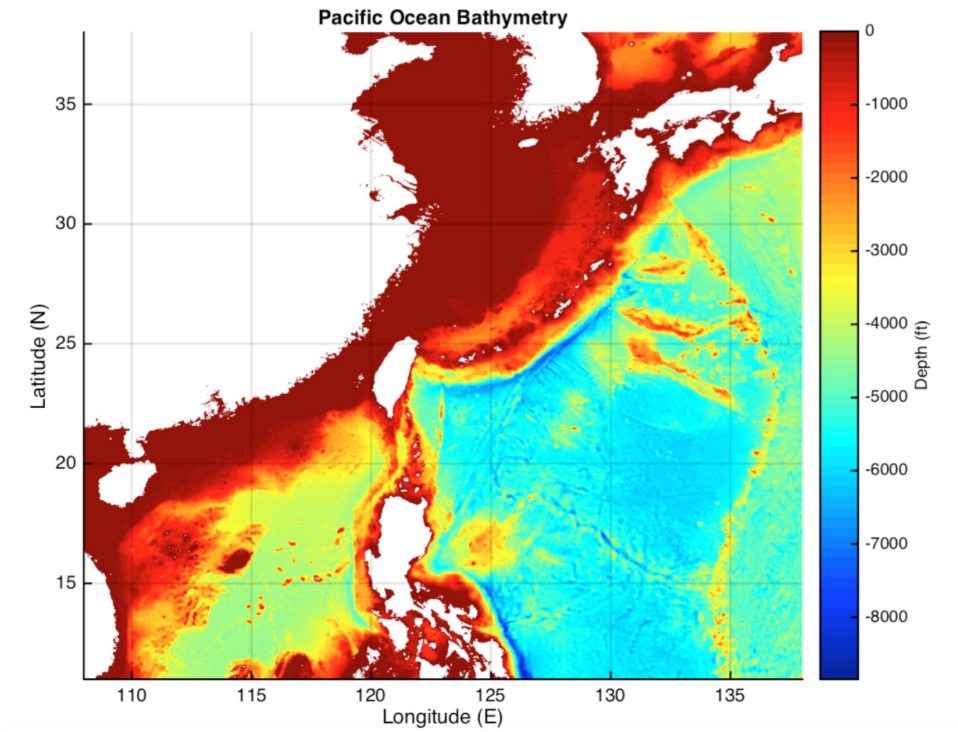

Figure 5-1: Bathymetry Plot of Western Pacific

The region of this focused ocean dynamics study can be seen in Figure 5-2, which depicts the surface velocity field in the region at 00:00Z on 06 September 2009. In this figure the Kuroshio Current can be seen heading to the North East of the island of Taiwan. This large scale ocean realization was used to model the ocean characteristics in the region and the acoustic study was conducted on a nested and reduced grid scale to the North East of Taiwan.

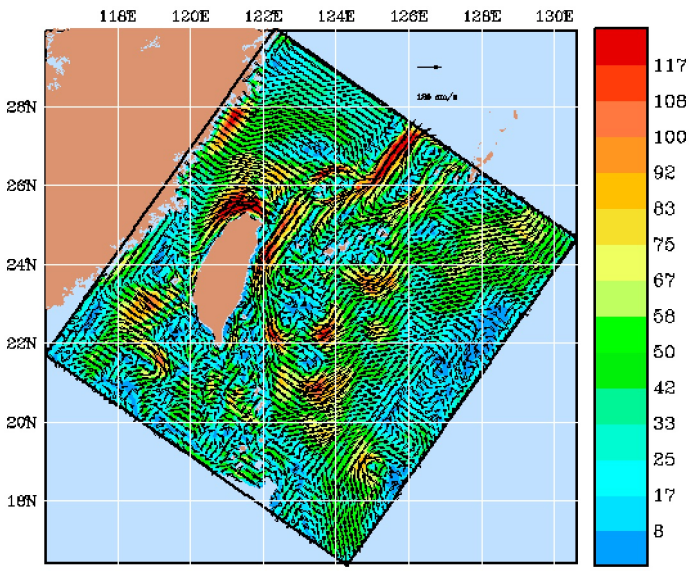

Figure 5-2: Kuroshio Current: Surface Velocity

5.2 2D Ocean Acoustic Uncertainty Evaluation

In order to gain a more thorough understanding of the acoustical effects due to ocean field uncertainty each ocean field initial condition was slightly perturbed to generate an ensemble of ocean predictions. These ocean field realizations were generated over the course of a three and a half day period from 21:00Z on 04 September 2009 to 12:00Z on 07 September 2009 at three hour increments. With 19 realizations for each of the 21 time intervals over the course of several days the effects of cyclical ocean tides, internal waves effects and daily changes in ocean state can be identified and evaluated to determine the effect that this will have on the acoustic propagation of sound. The statistical evaluation of the varying acoustic fields generated can be used to better understand the sonar performance predictions along the dynamic shelf break region.

5.2.1 Acoustic Model Inputs

Bathymetry

The topography in the waters surrounding Taiwan is complex and varying. To the north and west of Taiwan the East China Sea continental shelf is a shallow littoral

region that extends along the coast of China. The shelf break region extends to the Northeast of Taiwan, which descends into the Okinawa trough. The shelf ridge continues to drop off further to the Southeast reaching its deepest depths in the Huatung Basin and Ryukyu Trench as seen in Figure 5-4 (Rudnick et al., 2011). The primary region of the acoustic model runs for the N-2D slice study and the

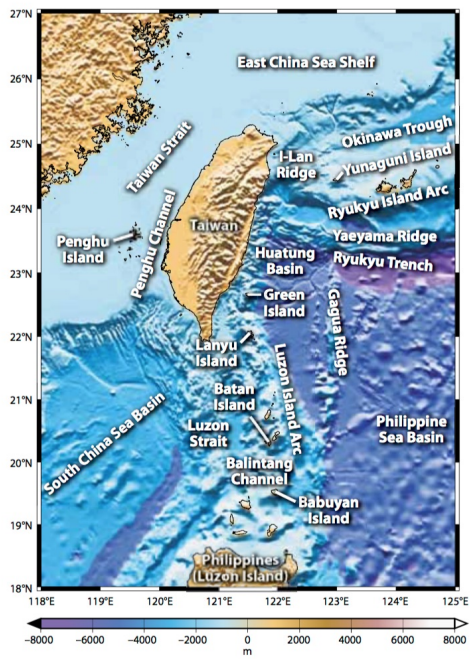

Figure 5-3: Topographical Features Surrounding Taiwan (Rudnick et al., 2011)

3D acoustic model were centered at a longitude of 122°33'00" E and a latitude of 25°43'00" N. The acoustic propagation was analyzed for a 2D slice and a 3D region. The 2D slice is represented by the white line at a bearing of 164° from the acoustic source as seen in Figure 5-4. The 3D acoustic area for this study region is highlighted by the white circle in Figure 5-4. The bathymetric data input to the acoustic model was obtained from the National Ocean and Atmospheric Administration center for environmental information. The data obtained for the region of acoustic study had a resolution of 1 arc-second. The acoustic grid data was extracted and imported into the acoustic model (Amante and Eakins, 2009). In order to assess the bathymetric features and determine a suitable area with complex features along the shelf break region the topographic data was plotted using MATLAB codes derived from the

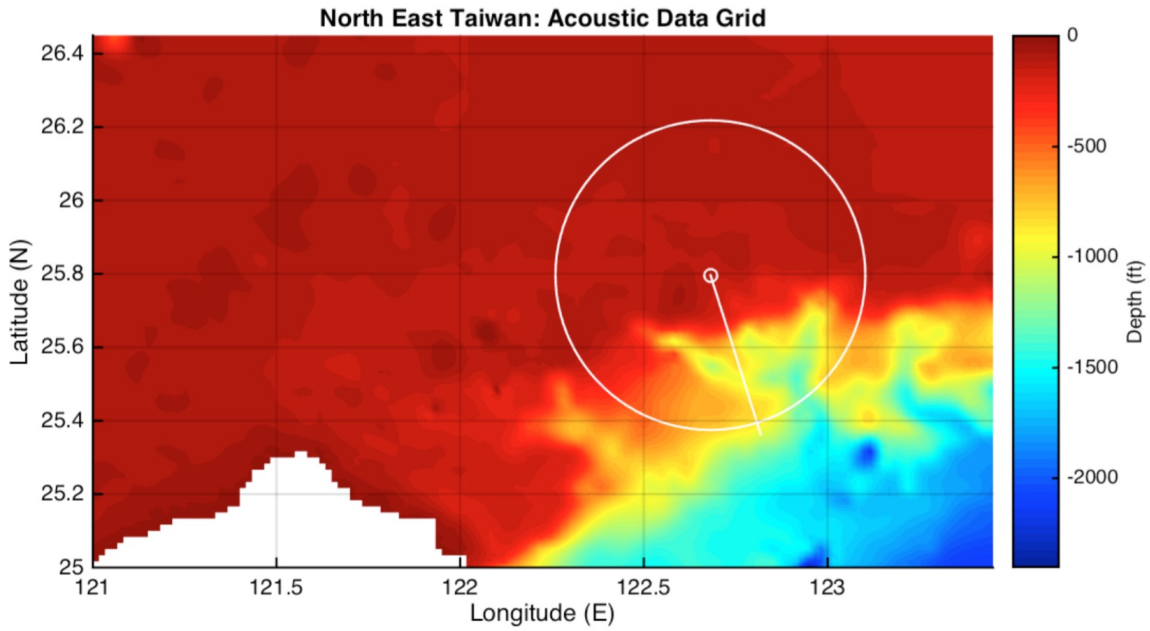

Figure 5-4: Focused Acoustic Study Region

techniques described in the text *MATLAB Recipes for Earth Sciences* (Trauth et al., 2007). Additionally, a profile of the region where the 2D slice data was analyzed can be seen in Figure 5-5

Figure 5-5: 2D Slice Bathymetric Profile

The plots of the bathymetric features of the region clearly identify the critical shelf break. Specifically, the area that was selected for the acoustic study was centered on the North Mien-Hua Canyon. This canyon along the shelf region Northwest of the island of Taiwan is located in an area of dynamic ocean and atmospheric conditions, which make it a unique region to analyze these complex effects on acoustic performance.

Sediment

The acoustic properties of the ocean seabed can have a significant effect on the propagation of sound through the ocean. The sediment layer can exhibit variations and uncertainties that would complicate the study of ocean properties effect on the acoustic field. Therefore, for this study in order to isolate the effects of uncertain ocean states on the resulting acoustic field the sediment was modeled as range independent. To model the acoustic propagation in the region of study accurately while using a range independent sediment a representative value must be used describing the sediment properties in the region. The sediment properties in the North Mien-Hua region had previously been studied during the QPE exercise to better understand and validate sound speed attenuation models of sediment. Chirp sonar responses were used to validate the Biot model with a fluid approximation. The model in the QPE experiment was able to estimate the sediment properties to include the sound speed, density and attenuation. In order to validate the results of this experiment the calculated properties were compared to core samples that were taken from the North Mien-Hua canyon region (Chiu et al., 2015). The sediment grain size obtained from the core samples can be used to determine the mean grain diameter using Equation 5.1.

$$\phi = -\log_2(d/d_o) \tag{5.1}$$

In this equation d represents the grain diameter and ϕ represents the mean grain size. The grain size, porosity and permeability are used to determine the attenuation characteristics of the sound in the sediment. The values of porosity, β and permeability, κ can be calculated using the following formulas. The first was determined through experimentation to determine a relationship between the mean grain size and the porosity (Bachman, 1985).

$$\phi = \frac{0.0943 - \sqrt{0.0943^2 - 4(0.034)(\beta - 0.208)}}{2(0.00334)} \tag{5.2}$$

The second is a modified Kozeny-Carman equation used to determine the permeability (Hovem and Ingram, 1979).

$$\kappa = \frac{d^2\beta^2}{180(1-\beta)^2} \tag{5.3}$$

For the purpose of this study the data obtained from the core samples is used as a representative sample of the region. The core samples indicated that the sediment type varied from coarse sand in the north to fine silt in the south. The compressional wave speed in the sediments varied from 1529 m/s to 1747 m/s (Chiu et al., 2015). The region of acoustic study for this paper is located primarily in the southern end of the region corresponding to the silty region that was studied and a ϕ value of 5 was used. Table 5.1 provides examples of various sediment types and grain sizes (Krumbein and Sloss, 1951).

Table 5.1: Sediment Mean Grain Size Table

ϕ	Size (metric)	Wentworth Class
-8	>256 mm	Boulder
-5	32 mm	Coarse Gravel
-1	2 mm	Fine Gravel
1	0.5 mm	Coarse Sand
5	62 μm	Silt
8	<3.9 μm	Clay

Temperature and Salinity

The acoustic model employed is a range dependent parabolic equation model that utilizes 4D temperature and salinity fields to accurately represent the ocean state. The ocean states are generated using the MSEAS high-fidelity multi-resolution simulations. The temperature and salinity fields are predicted from an ensemble of ocean states and each ocean state will generate a unique acoustic field.

The temperature and salinity field forecasts were generated with the ocean model and assimilated with the ocean data from the QPE experiment. The Error Subspace Statistical Estimation (Lermusiaux, 2006), was employed for data assimilation and

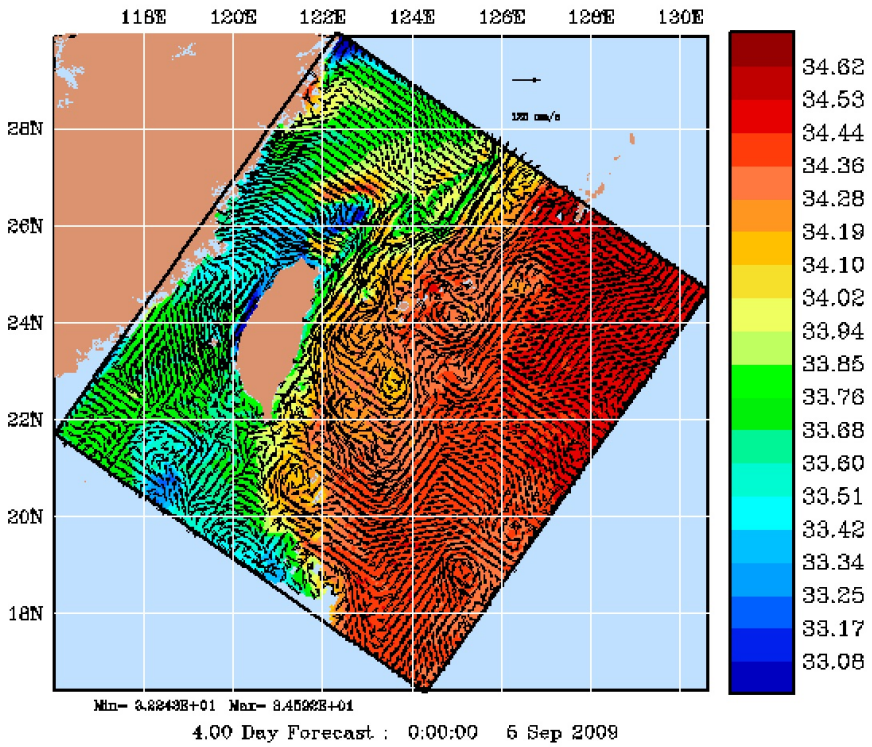

Figure 5-6: Surface Salinity

uncertainty analysis. Additionally, sub-grid scale ocean processes are represented through the use of dynamically orthogonal stochastic partial differential equations. The stochastic partial differential equations represent the deterministic ocean equations as well as the additional stochastic effects. Deterministic effects include those incorporated into the ocean model equations described in Chapter 2.

The stochastic effects include the sub grid scale processes such as internal waves and turbulence that are not described by the deterministic equations. Additionally, river discharge from Taiwan can affect the salinity concentrations, which generates additional uncertainties (Landry, 2014, Mirabito et al., 2012). The temperature and salinity fields are perturbed several times and each perturbation is then dynamically evolved in time to generate the time series ensemble forecast ocean states. The fields are then reduced to the region along the north coast of Taiwan to serve as an input to the Peregrine program. An example of the surface salinity field is displayed in Figure 5-6. Additionally a representative surface temperature field is displayed in Figure 5-7.

The 4D ocean realizations are used for the acoustic code to capture range and

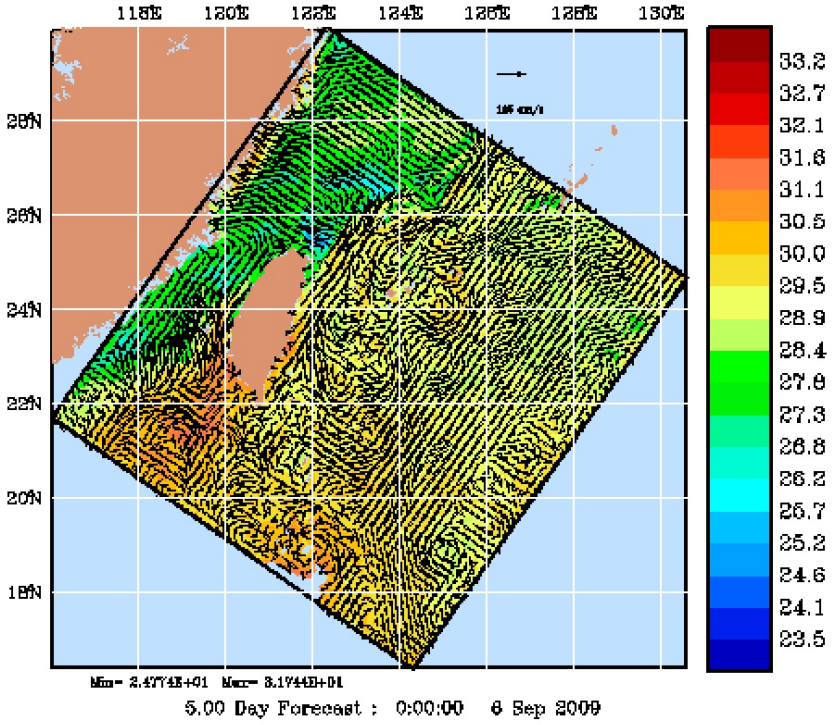

Figure 5-7: Surface Temperature

depth effects of the ocean field on the propagation. For this study the primary focus is to isolate the acoustic effects due to the variations and uncertainty contained within the ocean field and quantitatively represent these variations. The focused region of the acoustic study was can be seen in the two initial ocean temperature perturbations displayed in Figure 5-8 and the initial salinity perturbation are displayed in Figure 5-9. The perturbations shown in these figure demonstrate the extent of the variations in the temperature and salinity fields for the focused region of the acoustic study at the starting time.

The each perturbation of the model is dynamically evolved in time to generate the ensembles. There are a total of 19 realizations at each time interval of the entire temperature and salinity field. For reference the final time interval perturbations for temperature and salinity are displayed in Figure 5-10 and Figure 5-11 respectively. These ocean field realizations were used for the 2D and 3D acoustic field models in order to perform uncertainty analysis.

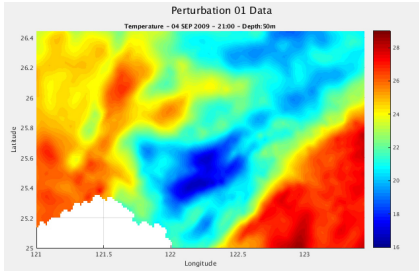

(a) Temperature Perturbation 01

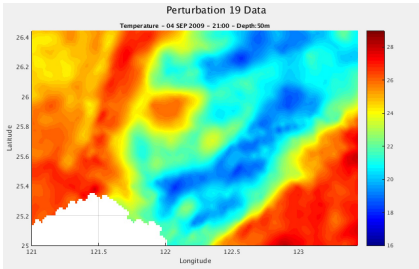

(b) Temperature Perturbation 19

Figure 5-8: Initial Ocean Field Temperature Pertubations

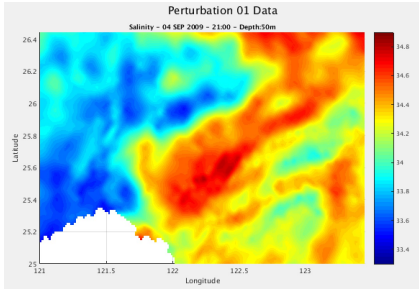

(a) Salinity Perturbation 01

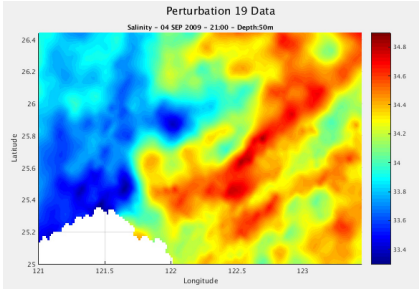

(b) Salinity Perturbation 19

Figure 5-9: Initial Ocean Field Salinity Pertubations

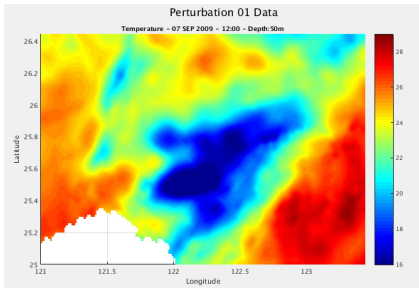

(a) Final Temperature Perturbation 01

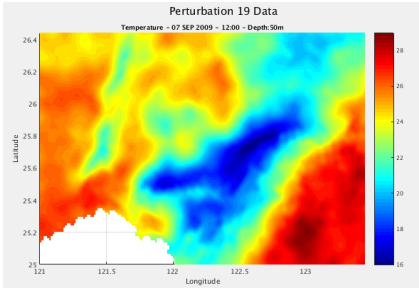

(b) Final Temperature Perturbation 19

Figure 5-10: Final Ocean Field Temperature Perturbations

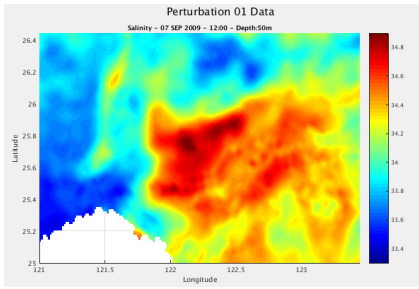

(a) Final Salinity Perturbation 01

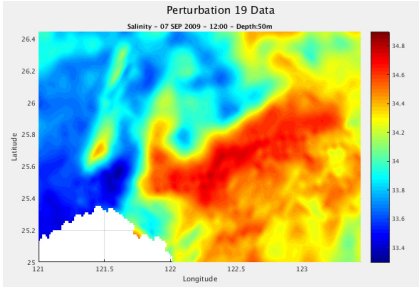

(b) Final Salinity Perturbation 19

Figure 5-11: Final Ocean Field Salinity Pertubations

Speed of Sound

The speed of sound in the ocean has been determined though laboratory measurements to be a function of the temperature, salinity and depth fields. The speed of sound in ocean has been empirically determined and represented by Mackenzie's nine term equation (Mackenzie, 1981).

$$\begin{aligned} c =& 1448.96 + 4.591T - 5.304 \times 10^{-2}T^2 + 2.374 \times 10^{-4}T^3 \\ &+ 1.340(S - 35) + 1.630 \times 10^{-2}D + 1.675 \times 10^{-7}D^2 \\ &- 1.025 \times 10^{-2}T(S - 35) - 7.139 \times 10^{-13}TD^3 \end{aligned} \tag{5.4}$$

Several empirical sound speed determinations have been made in addition to Mackenzie's equation, two examples include the equations by (Coppens, 1981), or (Lovett, 1978). However, each equation has its limits for temperature, salinity and depth. The Mackenzie formula is valid over the region that is used for this study. The temperature limits for the Mackenzie formula are 0^oC $\leq$ T $\leq$ 30^oC. The salinity limits are 30 ppt $\leq$ S $\leq$ 40 ppt and the depth limits are 0 m $\leq$ D $\leq$ 8000 m (Etter, 2013). The sound speed is generally measured experimentally with expendable bathythermographs that measure temperature and salinity directly. A second method uses a velocimeter that determines the sound speed directly by calculating the travel time of a pulse. For the acoustic model used in this study the speed of sound is determined at each grid point utilizing the temperature and salinity field from the MSEAS model. Subsequent ocean sound speed plots are generated using the Mackenzie formula. These plots are used to display the cumulative effect of the variations within both temperature and salinity fields.

Time

The time of the data collection for this experiment was during the fall of 2009. During the fall in the East China sea near the region of study north of Taiwan there are several factors that effect the ocean states. During the summer months the region typically experiences a high number of tropical storms. Typically, there are 3-5 storm systems

with possibly one per month developing into a typhoon during this period. The storm systems develop in the southern regions surrounding the eastern Philippines and track to the Northeast. These systems also strengthen around the region of Taiwan due to the elevated temperature of the ocean currents that flow into the region. During strong storms wind speeds can range from 20-40 mph. During the time interval of this study there was no severe weather taking place (Davis, 2016). Typhoon Morakot had passed through the region of study on 11 August 2009 approximately 1 month before the data collection period used in this study. During the time frame of this study the region experienced seasonable temperatures and calm weather with no precipitation. The exact times for each interval of the ocean model runs are listed in the subsequent table.

Date Time Group of Ocean Data Runs			
1	Fri, 04 Sep 2009 21:00:00 GMT	12	Sun, 06 Sep 2009 06:00:00 GMT
2	Sat, 05 Sep 2009 00:00:00 GMT	13	Sun, 06 Sep 2009 09:00:00 GMT
3	Sat, 05 Sep 2009 03:00:00 GMT	14	Sun, 06 Sep 2009 12:00:00 GMT
4	Sat, 05 Sep 2009 06:00:00 GMT	15	Sun, 06 Sep 2009 15:00:00 GMT
5	Sat, 05 Sep 2009 09:00:00 GMT	16	Sun, 06 Sep 2009 18:00:00 GMT
6	Sat, 05 Sep 2009 12:00:00 GMT	17	Sun, 06 Sep 2009 21:00:00 GMT
7	Sat, 05 Sep 2009 15:00:00 GMT	18	Mon, 07 Sep 2009 00:00:00 GMT
8	Sat, 05 Sep 2009 18:00:00 GMT	19	Mon, 07 Sep 2009 03:00:00 GMT
9	Sat, 05 Sep 2009 21:00:00 GMT	20	Mon, 07 Sep 2009 06:00:00 GMT
10	Sun, 06 Sep 2009 00:00:00 GMT	21	Mon, 07 Sep 2009 09:00:00 GMT
11	Sun, 06 Sep 2009 03:00:00 GMT	22	Mon, 07 Sep 2009 12:00:00 GMT

5.3 2D Ocean Slice States

The following section will display the mean and standard deviation for the 2D ocean states, for salinity, temperature and sound speed for all 22 time intervals along the slice shown in Figure 5-4.

5.3.1 2D Ocean Slice: Mean Salinity

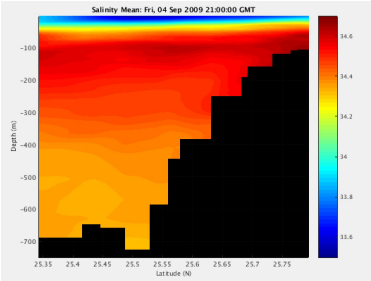

(a) Time 1

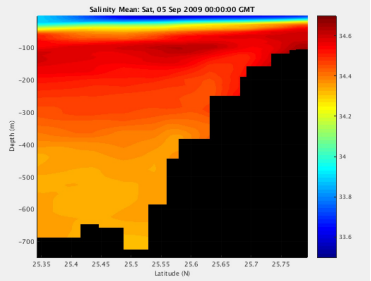

(b) Time 2

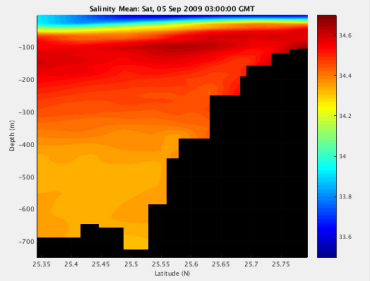

(c) Time 3

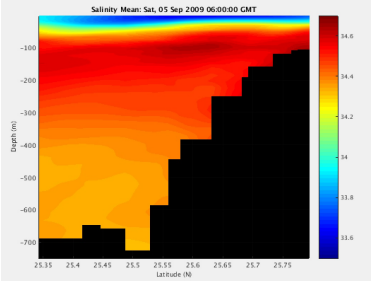

(d) Time 4

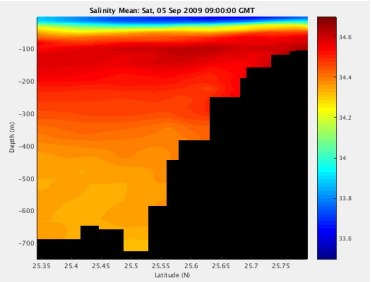

(e) Time 5

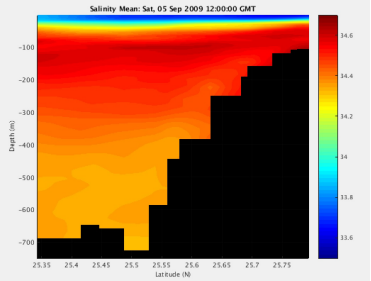

(f) Time 6

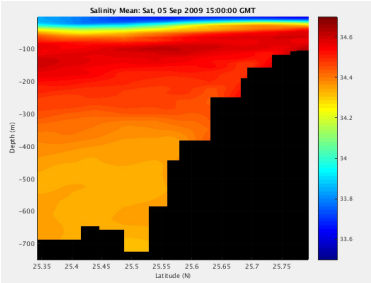

(g) Time 7

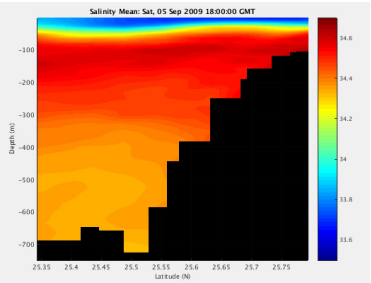

(h) Time 8

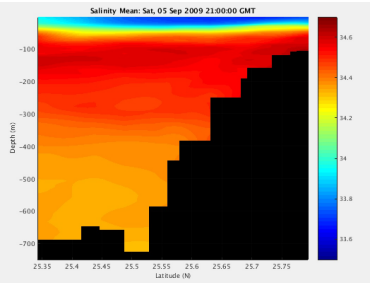

(i) Time 9

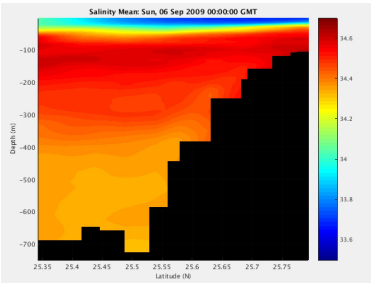

(j) Time 10

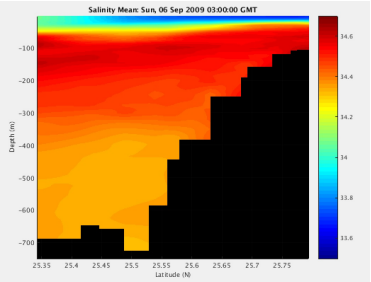

(k) Time 11

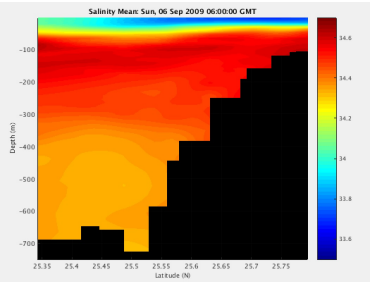

(l) Time 12

Figure 5-12: 2D Slice Salinity Mean

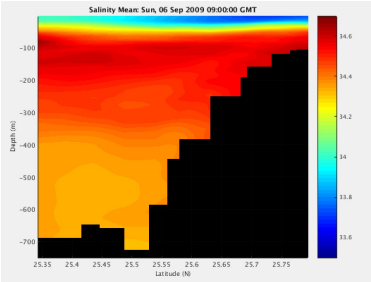

(m) Time 13

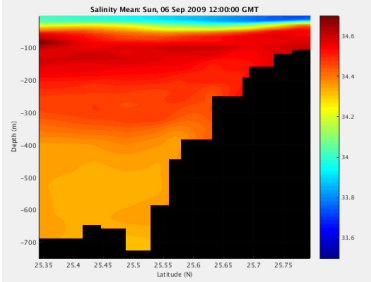

(n) Time 14

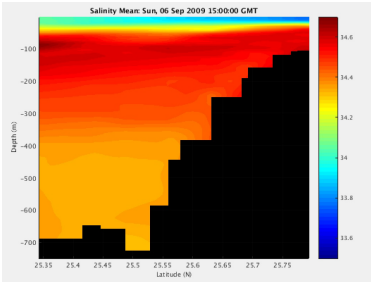

(o) Time 15

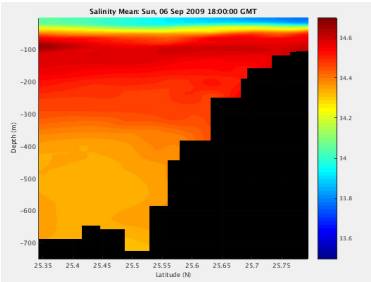

(p) Time 16

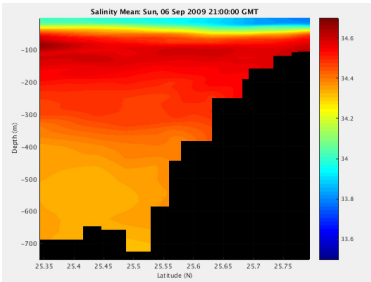

(q) Time 17

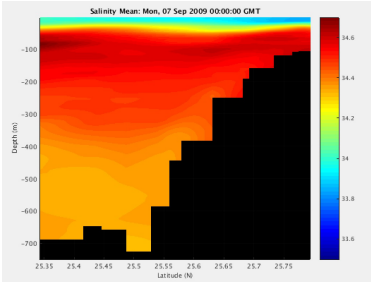

(r) Time 18

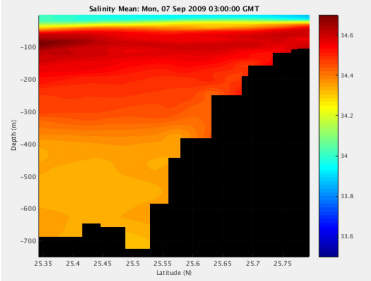

(s) Time 19

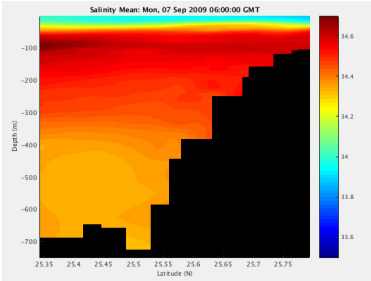

(t) Time 20

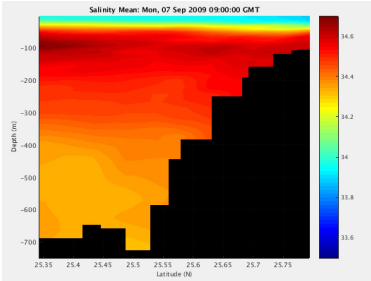

(u) Time 21

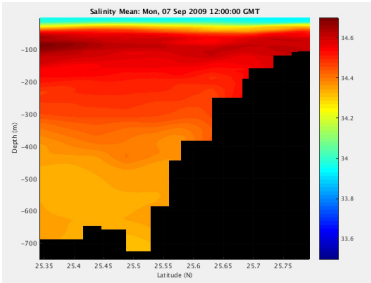

(v) Time 22

Figure 5-12: 2D Slice Salinity Mean

5.3.2 2D Ocean Slice: Salinity Standard Deviation

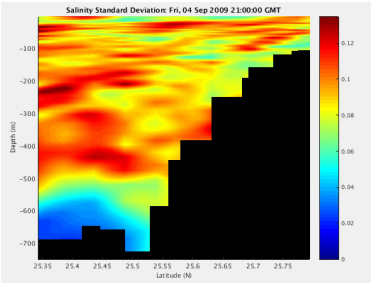

(a) Time 1

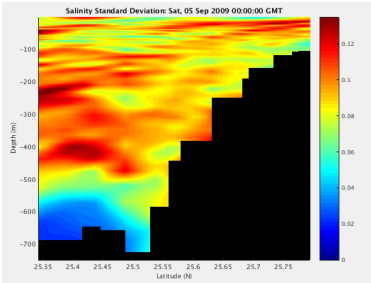

(b) Time 2

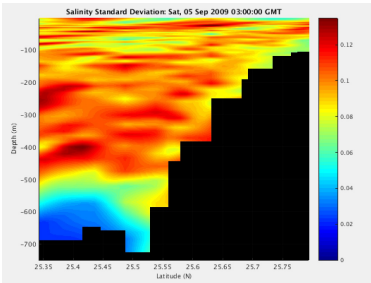

(c) Time 3

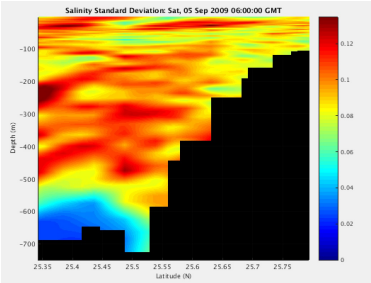

(d) Time 4

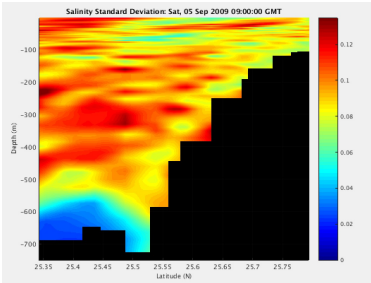

(e) Time 5

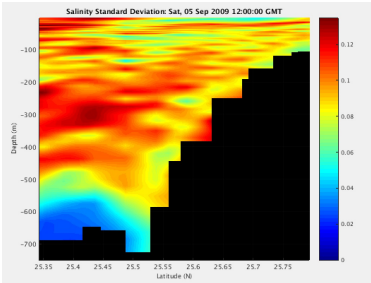

(f) Time 6

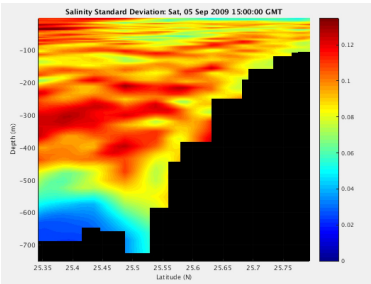

(g) Time 7

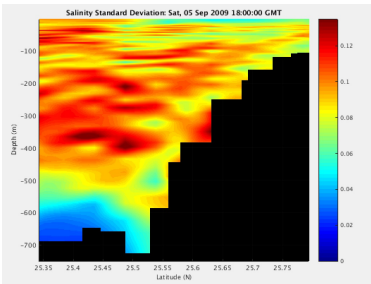

(h) Time 8

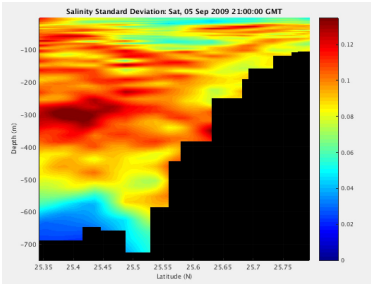

(i) Time 9

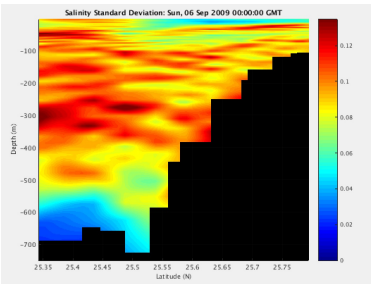

(j) Time 10

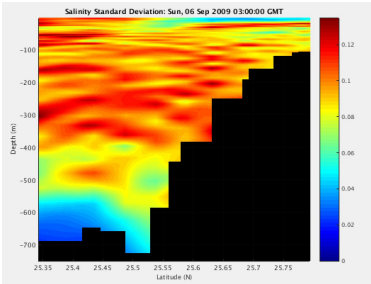

(k) Time 11

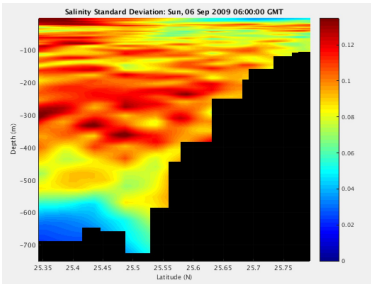

(l) Time 12

Figure 5-13: 2D Slice Salinity Standard Deviation

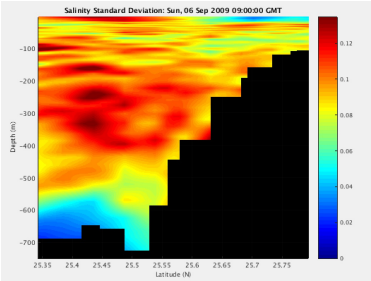

(m) Time 13

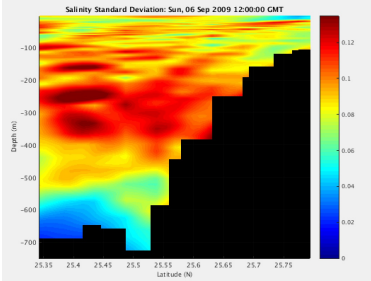

(n) Time 14

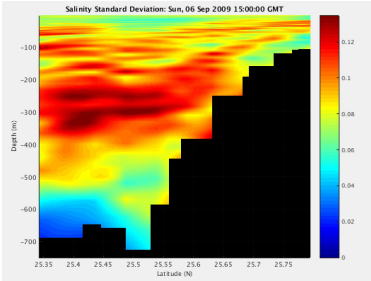

(o) Time 15

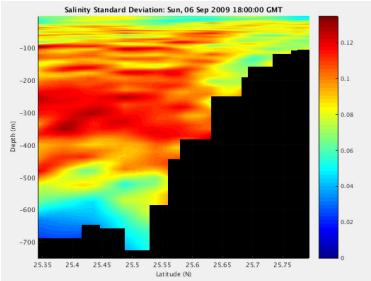

(p) Time 16

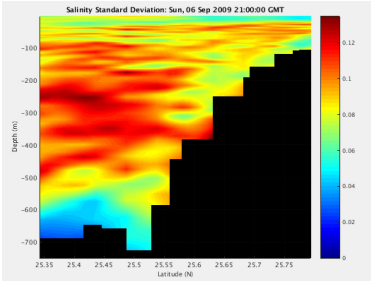

(q) Time 17

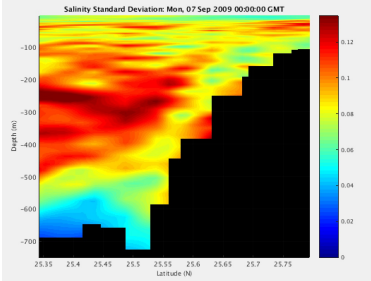

(r) Time 18

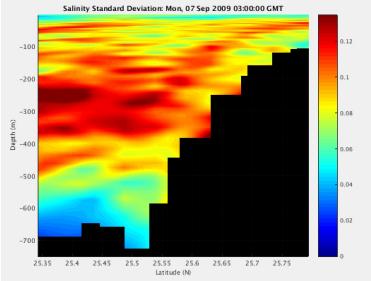

(s) Time 19

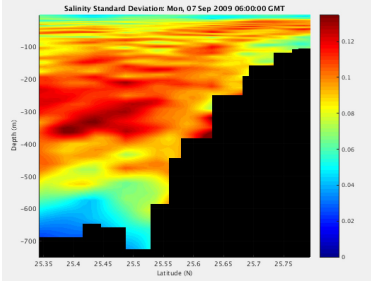

(t) Time 20

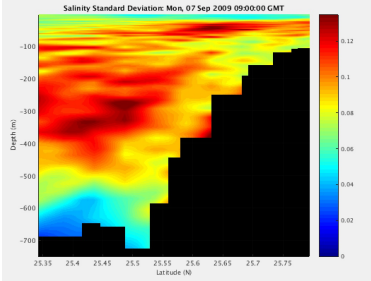

(u) Time 21

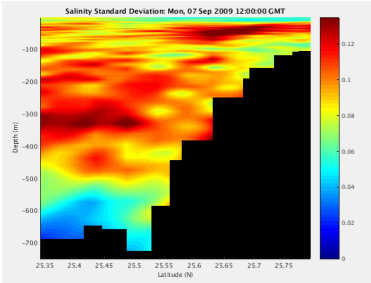

(v) Time 22

Figure 5-13: 2D Slice Salinity Standard Deviation

5.3.3 2D Ocean Slice: Mean Temperature

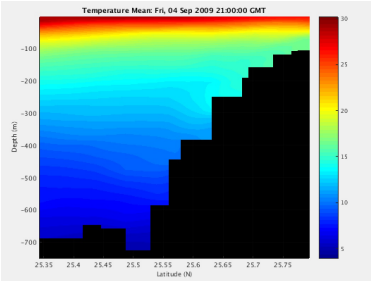

(a) Time 1

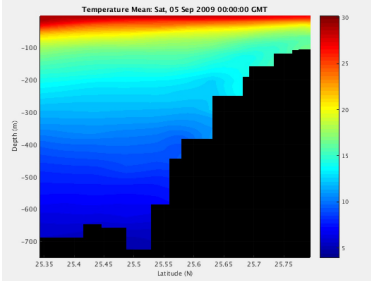

(b) Time 2

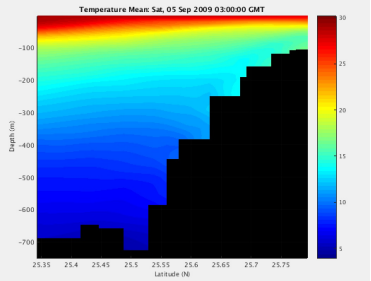

(c) Time 3

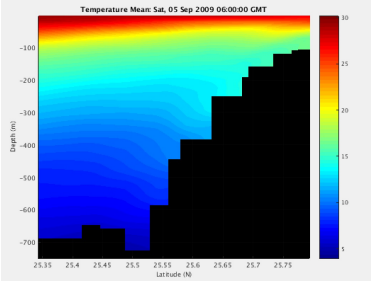

(d) Time 4

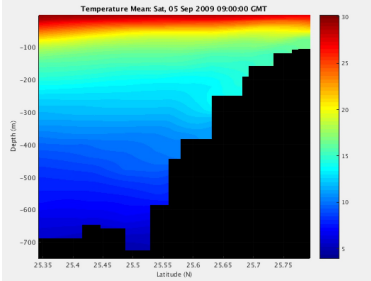

(e) Time 5

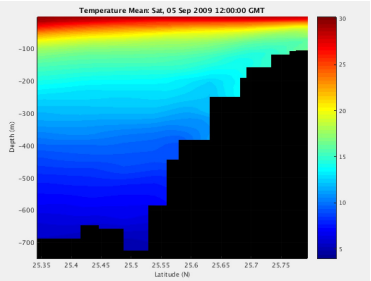

(f) Time 6

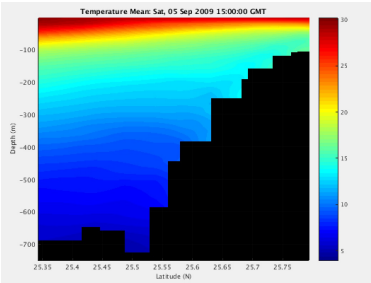

(g) Time 7

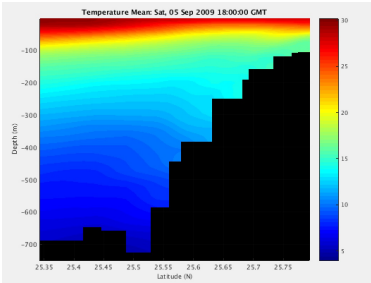

(h) Time 8

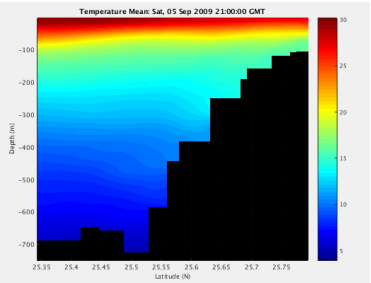

(i) Time 9

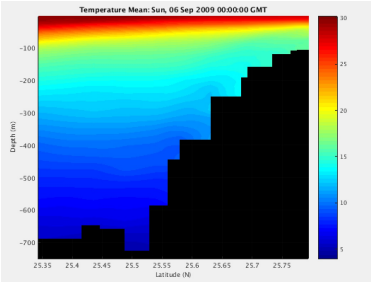

(j) Time 10

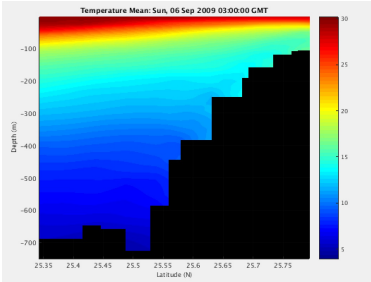

(k) Time 11

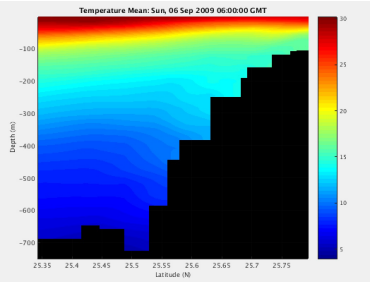

(l) Time 12

Figure 5-14: 2D Slice Temperature Mean

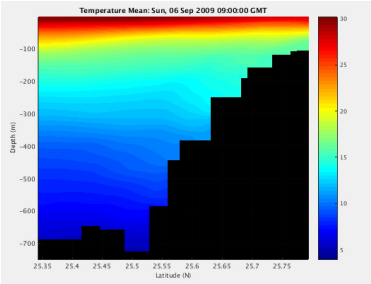

(m) Time 13

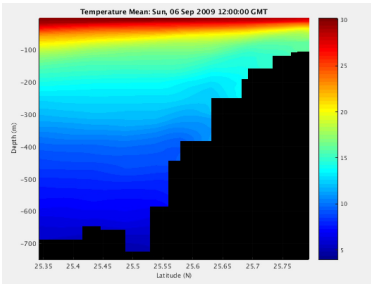

(n) Time 14

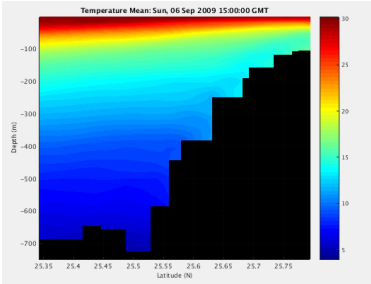

(o) Time 15

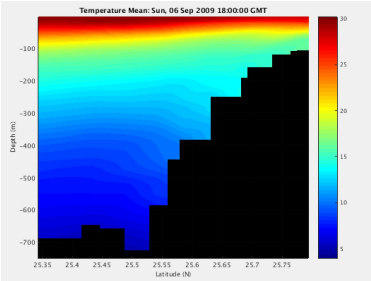

(p) Time 16

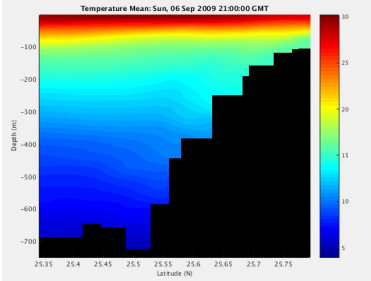

(q) Time 17

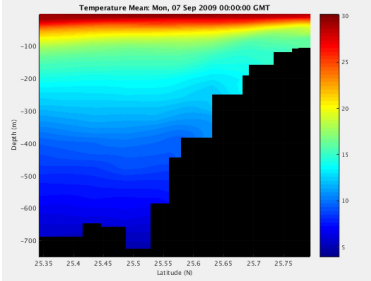

(r) Time 18

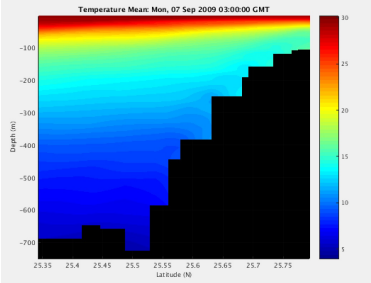

(s) Time 19

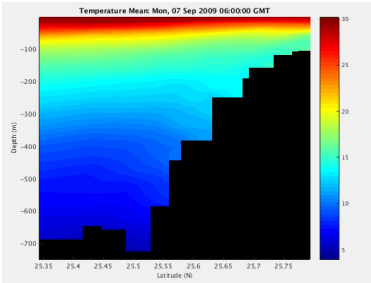

(t) Time 20

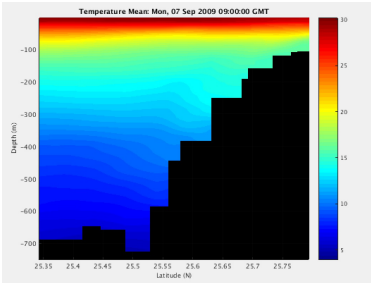

(u) Time 21

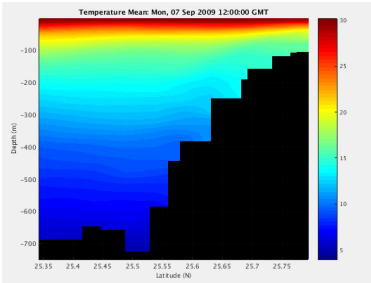

(v) Time 22

Figure 5-14: 2D Slice Temperature Mean

5.3.4 2D Ocean Slice: Temperature Standard Deviation

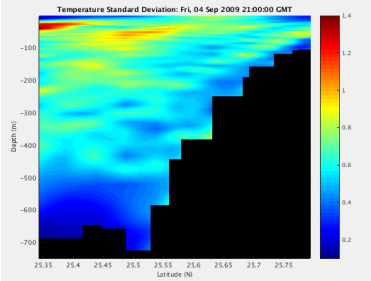

(a) Time 1

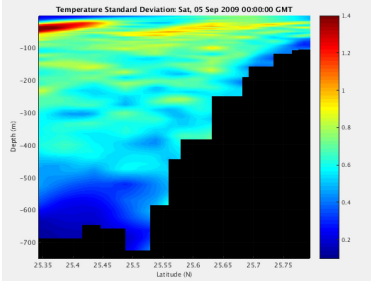

(b) Time 2

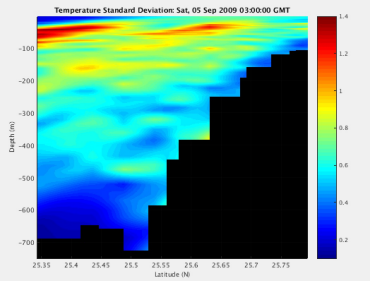

(c) Time 3

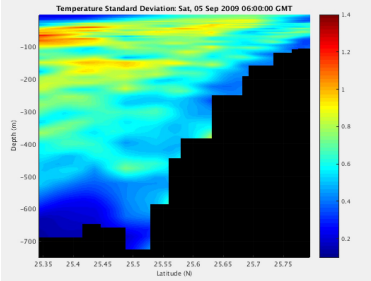

(d) Time 4

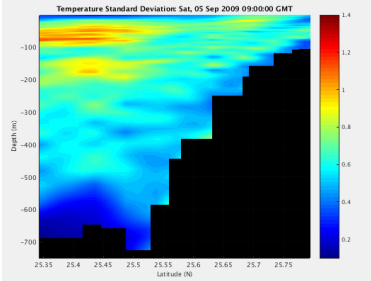

(e) Time 5

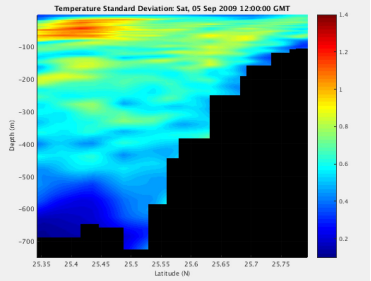

(f) Time 6

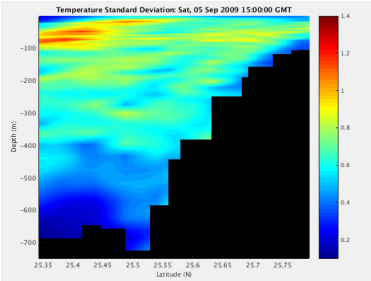

(g) Time 7

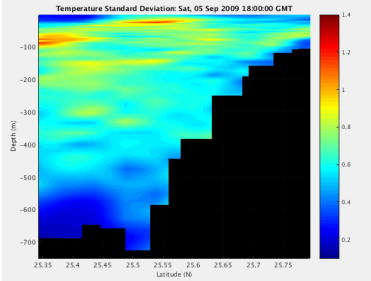

(h) Time 8

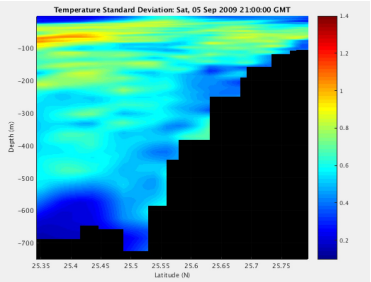

(i) Time 9

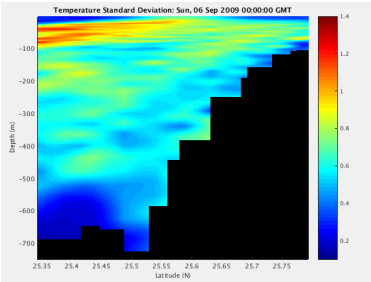

(j) Time 10

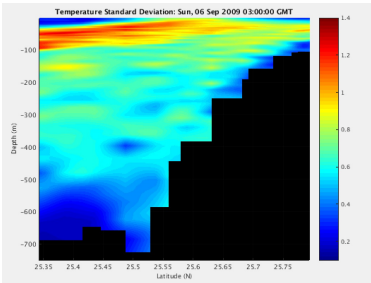

(k) Time 11

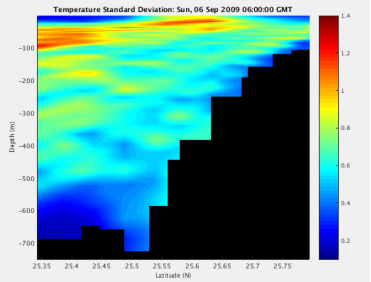

(l) Time 12

Figure 5-15: 2D Slice Temperature Standard Deviation

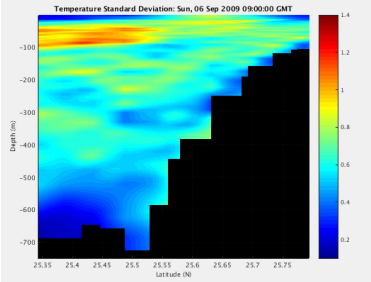

(m) Time 13

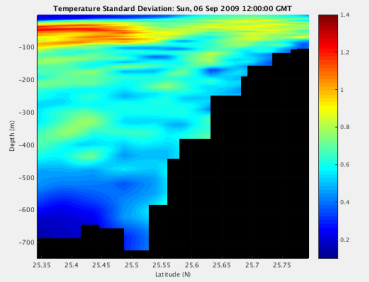

(n) Time 14

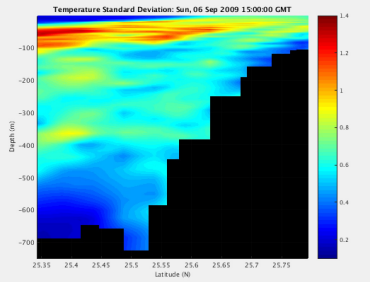

(o) Time 15

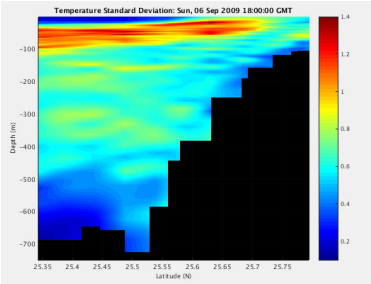

(p) Time 16

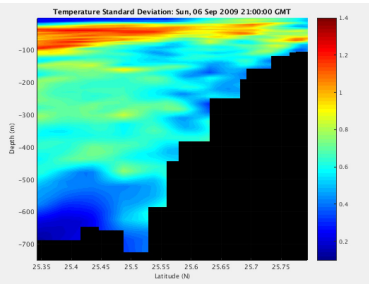

(q) Time 17

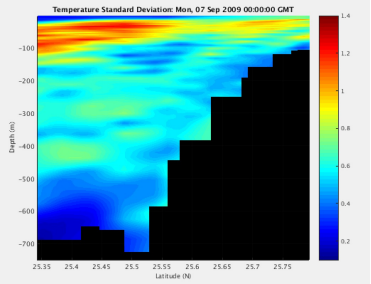

(r) Time 18

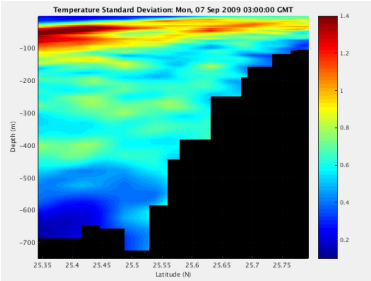

(s) Time 19

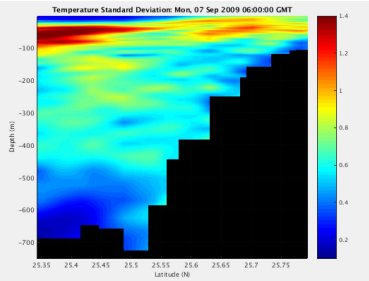

(t) Time 20

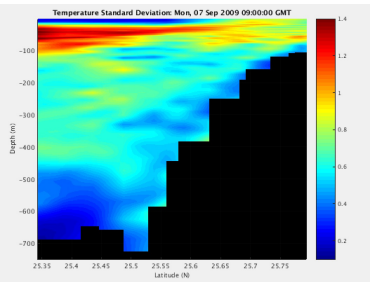

(u) Time 21

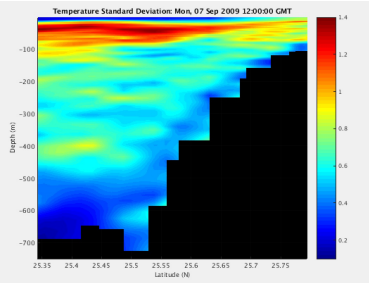

(v) Time 22

Figure 5-15: 2D Slice Temperature Standard Deviation

5.3.5 2D Ocean Slice: Mean Sound Speed

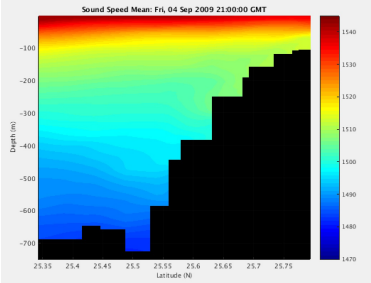

(a) Time 1

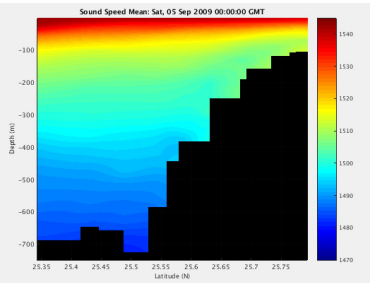

(b) Time 2

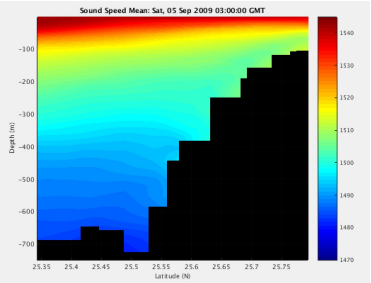

(c) Time 3

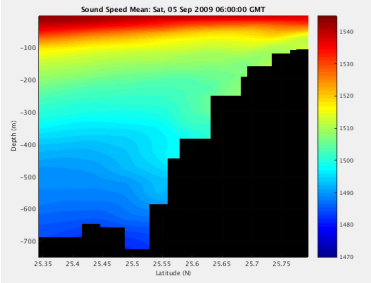

(d) Time 4

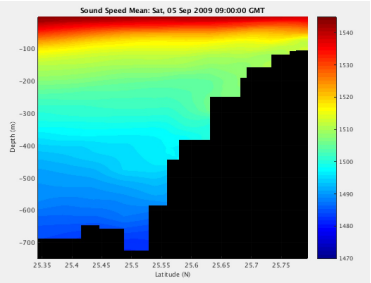

(e) Time 5

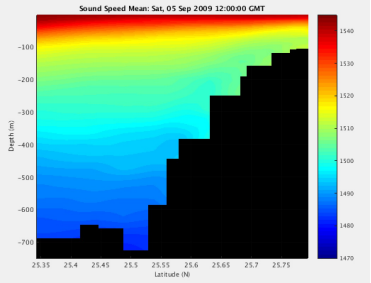

(f) Time 6

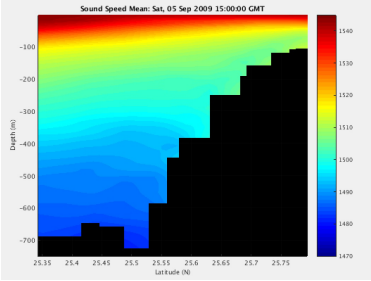

(g) Time 7

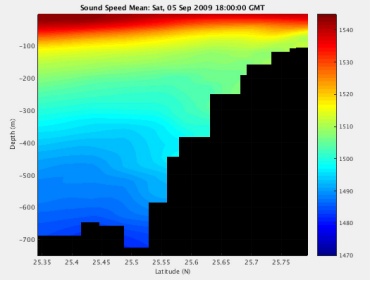

(h) Time 8

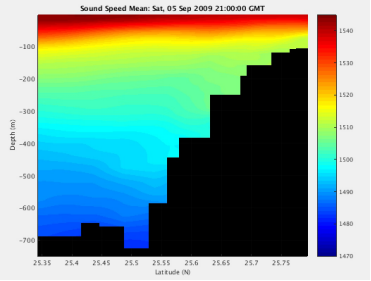

(i) Time 9

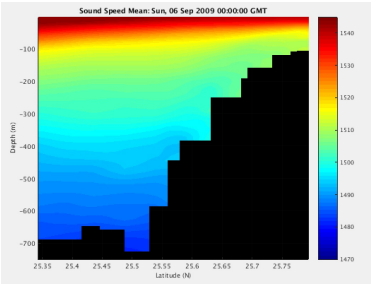

(j) Time 10

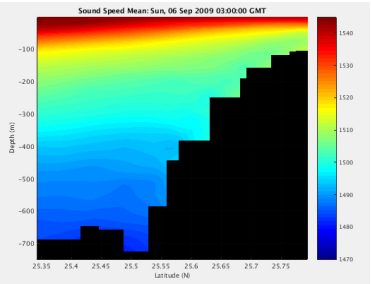

(k) Time 11

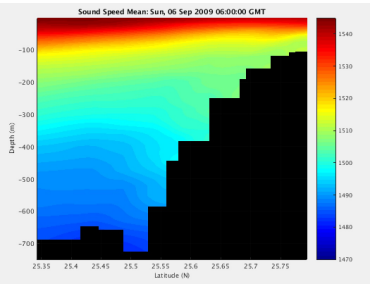

(l) Time 12

Figure 5-16: 2D Slice Sound Speed Mean

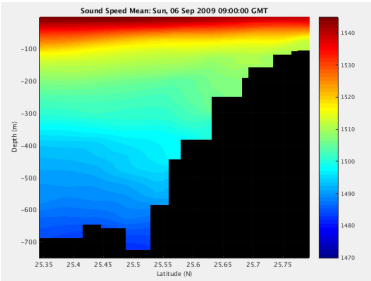

(m) Time 13

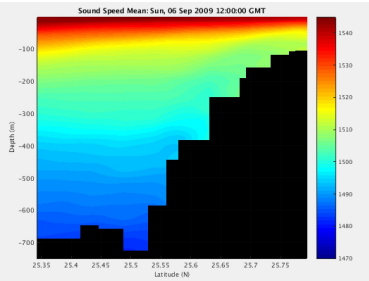

(n) Time 14

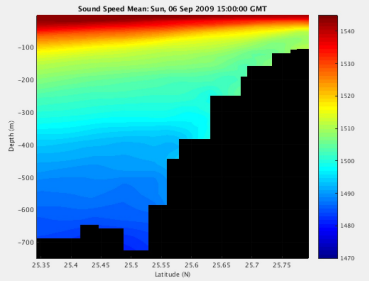

(o) Time 15

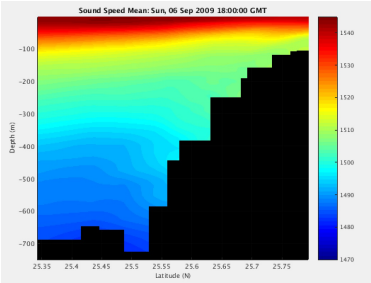

(p) Time 16

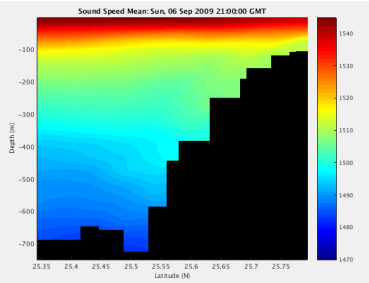

(q) Time 17

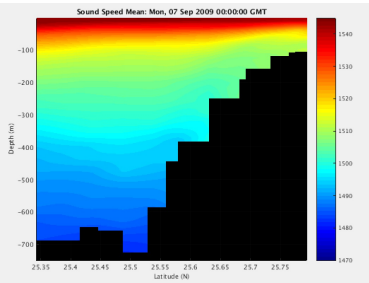

(r) Time 18

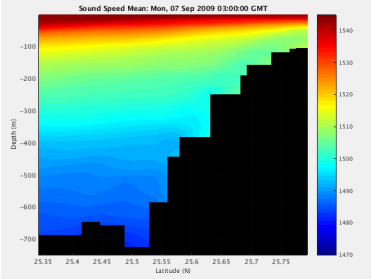

(s) Time 19

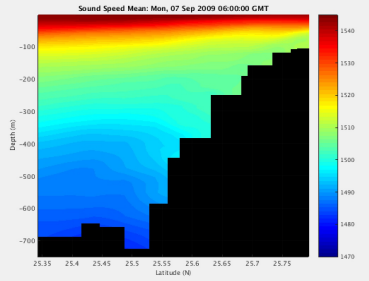

(t) Time 20

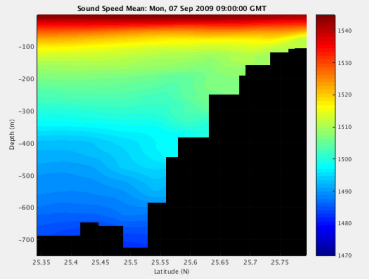

(u) Time 21

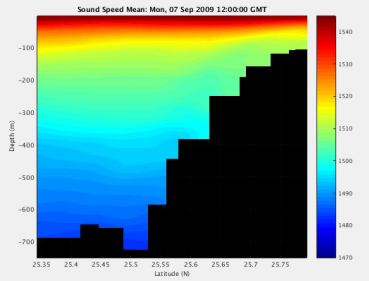

(v) Time 22

Figure 5-16: 2D Slice Sound Speed Mean

5.3.6 2D Ocean Slice: Sound Speed Standard Deviation

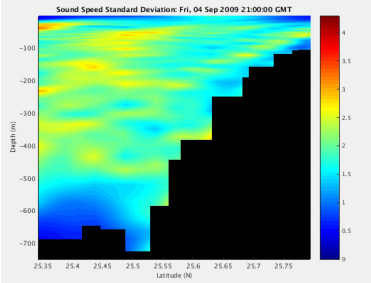

(a) Time 1

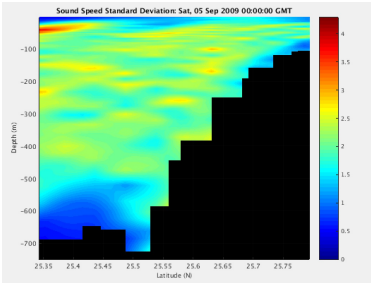

(b) Time 2

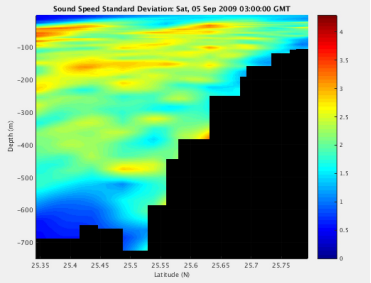

(c) Time 3

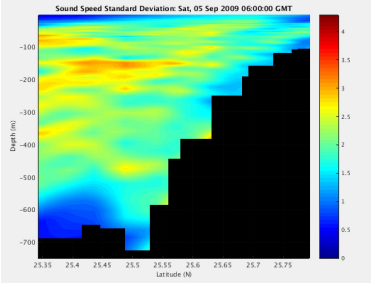

(d) Time 4

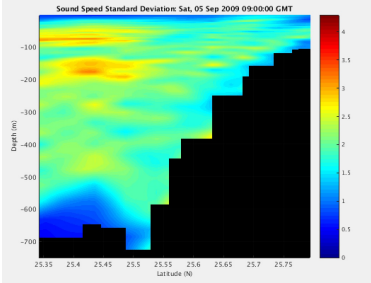

(e) Time 5

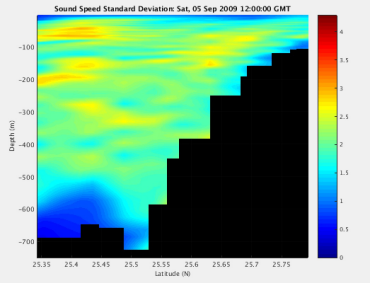

(f) Time 6

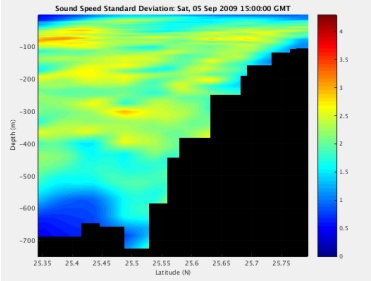

(g) Time 7

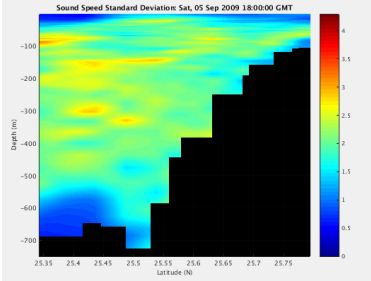

(h) Time 8

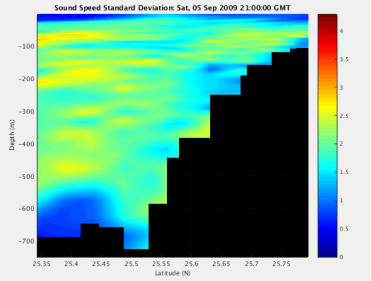

(i) Time 9

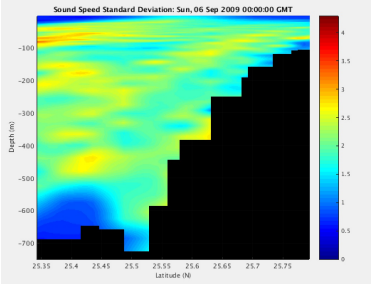

(j) Time 10

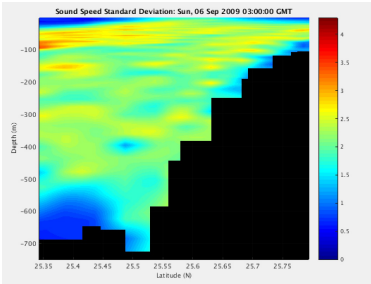

(k) Time 11

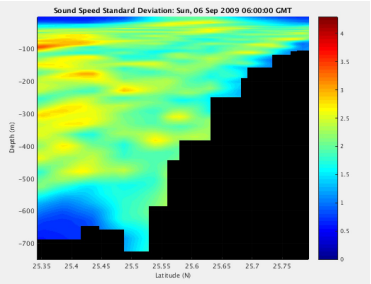

(l) Time 12

Figure 5-17: 2D Slice Sound Speed Standard Deviation

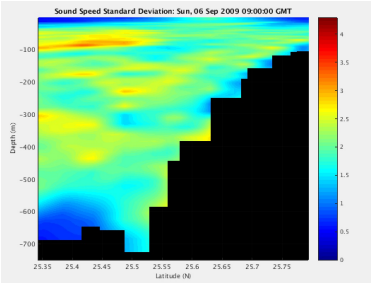

(m) Time 13

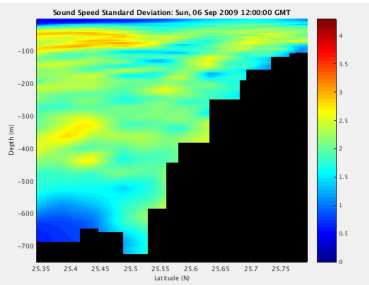

(n) Time 14

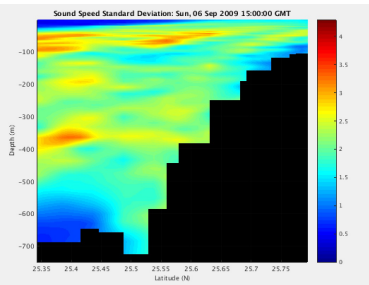

(o) Time 15

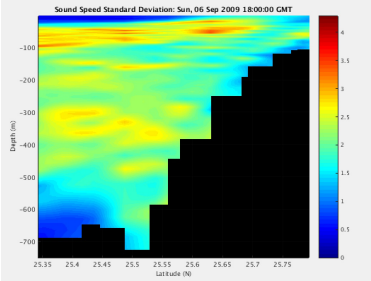

(p) Time 16

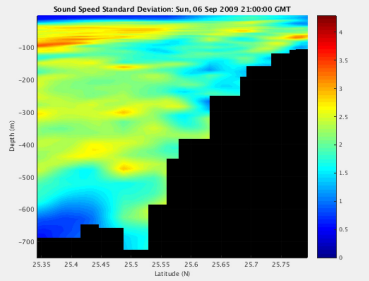

(q) Time 17

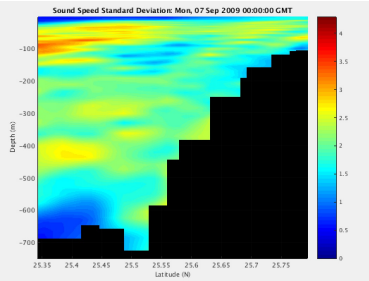

(r) Time 18

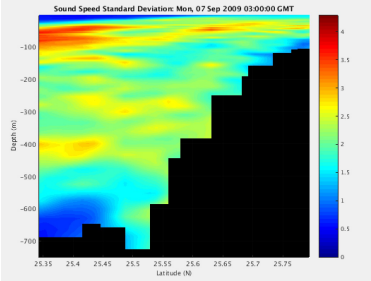

(s) Time 19

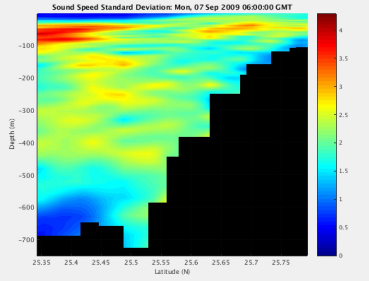

(t) Time 20

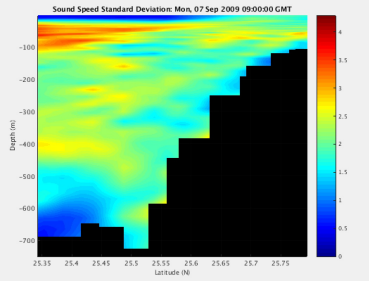

(u) Time 21

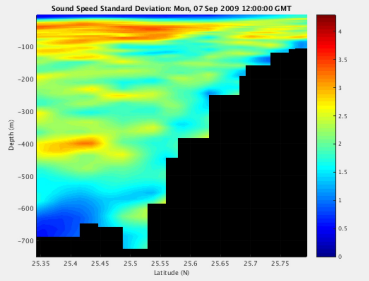

(v) Time 22

Figure 5-17: 2D Slice Sound Speed Standard Deviation

5.3.7 2D Acoustic Field Downslope Propagation

The temperature, salinity and sound speed fields shown in the previous sections display the variations between the realizations of the ensemble. Variations in the salinity fields as shown in Figure 5-13 display the effects of internal tides on the salinity field realizations, which appear as striations in the standard deviation fields. The evolution of the ensemble of ocean states was used as the temperature and salinity input into the 3D parabolic equation Peregrine code. For each ocean state the acoustic code was ran to generate a representative acoustic field for the 2D propagation downslope in the North Mein-Hua canyon. The region of these acoustic runs is shown along the red line that is within the region of acoustic study shown by the rectangular area in Figure 5-18.

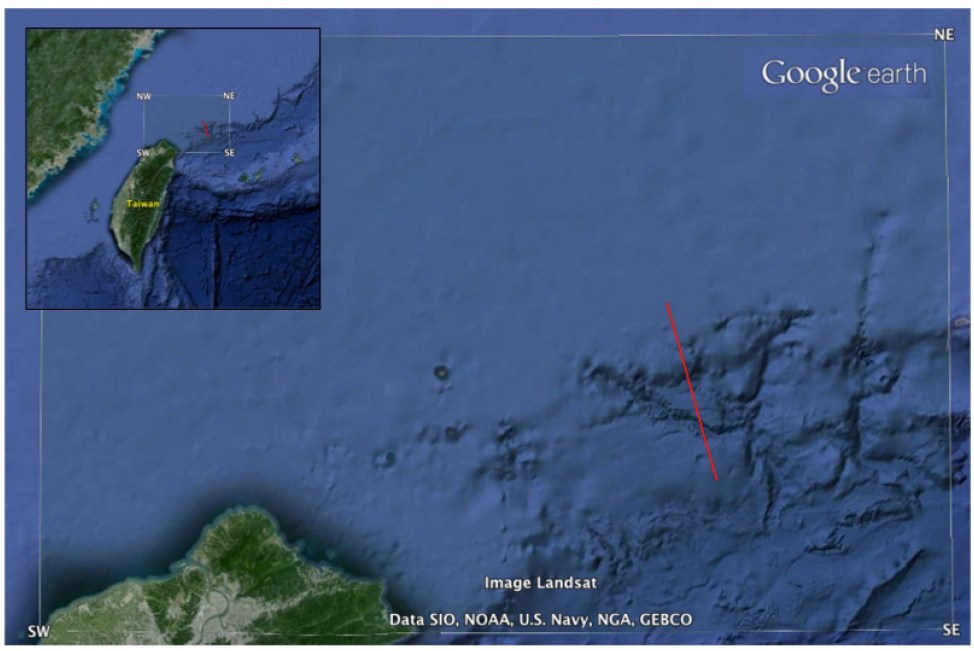

Figure 5-18: 2D Ocean Slice: Path of Acoustic Propagation

The downslope propagation was transmitted at a depth of 75m at a frequency of 150 hz originating at position with Longitude 122°40'52"E and Latitude 25°47'41"N for 50km. The upslope runs shown in the following section were also transmitted along the same path in the reverse direction originating from position with Longitude 122°48'44"E and Latitude 25°22'50"N. The upslope runs were also transmitted at the

same depth and frequency as the downslope runs. For the downslope runs each of the 19 realizations of the acoustic field plots for the final time interval are displayed in Figure 5-19. In these figures the uncertainties in the ocean field generate variations within the acoustic fields that will be analyzed using the CROM methodology.

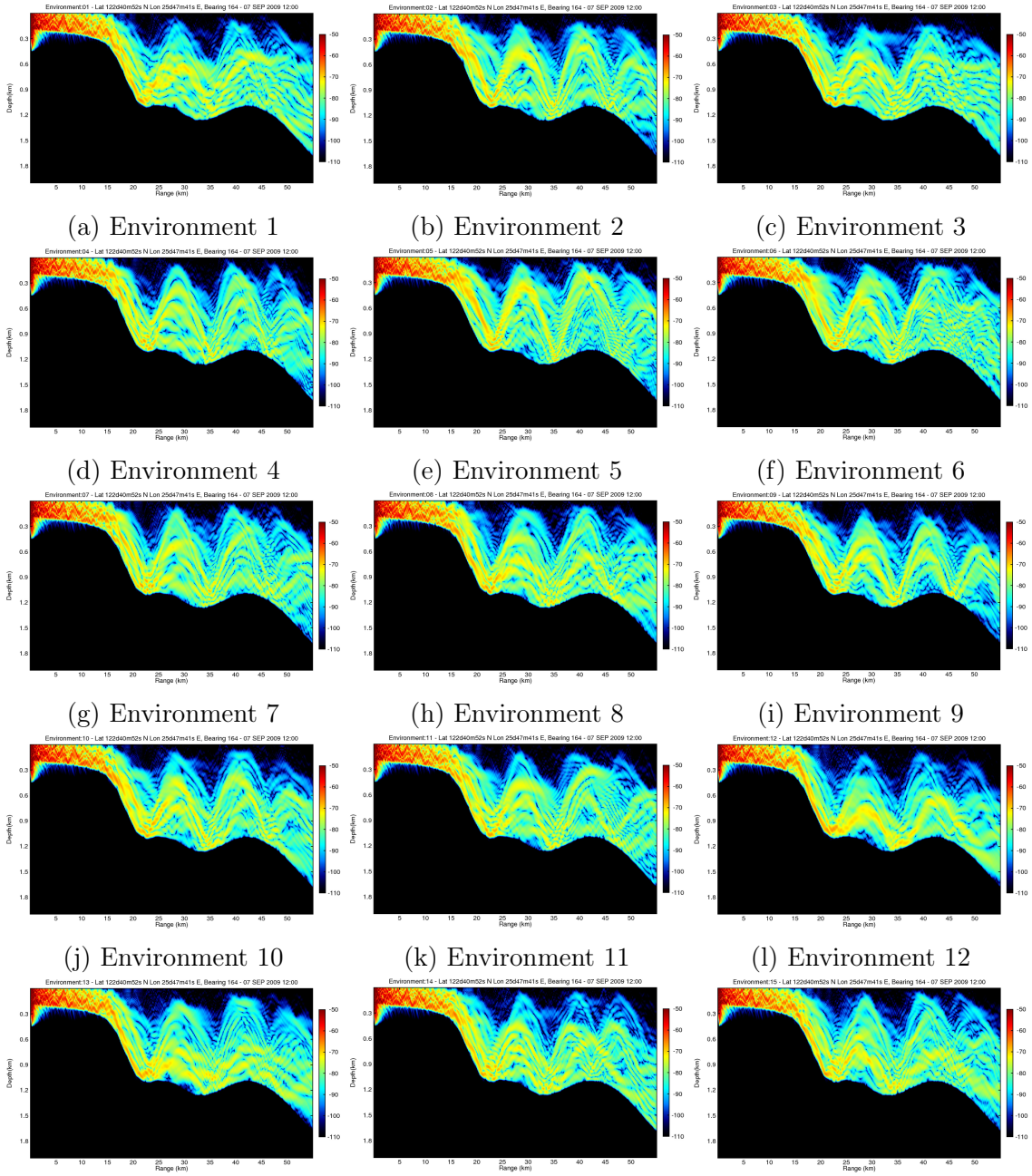

(a) Environment 1 (b) Environment 2 (c) Environment 3

(d) Environment 4 (e) Environment 5 (f) Environment 6

(g) Environment 7 (h) Environment 8 (i) Environment 9

(j) Environment 10 (k) Environment 11 (l) Environment 12

(m) Environment 13 (n) Environment 14 (o) Environment 15

Figure 5-19: Downslope 2D Slice Acoustic Field

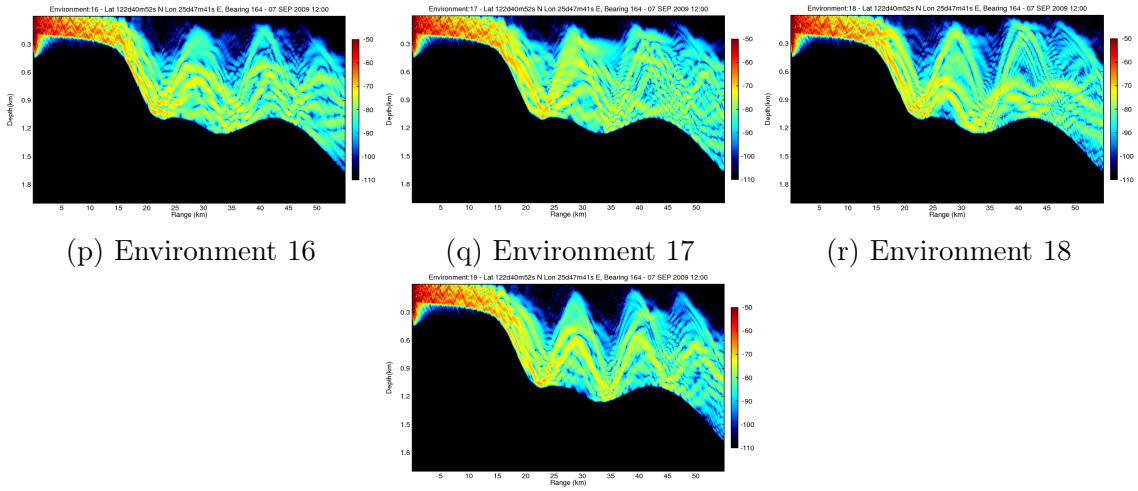

(p) Environment 16 (q) Environment 17 (r) Environment 18

(s) Environment 19

Figure 5-19: Downslope 2D Slice Acoustic Field

5.3.8 2D Acoustic Field Upslope Propagation

The 19 realizations for the upslope propagation at the final time interval are displayed in Figure 5-20.

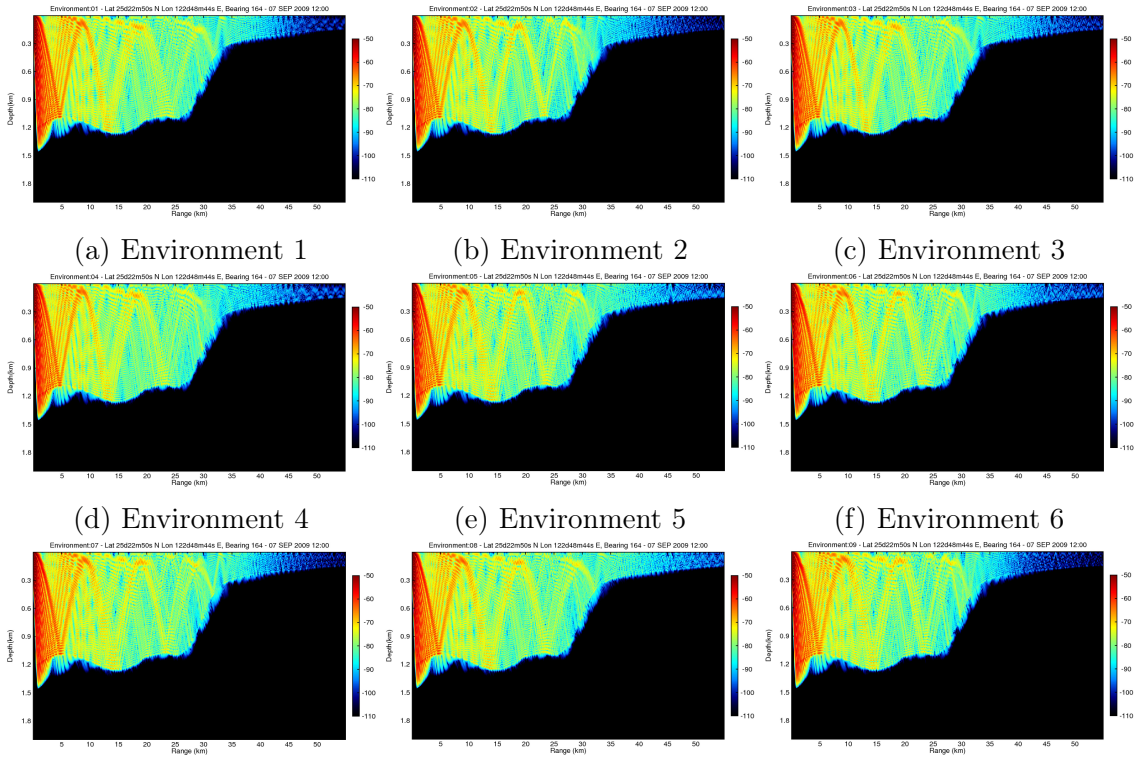

(a) Environment 1 (b) Environment 2 (c) Environment 3

(d) Environment 4 (e) Environment 5 (f) Environment 6

(g) Environment 7 (h) Environment 8 (i) Environment 9

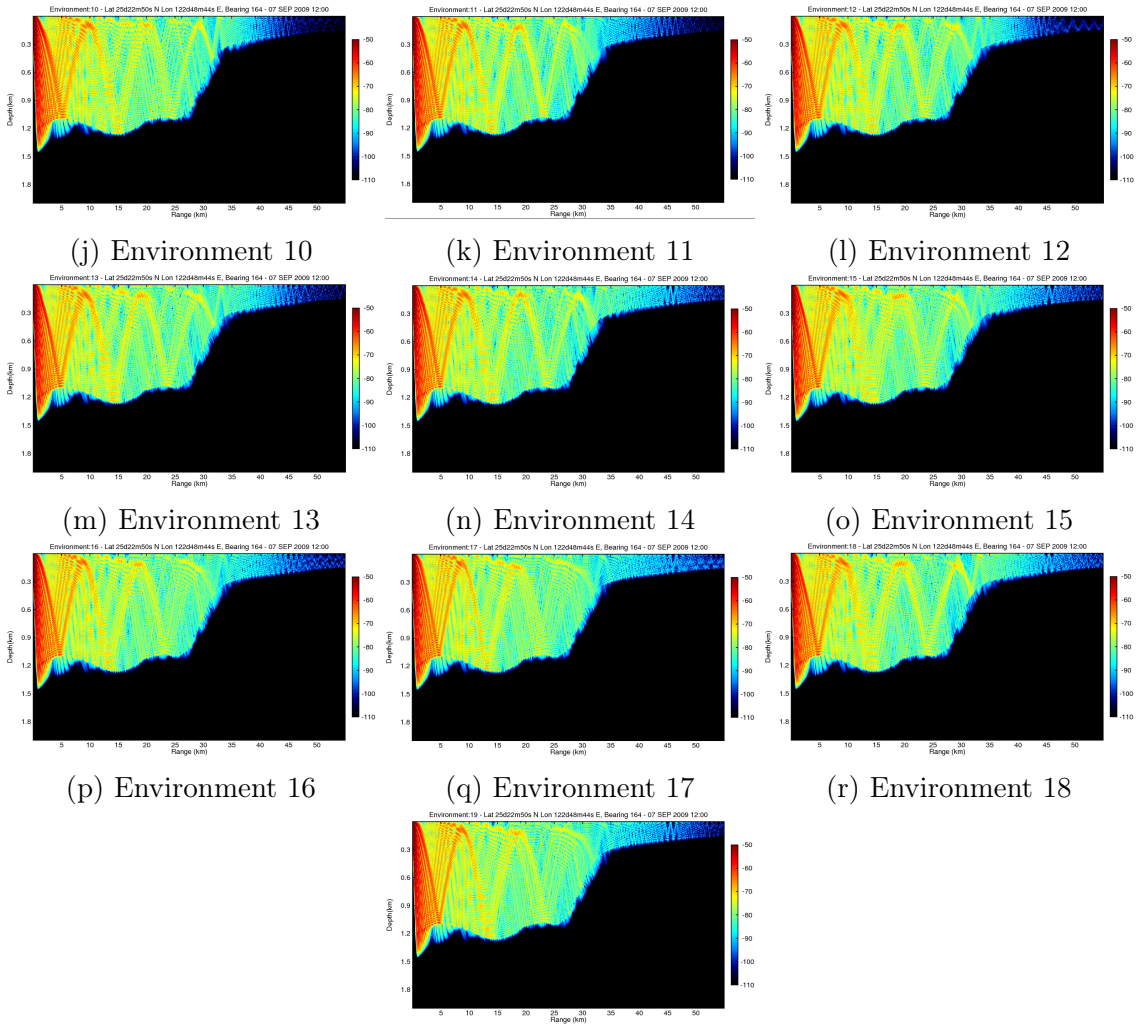

(j) Environment 10 (k) Environment 11 (l) Environment 12

(m) Environment 13 (n) Environment 14 (o) Environment 15

(p) Environment 16 (q) Environment 17 (r) Environment 18

(s) Environment 19

Figure 5-20: Upslope 2D Slice Acoustic Field

5.4 Transmission Loss Cluster Analysis

The analysis of the transmission loss data obtained from the from the various ocean state perturbations over the three and half day period can be seen to exhibit various characteristics that develop with range. The variation in transmission loss is more readily apparent for the downslope propagation than for the upslope acoustic fields. The cumulative transmission loss fields are plotted for the downslope and upslope ensembles in Figure 5-21. From the cumulative transmission loss plots it can be seen that there is a variation in the dB level of approximately 20 dB due to only the variation in the ocean fields. Depending on the state of the background environment

this variation in transmission loss could be tactically significant for counter detection purposes. Therefore, a better understanding of the variations caused by the ocean uncertainty is necessary. In order to better understand and quantify the relationship

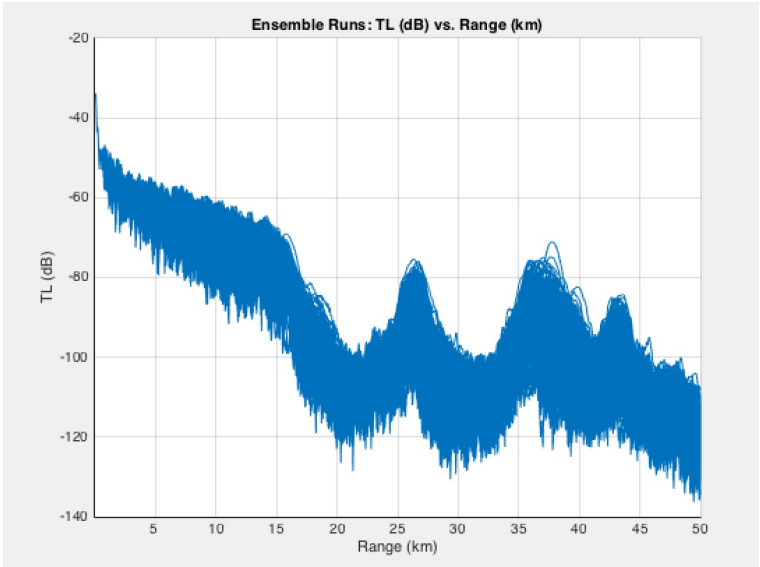

(a) Downslope Transmission Loss vs Range

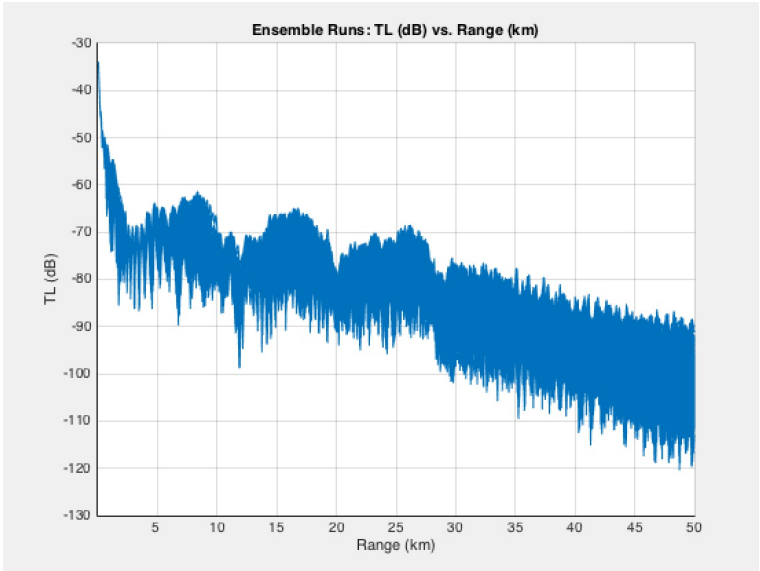

(b) Upslope Transmission Loss vs Range

Figure 5-21: Cumulative Transmission Loss for Downslope Ensemble and Upslope Ensemble

between the ocean variability and the resulting acoustic field a cluster based analysis is performed. As discussed in Chapter 4 cluster analyses have been previously performed on stochastic flow simulations in order to analyze the results and draw conclusions

on the structures of the resulting data. Inferences can be made on the temporal relationships between the various flow states and interaction between mechanisms within the flow. For example cluster based reduced order modeling was employed in the examination of the flow field induced by the wake of a high speed train. The approach used in the analysis of the high speed train wake was classified as cluster based reduced order modeling. This technique is used to group the data using a k-means clustering analysis. Next, an analysis of the temporal relationship between the cluster transitions is performed, which is modeled as a Markov Process (Östh et al., 2015). This method can mine the data to extract the various flow structures from the seemingly random data. The cluster based reduced order modeling methodology will be employed to quantify the uncertainties within the transmission loss fields due to the uncertainty contained withing the evolution of the ocean temperature and salinity fields.

5.4.1 Transmission Loss Clustering

The first step in the CROM methodology is to cluster the data. Out data set contains the ensemble of 19 perturbations over 22 three hour time intervals. The clustering technique employed is k-means clustering. The k-means clustering employs correlation distance measure and the number of clusters is determined using the elbow method. The data is first clustered using cluster values from 1-10. The clusters for each iteration of the downslope propagation can be seen in Figure 5-22 and in Figure 5-23 for the upslope propagation. For the low cluster values it can be seen that the range of data is not well represented and for the higher cluster plots there are regions where the clusters are overlapped. The elbow method is employed to determine the optimal cluster value that best represents the division of transmission loss clusters.

The determination of the optimal number of clusters is one of the most difficult aspects of cluster analysis. The elbow method is one approach that seeks to determine the optimal number of clusters by sequentially plotting the sum of the distance measures for all data points of each cluster value. The ideal number of clusters will

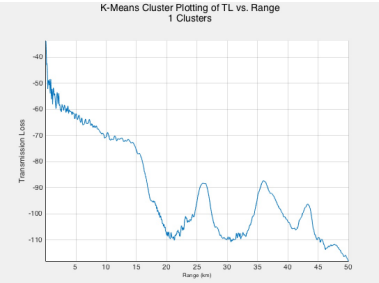

(a) Cluster 1

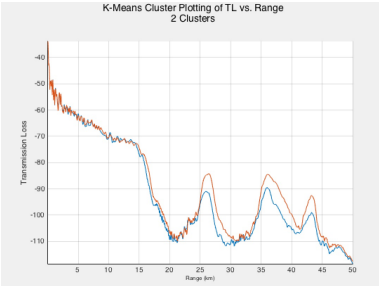

(b) Cluster 2

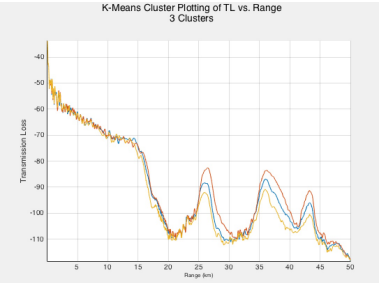

(c) Cluster 3

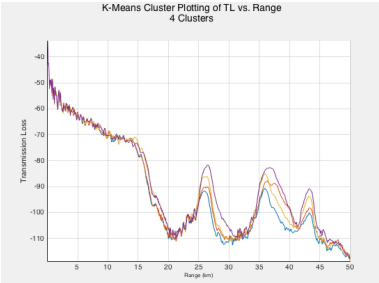

(d) Cluster 4

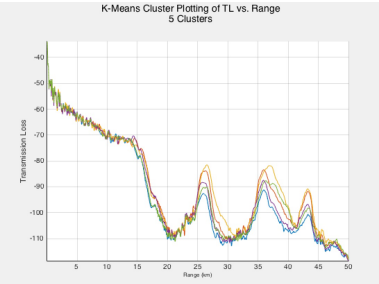

(e) Cluster 5

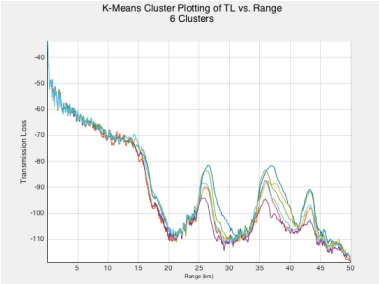

(f) Cluster 6

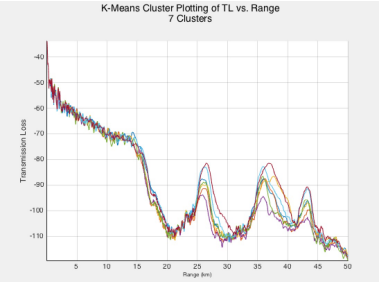

(g) Cluster 7

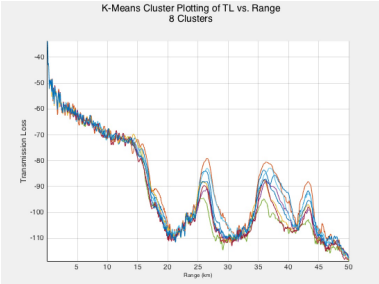

(h) Cluster 8

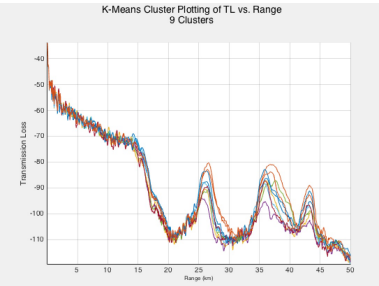

(i) Cluster 9

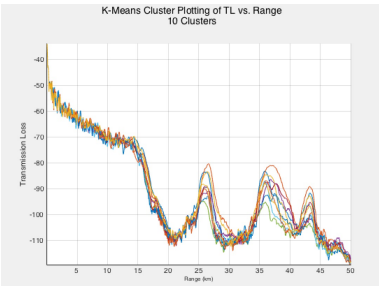

(j) Cluster 10

Figure 5-22: Downslope Transmission Loss Clusters

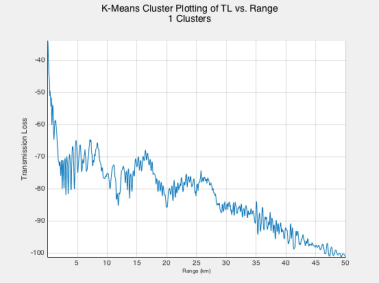

(a) Cluster 1

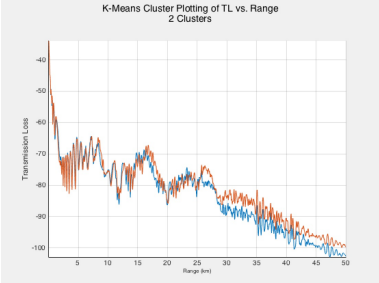

(b) Cluster 2

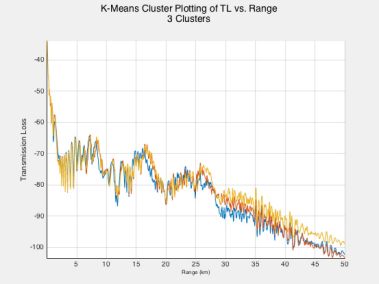

(c) Cluster 3

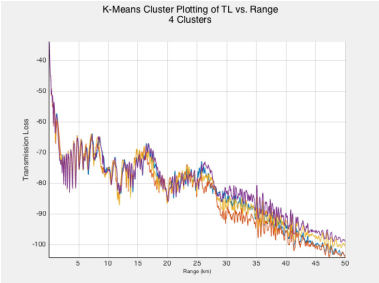

(d) Cluster 4

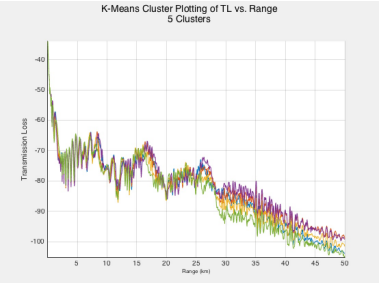

(e) Cluster 5

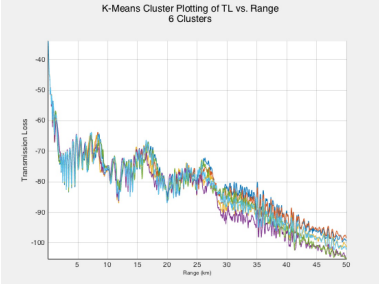

(f) Cluster 6

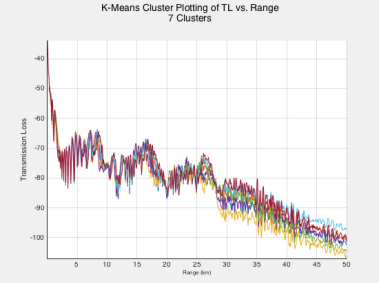

(g) Cluster 7

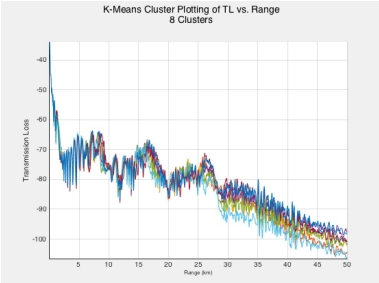

(h) Cluster 8

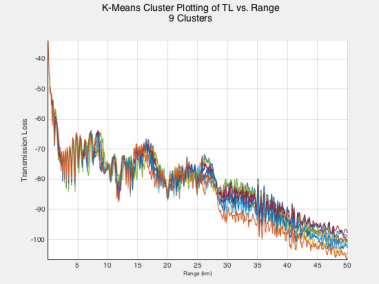

(i) Cluster 9

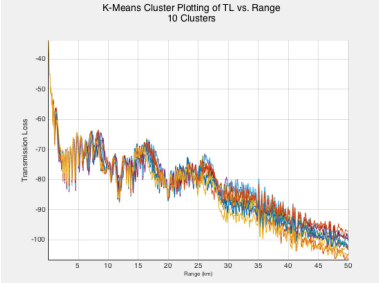

(j) Cluster 10

Figure 5-23: Upslope Transmission Loss Clusters

be the cluster where a change in cluster value causes a reduced change in the sum of distances. The cumulative sum of distances are plotted in Figure 5-24.

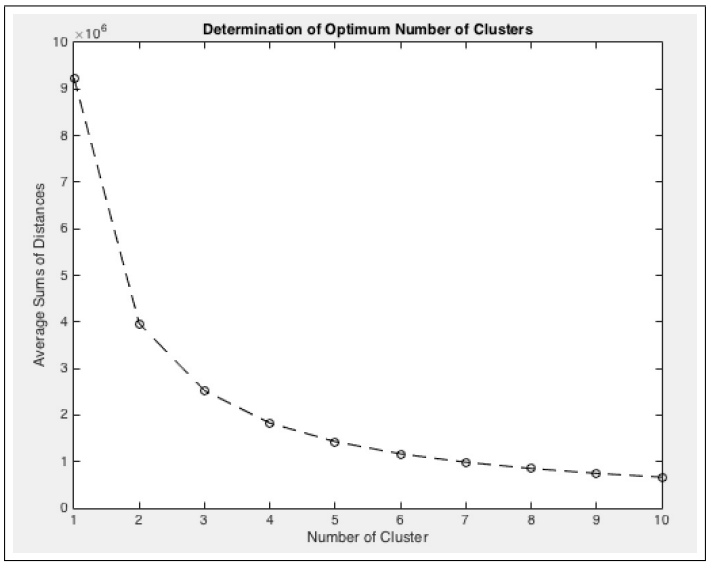

Figure 5-24: Cluster Cumulative Sum of Distances Plot

The elbow of the curve can be identified at approximately 2-4 clusters by inspection of the sum of distances plot. A more rigorous and heuristic identification of the optimal number of clusters can be found using the gap statistic developed by (Tibshirani et al., 2001) for DNA analysis. The gap statistic utilizes a compactness score for the intra cluster data based on the variance of the dataset cluster J_{c_k}. The $\log(J_{c_k})$ is compared to generated reference distributions that are each evenly distributed within the bounds of the original dataset. The estimate of the uniform distribution is determined through Monte Carlo sampling of B generated uniform distributions and is represented by the term $E_n^*\{\log(J_{c_k})\}$. The gap statistic equation is displayed below.

$$\mathrm{Gap}_n(k) = E_n^*\{\log(J_{c_k})\} - \log(J_{c_k}) \tag{5.5}$$

The $\log(J_{c_k})$ is determined for each cluster value and compared to the reference distribution. The tolerance of this procedure s_k is dependent on the standard deviation of the reference distribution $\mathrm{sd}(k)$.

$$s_k = (\sqrt{1 + 1/B})\mathrm{sd}(k) \tag{5.6}$$

The cluster value with the maximum gap value accounting for the tolerance of the reference distribution represents the elbow of the curve. From this the optimal number of clusters can be determined using equation 5.7.

$$\text{Gap}(k) \geq \text{Gap}(k+1) - s_{k+1} \tag{5.7}$$

An example cluster gap statistic obtained from the transmission loss data set can be seen in Figure 5-25. In this example the optimal number of clusters is 3, which

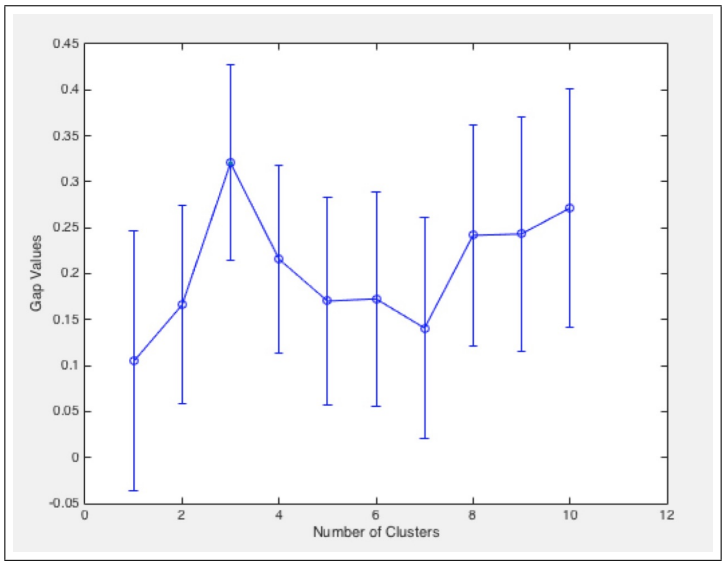

Figure 5-25: Cluster Gap Statistic Plot

checks with the expected cluster value determined from the observation of the elbow point on the sum of distances plot in Figure 5-24. The optimum number of clusters is determined through analysis of the Gap Statistic plot. Cluster 3 represents the smallest cluster k where the subsequent cluster 4 has a gap statistic value less than or equal to cluster 3 and this difference is greater than the tolerance s_k. Therefore, the datasets were clustered using a k value of 3. The upslope and downslope transmission loss cluster plots can be seen in Figure 5-26 The plots in Figure 5-26 incorporate all of the perturbations across all of the time intervals. The data was additionally clusters at each individual time step for all the perturbations. The upslope clustered data at the final time interval can be seen in Figure 5-27. The downslope clustered data can be seen in Figure 5-28. From analysis of these clustered plots the data can be dis-

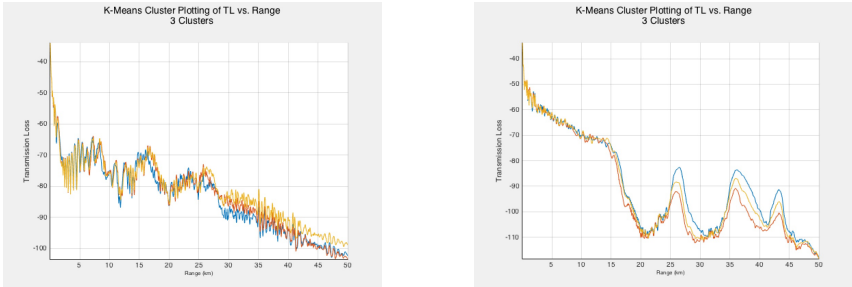

(a) Upslope (b) Downslope

Figure 5-26: Transmission Loss vs. Range Cluster Plots (k=3)

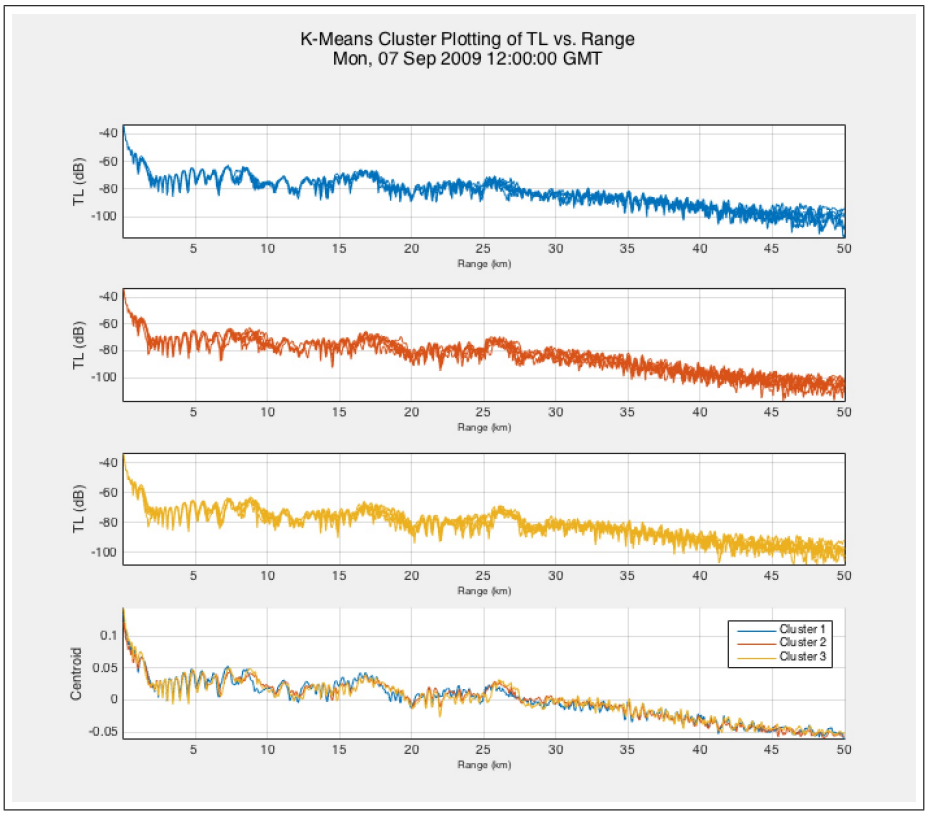

Figure 5-27: Upslope Clustered Data at Final Time Interval

tilled to understand the significance of the effect of the ocean field uncertainty. The first observation is that the deviation between clusters is greater for the downslope transmission loss as compared to the upslope losses. The reason for this is most likely due to number of interactions with the bottom. The upslope acoustic propagation is reflected off of the surface and bottom several more times than the downslope propagation due to the geometry of the waveguide. Therefore, the downslope propagation

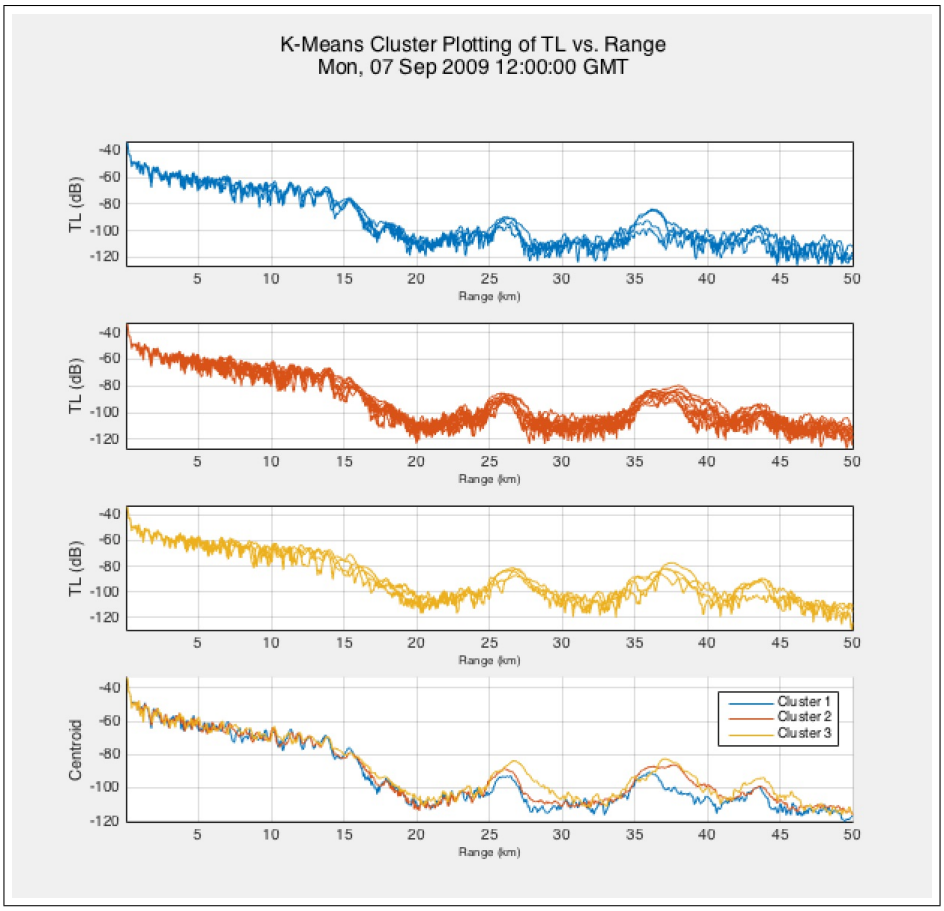

Figure 5-28: Downslope Clustered Data at Final Time Interval

is influenced by the uncertainties in the ocean field for greater lengths, which enhanced the effects on the resulting acoustic field at further ranges. Additionally, the acoustic field uncertainties are enhanced in the vicinity of bathymetric features. In regions where there acoustic field encounters rising elevation around ranges of 25-27 km and 35-40 km for the downslope propagation in Figure 5-28 the uncertainty in the transmission loss is greatest. The significance of the variations in the transmission loss is that variations of 5-15 dB between clusters exist and extend over ranges of approximately 5 km. Incorporating these acoustic field uncertainties into counter detection tactical decision aides can enhance the operational awareness of acoustic vulnerabilities.

5.5 Probability of Detection Decision Aid

5.5.1 Gaussian Probability of Detection Plots

The acoustic fields can now be employed to generate probability of detection plots with increased fidelity by accounting for the uncertainty due to the the ocean field. The first method will utilize the raw acoustic field ensembles and perform a Gaussian analysis to determine the probability of detection. This process utilizes the ensemble of the acoustic field at each range and fitted a Gaussian curve that represents the uncertainty in the acoustic field. The Gaussian field is then compared to a background noise level to develop the signal to noise ratio that will provided the basis for comparison to determine the probability of detection. The upslope transmission loss probability of detection plot can be seen in Figure 5-29.

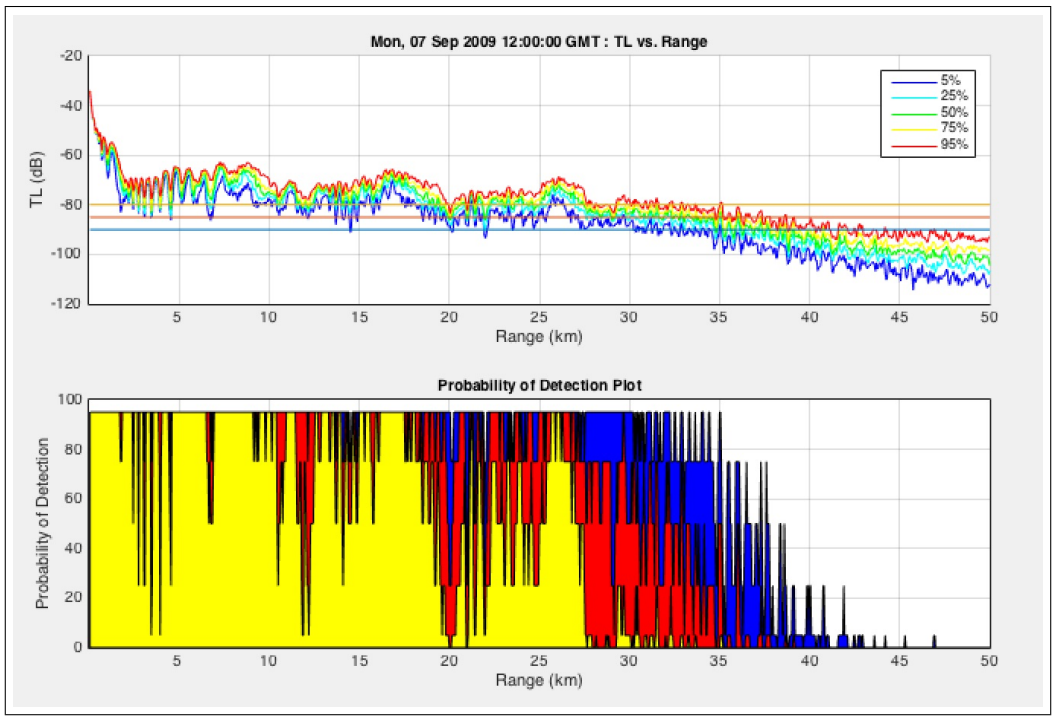

Figure 5-29: Upslope Transmission Loss and Gaussian Probability of Detection Plot with Constant Background Noise

The upper plot in Figure 5-29 represents the range of percentiles of the acoustic field dataset, and the three horizontal lines at -80dB, -85dB and -90dB represent possible constant background noise profiles. The probability of detection plot is generated

by comparing each transmission loss curve to the three noise profiles and generates a probability based on the percentile of possible transmission loss fields that exhibit a signal to noise ratio that would increase the chances of detection. In the upslope propagation the acoustic field exhibits an approximately 5-10 dB variation growing slightly at further ranges. The downslope probability of detection plot develops regions of variation that range from 20-30 dB along the shelf-break region. These variations occur at longer ranges than the upslope propagation and represent ranges where the probability of detection varies. The downslope probability of detection curve is shown in Figure 5-30.

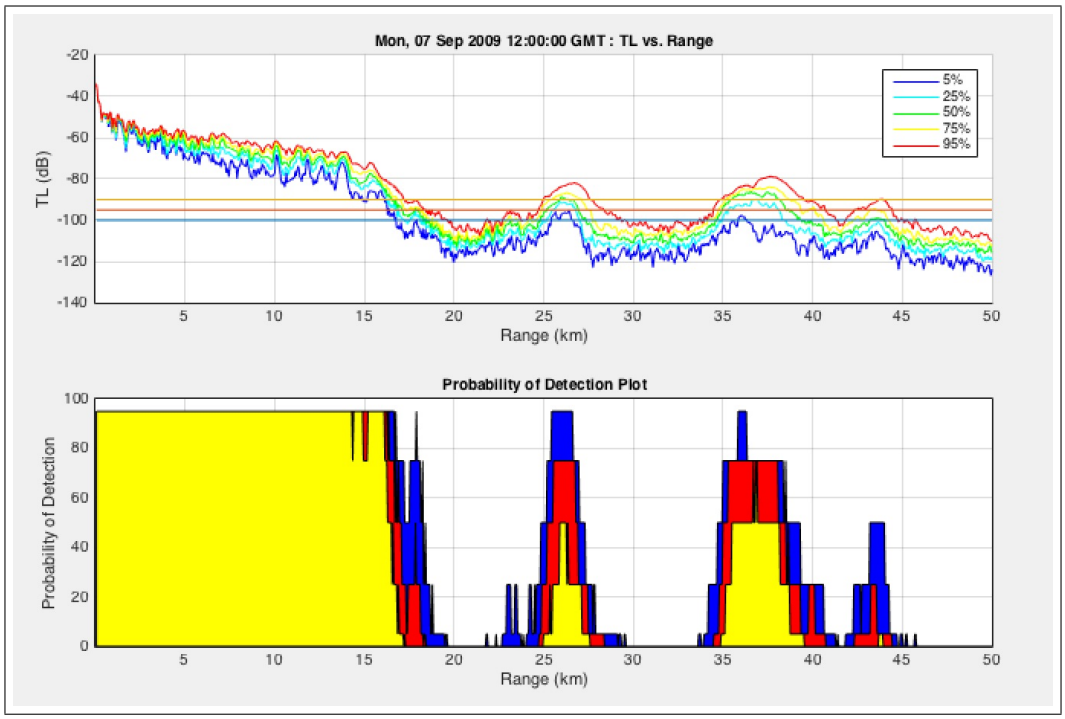

Figure 5-30: Downslope Transmission Loss and Gaussian Probability of Detection Plot with Constant Background Noise

In the downslope propagation the steepest slope of the shelf-break region occurs at approximately 20 km. In the region from 22-30 km the transmission loss exhibits increased uncertainty, which is reflected in the probability of detection plot with various probabilities of detection for each of the potential background profiles. The red, blue and yellow background profiles in the upper plots correspond with the respective colors in the lower probability of detection plots in the lower plots. This

enables the evaluation of the probability of detection with respect to the uncertain background noise models. The noise profile can be easily varied to represent areas where noise levels change due to increased ambient levels due to weather effects, or shipping and fishing traffic.

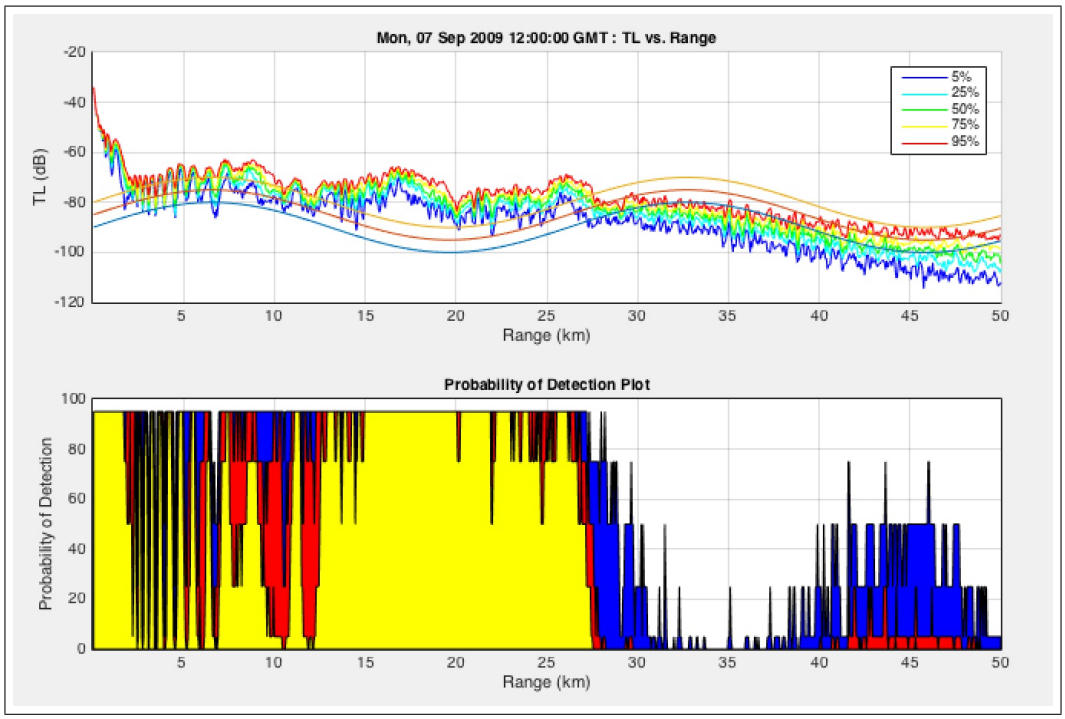

Figure 5-31: Upslope Transmission Loss and Gaussian Probability of Detection Plot with Variable Background Noise

An example variable noise profiles are plotted using a simple sine wave profile to demonstrate this for the upslope propagation in Figure 5-31 and for the downslope propagation in Figure 5-32. As seen in these figures the variation in the noise profile can significantly alter the probability of detection ranges.

The Gaussian probability of detection plots are useful tools to enhance the operators understanding the potential zones of detection with an associated probability. This enables an understanding of the forecast acoustic field vulnerabilities that can be exploited operationally during the planning phase or in real time for a more thorough situational awareness.

The Gaussian probability of detection plots require that the entire acoustic field dataset with all perturbations be utilized to generate the detection plot. As outlined

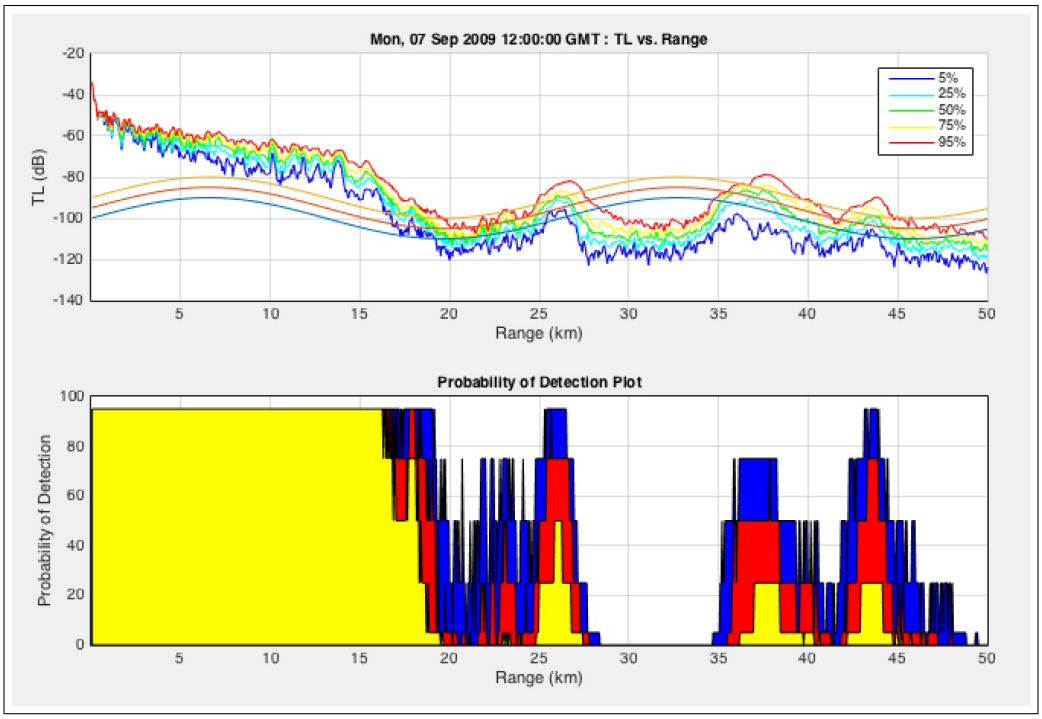

Figure 5-32: Downslope Transmission Loss and Gaussian Probability of Detection Plot with Variable Background Noise

in Chapter 4 the cluster based analysis will be proven to provide comparable fidelity to Gaussian probability of detection plots utilizing the data of the cluster centroids.

5.5.2 Clustered Probability of Detection Plots

The clustered probability of detection plots will represent the same dataset through the use of the clustered centroids. The probability of detection will be determined from the cumulative cluster probability determined by the percentage of transmission loss fields contained within the cluster. Therefore, the number of clusters with values above the noise profile represent the probability of the detection at that range. The clustered probability of detection for the upslope and downslope propagation with a constant noise profile is displayed in Figure 5-33 and Figure 5-34 respectively.

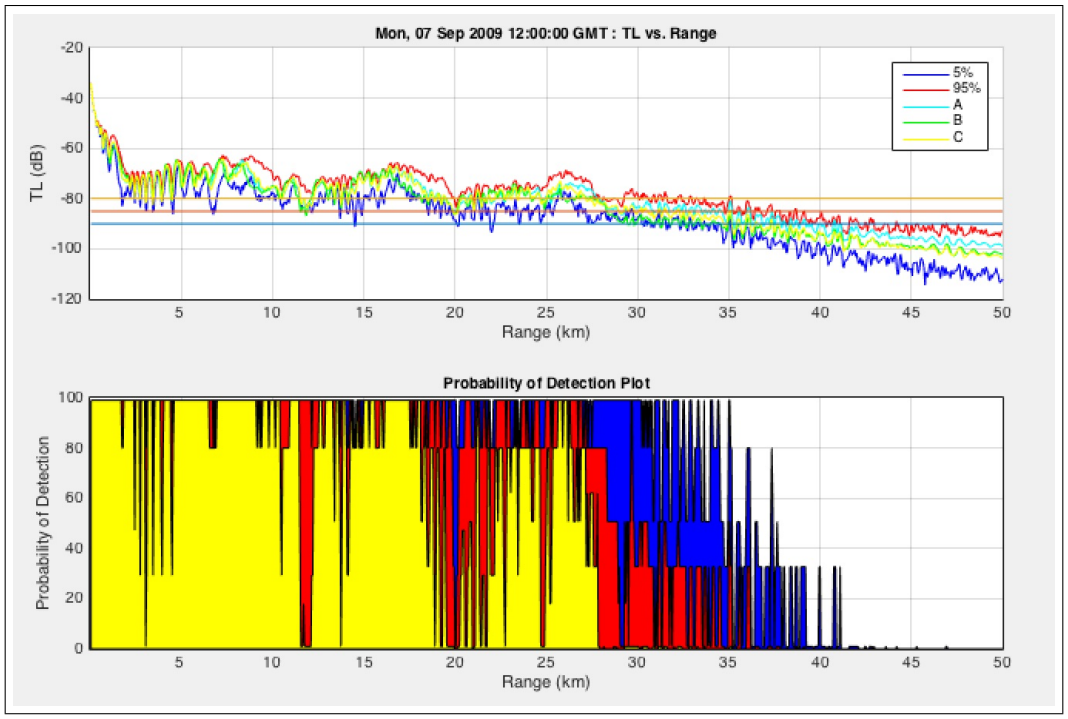

Figure 5-33: Upslope Transmission Loss and Clustered Probability of Detection Plot with Constant Background Noise

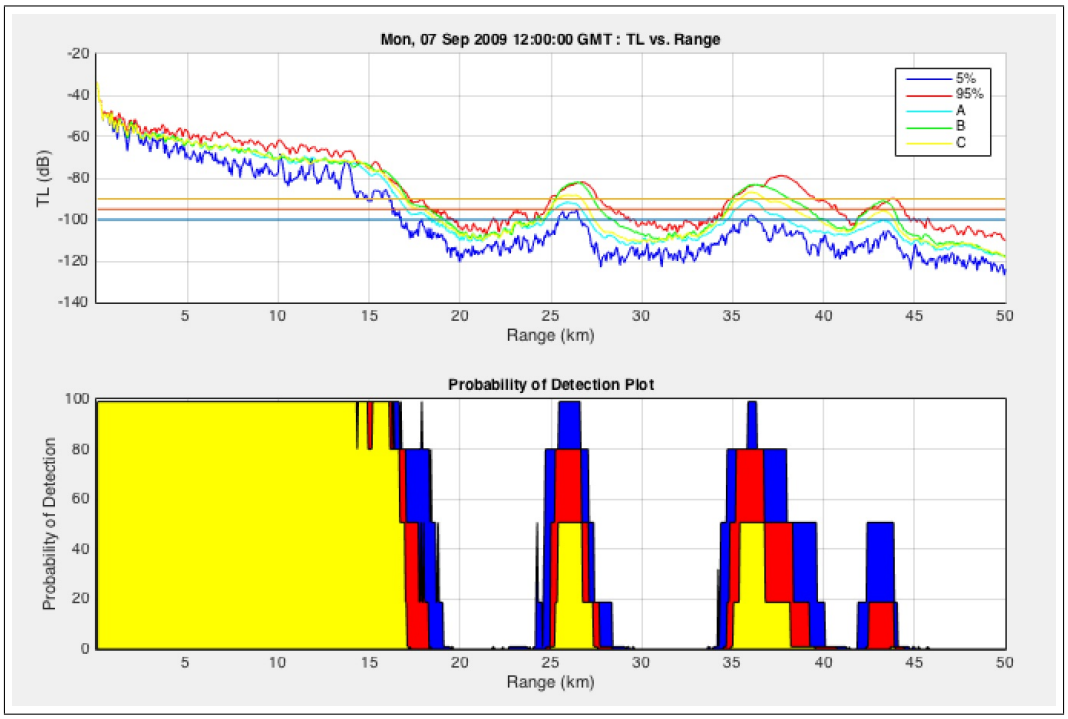

Figure 5-34: Downslope Transmission Loss and Clustered Probability of Detection Plot with Constant Background Noise

The clustered plots include the envelope of the dataset at the 5th and 95th percentile to approximately bound the dataset and the clusters are plotted and labeled as A, B and C. By comparison of Figures 5-29 and 5-30 to Figures 5-33 and 5-34 respectively it is clear that the probability of detection plots generated from the clustered data are equally representative of the variation in detection ranges as can be seen in the Gaussian plots.

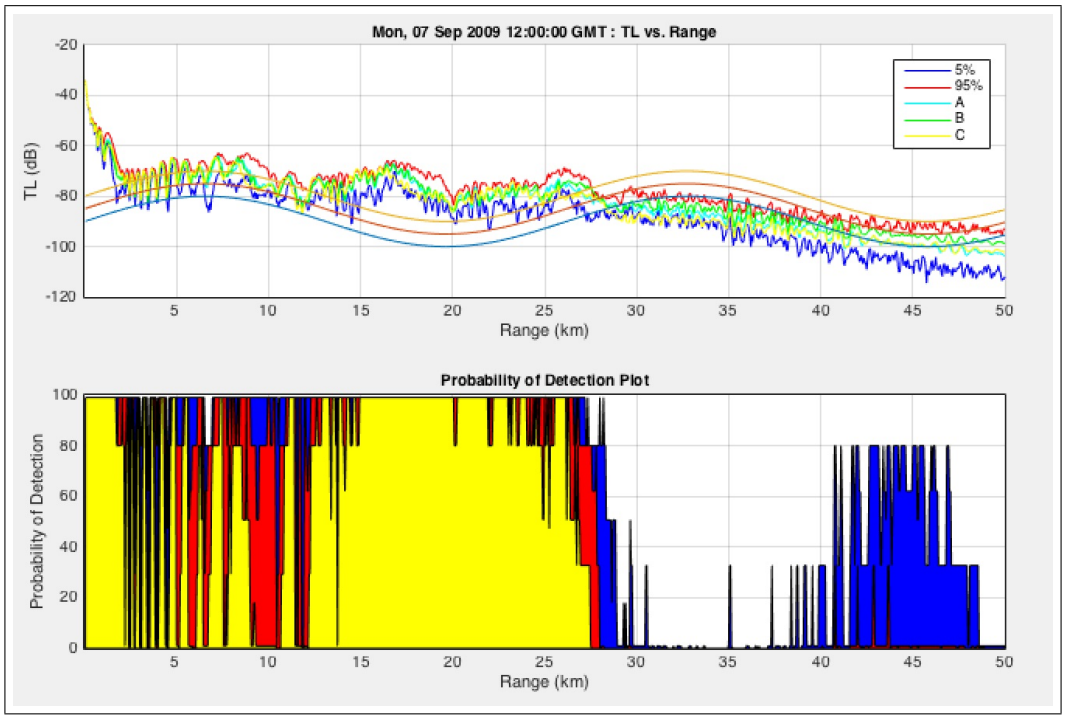

Figure 5-35: Upslope Transmission Loss and Clustered Probability of Detection Plot with Variable Background Noise

The probability of detection plots were also generated for variable background noise profiles using the clustered datasets. The clustered datasets with variable background noise can be seen in Figures 5-35 and 5-36 for upslope and downslope propagation respectively. Again, when compared to the Gaussian probability of detection plots in Figures 5-31 and 5-32 the results of the clustered plots are equally representative across all ranges of the probability of detection plots.

The benefit of using the clustered data sets is that these fields can be equally representative of the detection probabilities as the Gaussian fields, while only utilizing a fraction of the dataset to generate these representations. The clustered dataset uses

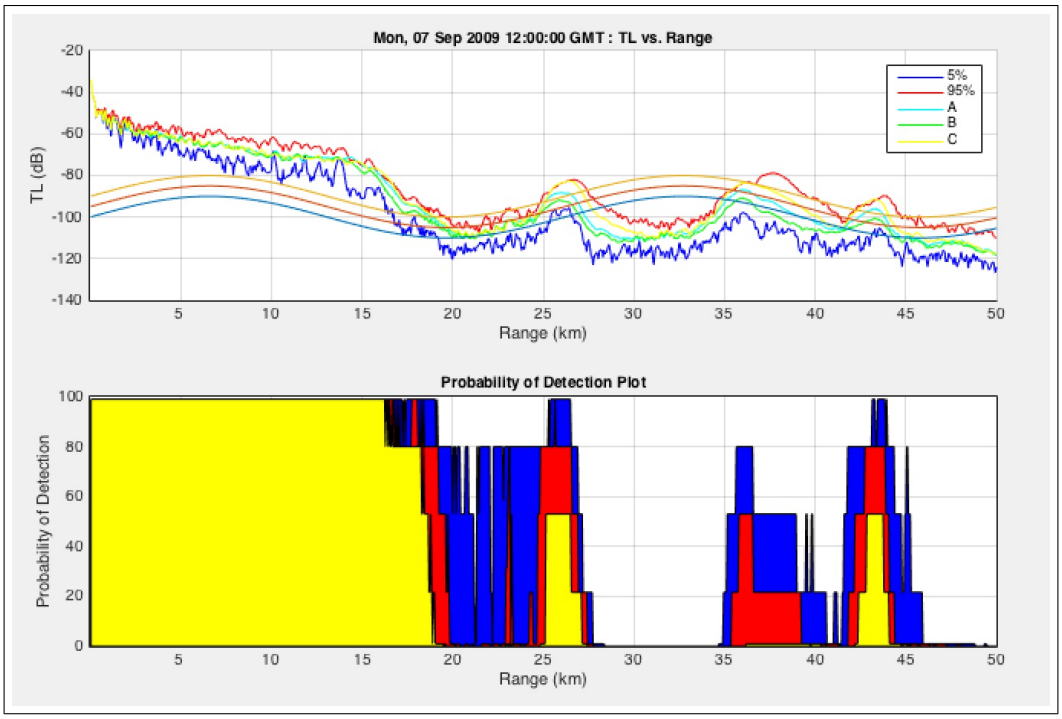

Figure 5-36: Downslope Transmission Loss and Clustered Probability of Detection Plot with Variable Background Noise

three arrays containing the clustered centroids, as compared to the 19 arrays of the perturbed dataset for each of the 22 time intervals. If a larger initial ensembles dataset was used this an even greater reduction would be possible. Additionally, the Markov process representation can use the clustered detection plots over an expanded time interval with the same clustered centroid groups to describe the expected fields with their associated uncertainty.

5.6 Acoustic Field Markov Process Representation

The Markov Process representation as described in Chapter 4 can be utilized to extend the predictive capability of the uncertain acoustic fields. The Markov process is defined by the cluster transition matrix. The cluster transition matrix is determined by evaluating the probability of transition between clusters from one time step to the next. The evaluation of cluster transitions can be used to determine the cluster transition matrix. In figure the 5-37 the most common cluster of each ensemble and

the mean cluster for each ensemble are represented at each time interval. The cluster

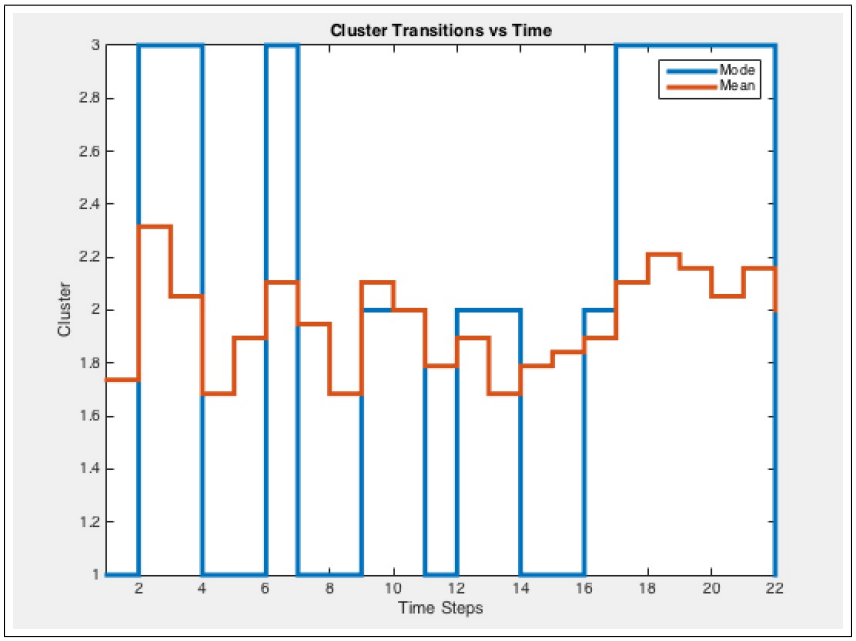

Figure 5-37: Cluster Transitions vs. Time

transition matrix, P_{jk} utilizes the analysis of the average cluster transitions for each ensemble to determine the probabilities of transition. The values of the cluster transition matrix can be seen in Figure 5-38.

$$\begin{vmatrix} 1/6 & 1/2 & 1/3 \\ 1/3 & 1/3 & 1/3 \\ 2/9 & 1/9 & 2/3 \end{vmatrix}$$

Figure 5-38: Cluster Transition Matrix

The cluster transition matrix can also be graphically represented in the Cluster Transition Diagram format described in Figure 4-2. The Cluster Transition Diagram for the example described by the Cluster Transition Matrix from Figure 5-38 can be seen below in Figure 5-39. The knowledge of the expected probabilities of cluster transition can be used to determine the likelihood of a specific clusters occurrence over

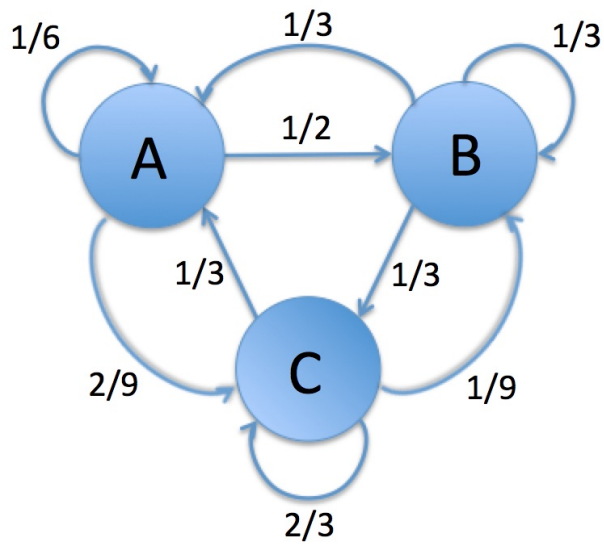

Figure 5-39: Cluster Transition Diagram

the different time steps. This information can be employed to generate estimations of the forecast probability of detection plots with incorporated uncertainty estimation.

5.7 2D Ocean Acoustic Field Conclusions

The 2D acoustic field uncertainty analysis is able to provide enhanced probability of detection plots. These plots are able to highlight the range of acoustic field variation that arises from the uncertainty in the ocean fields. Ranges where large bathymetric variations exist generate the largest resultant variations in the acoustic field, which have the most significant effects on the probability of detection plots. In certain regions of high variability the clusters may not completely reflect the potential acoustic states. In regions exhibiting this high variability it may be beneficial to increase the number of clusters to better represent the acoustic modes that are developed due to the variations in the ocean field. Potentially, the optimum number of clusters could be recomputed in critical regions where higher variability is expected. However, the Gap Statistic technique is computationally expensive due to the size of the datasets and the fact that the computations must be completed for each possible cluster value.

Therefore, it would be computationally beneficial to keep these regions where the optimum clusters is recomputed narrow to reduce the computational cost. Next, these same techniques will be applied to the 4D ocean models and the 3D acoustic propagation.

Chapter 6

3D Ocean Acoustic Uncertainty Analysis

The same analysis techniques can be applied to fully 3D acoustic propagation utilizing the 4D ocean field forecasts. The 3D acoustic propagation can provide a horizontal assessment of the acoustic field to easily locate regions of reduced or enhanced probability of detection, which can be used for improved mission planning. The analysis techniques used to evaluate the effects of the forecast ocean variability on the resulting acoustic field will be the same methods used for the 2D slices in the previous chapter. The 4D ocean fields will be analyzed and plotted to demonstrate the enhanced variability along the critical shelf-break region. Next, the 3D acoustic propagation results will be plotted and clustered using the same general techniques used in the slice analysis. The clustered results will be then compared to Gaussian analysis of the ensemble of 3D acoustic field. Finally, the results will be used to demonstrate examples of the forecast probability of detection estimates for the ocean acoustic ensembles.

6.1 4D Ocean Field

The forecast ocean realizations are analyzed across the entire study area to the North East of Taiwan. The 4D ocean field variance is depth dependent and depth slices of the

temperature, salinity and sound speed fields are plotted to display these variations. The ocean fields representing the temperature, salinity and sound speed at various depths for the final time interval are displayed in Figures (6-1 - 6-4).

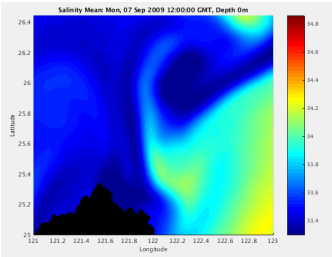

(a) Mean Salinity

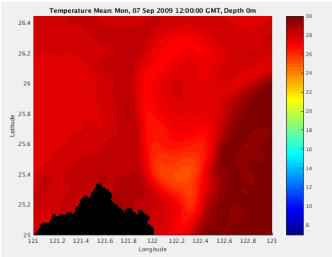

(b) Mean Temperature

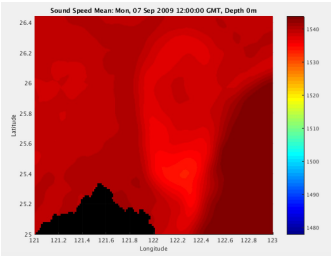

(c) Mean Sound Speed

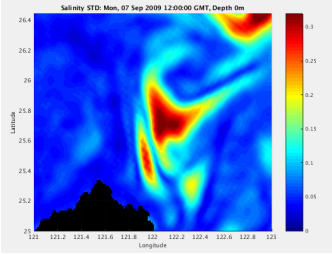

(d) Salinity STD

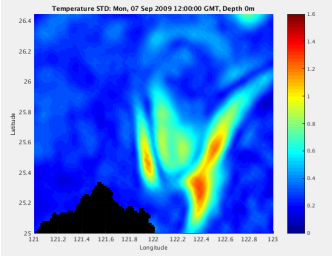

(e) Temperature STD

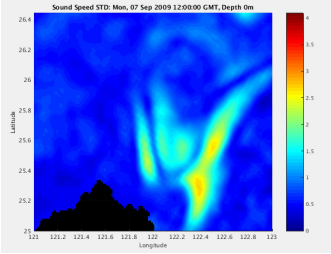

(f) Sound Speed STD

Figure 6-1: Surface Ocean Field Mean and Standard Deviation Profiles

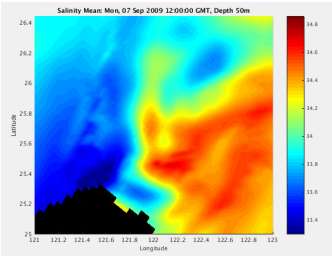

(a) Mean Salinity

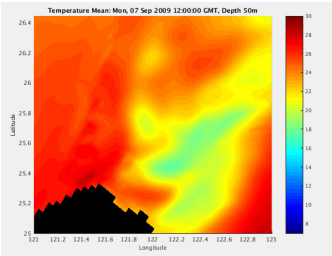

(b) Mean Temperature

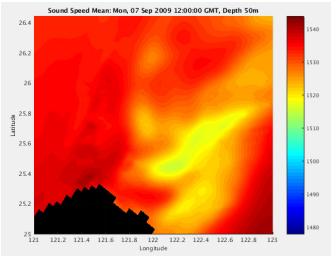

(c) Mean Sound Speed

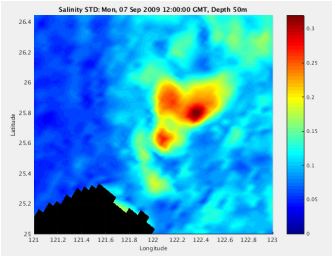

(d) Salinity STD

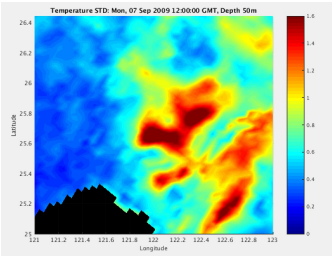

(e) Temperature STD

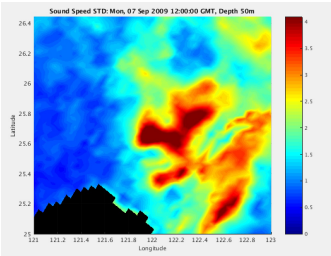

(f) Sound Speed STD

Figure 6-2: 50m Depth Ocean Field Mean and Standard Deviation Profiles

The sea floor is displayed as the blacked out region in each of the figures. As depth

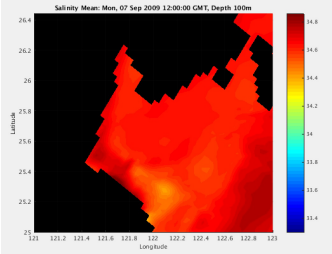

(a) Mean Salinity

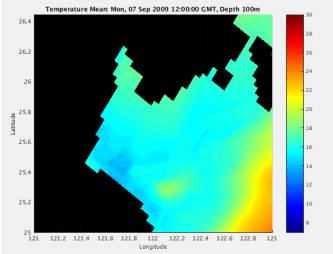

(b) Mean Temperature

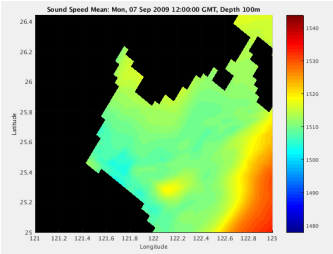

(c) Mean Sound Speed

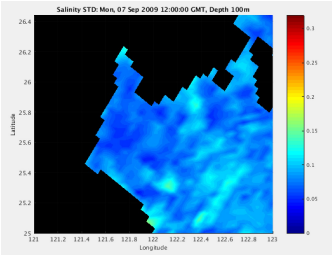

(d) Salinity STD

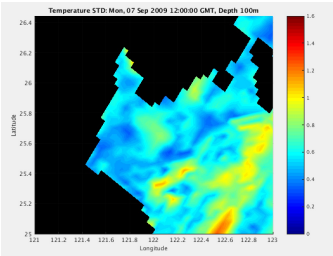

(e) Temperature STD

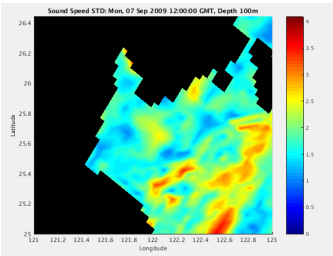

(f) Sound Speed STD

Figure 6-3: 100m Depth Ocean Field Mean and Standard Deviation Profiles

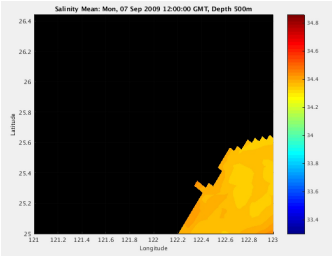

(a) Mean Salinity

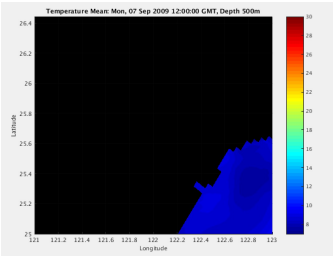

(b) Mean Temperature

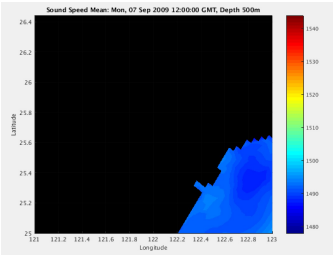

(c) Mean Sound Speed

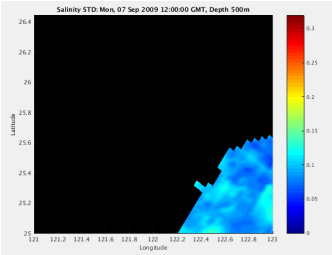

(d) Salinity STD

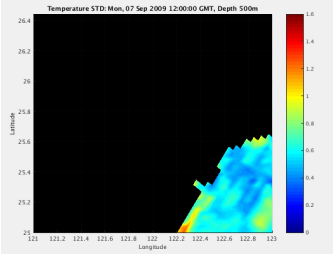

(e) Temperature STD

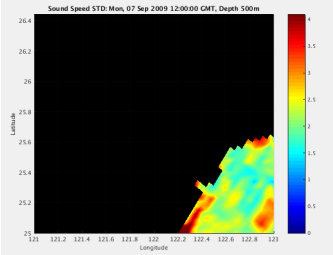

(f) Sound Speed STD

Figure 6-4: 500m Depth Ocean Field Mean and Standard Deviation Profiles

increases for each subsequent figure the variation in bathymetry the can be observed. These plots clearly demonstrate the increased variation of the ocean uncertainty along the critical shelf-break region. In Figures 6-1 and 6-2 the surface and 50m depth ocean fields exhibit their peak variance along the shelf-break. This region is also follows the direction of the Kuroshio current to the North West of the island of Taiwan, which

leads the the development of eddies which can be seen in the mean salinity and temperature fields in Figure 6-1. The dynamics of the ocean fields in this region where steep bathymetric slopes and ocean currents interact generate the uncertainty in the ocean field. The ensemble of 4D ocean realizations along this region are used to generate the 3D acoustic ensemble from the forecast uncertain ocean environment.

6.2 3D Acoustic Field

The 4D ocean ensemble was input to the 3D acoustic Peregrine code to generate the 3D acoustic field ensemble. The acoustic fields were then used to generate a transmission loss field for the region of study. The plot of the 3D acoustic propagation using a transceiver depth of 100m and a frequency of 150 Hz originating from the same source location as the 2D downslope propagation is plotted on the map in Figure 6-5. In Figure 6-5 the propagation is displayed and the range of transmission loss is shown

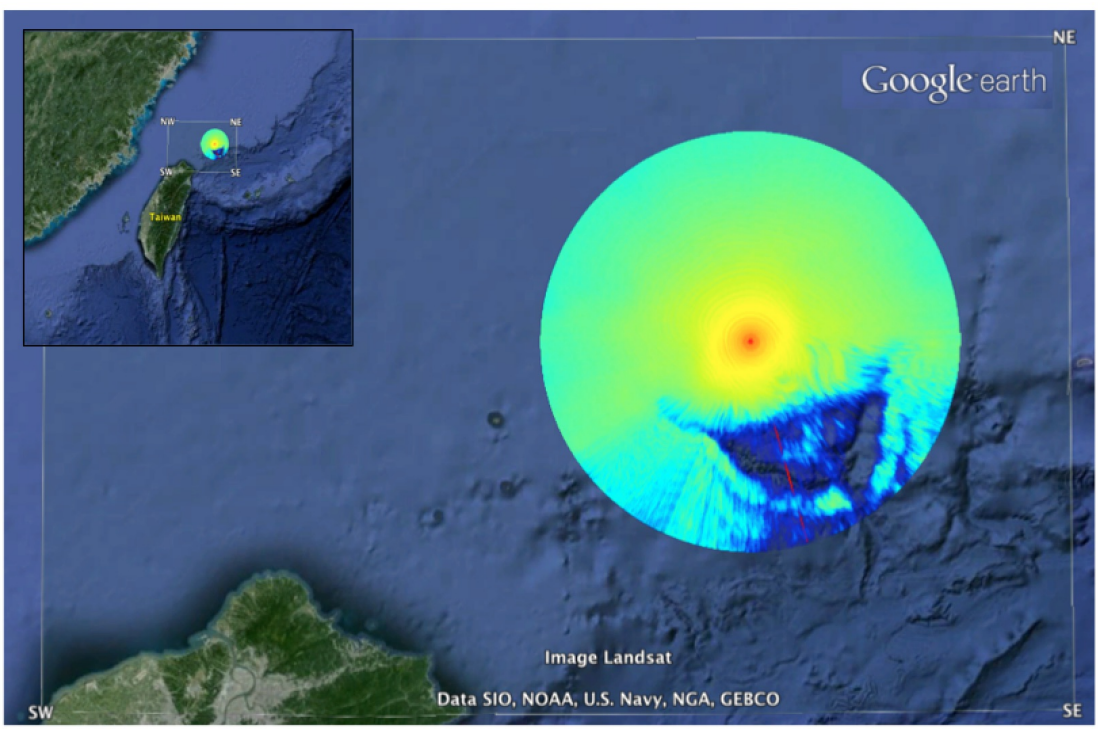

Figure 6-5: 3D Acoustic Propagation Along Shelf-Break Region

down to -120 dB. This plot displays the expected propagation with an extremely low

background noise level. In the Figure 6-6 the background noise is assumed to be at a level of -90 dB, which limits the range of the sound propagation to less than 50 km, which is computed and more accurately displays the bounds of the propagation. From analysis of Figure 6-6 it is evident that the propagation is greatly reduced due

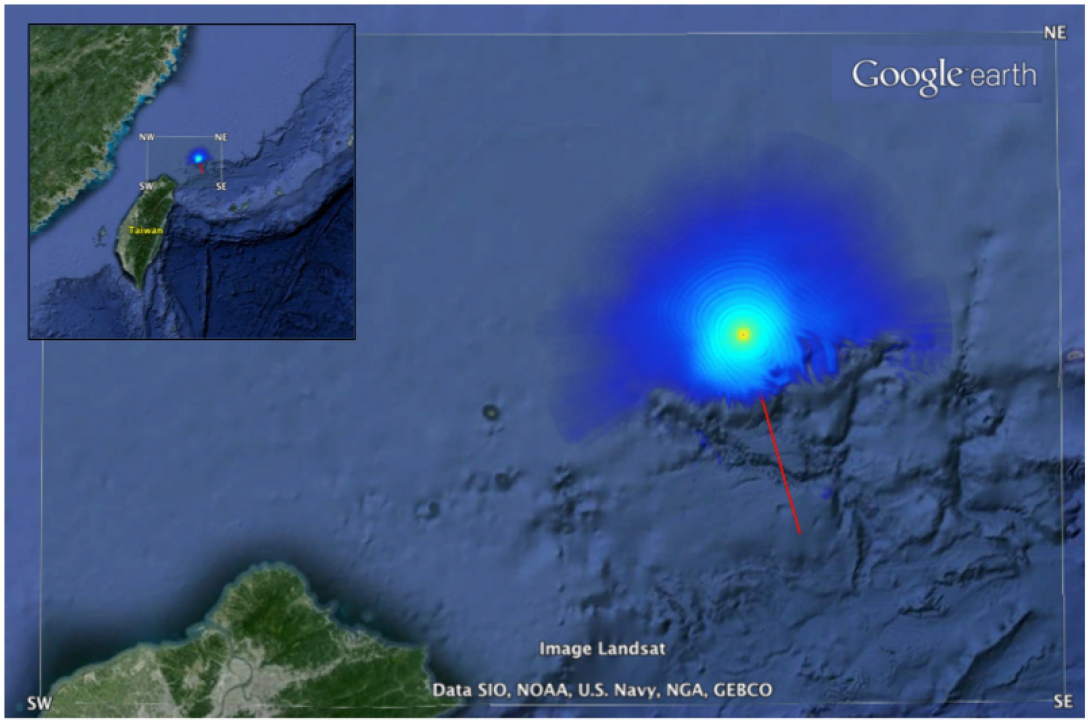

Figure 6-6: 3D Acoustic Propagation Along Shelf-Break Region Above -90 dB

to the interaction with the steep bathymetry along the North Mein-Hua canyon. A full ensemble of 3D acoustic propagation plots are generated to be clustered and evaluated to determine regions of significant variation due to the ocean uncertainty.

Additionally, a second ensemble was generated with the epicenter of the propagation originating from the same location that was used for the source of the upslope 2D propagation slice. The 3D acoustic field propagates primarily up the slope of the North Mein-Hua canyon and is displayed in Figure 6-7. The transmission loss is again plotted using a transceiver depth of 100 m with a limiting background level of -120 dB in Figure 6-7 and -90 dB in Figure 6-8.

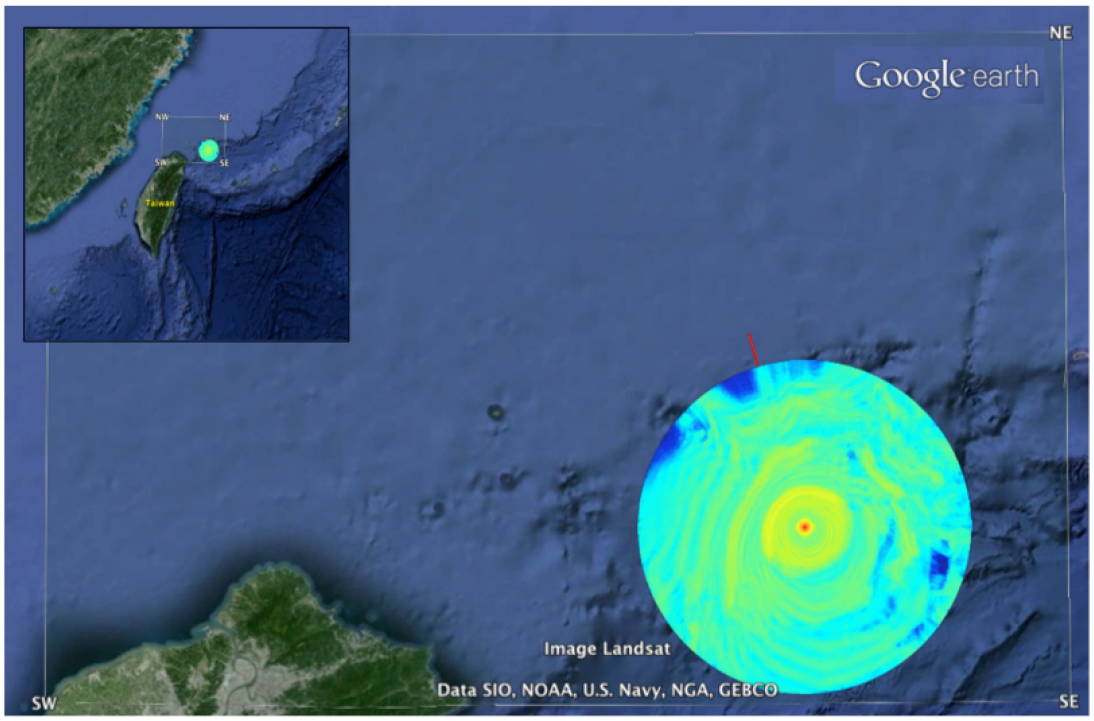

Figure 6-7: Upslope 3D Acoustic Propagation Along Shelf-Break Region

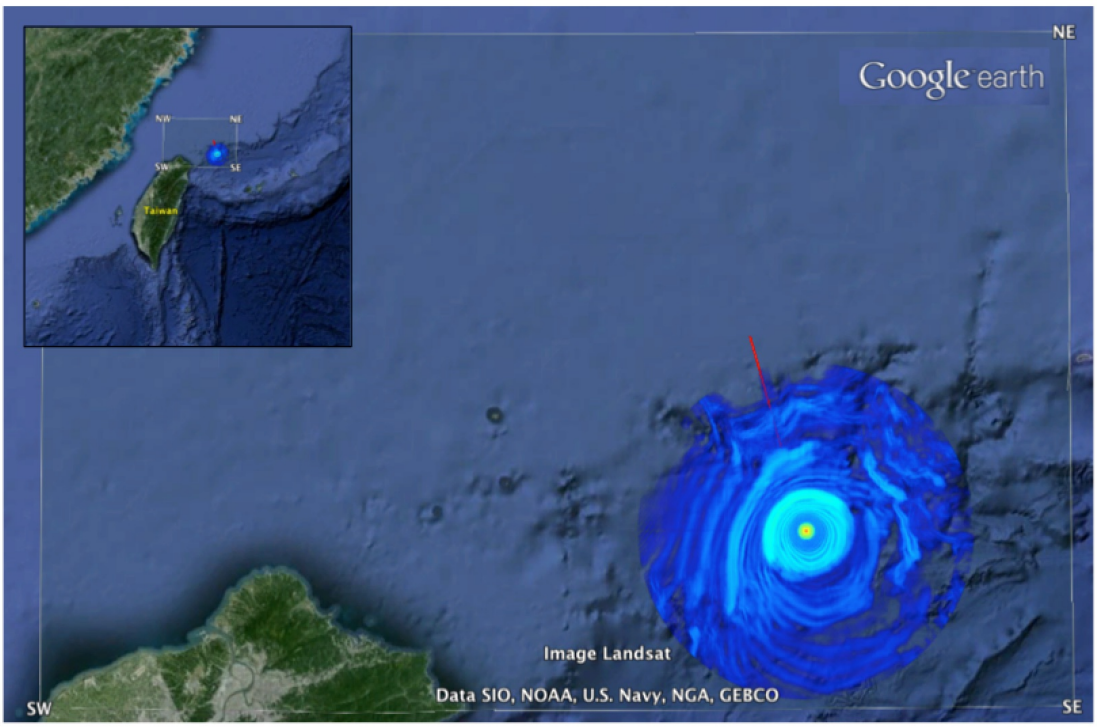

Figure 6-8: Upslope 3D Acoustic Propagation Along Shelf-Break Region Above -90 dB

The horizontal transmission loss profile ensembles can be clustered to identify areas of variation due to the uncertainties in the ocean field. These clustered transmission loss profiles generated from the ensembles can be used to identify regions of higher or lower transmission loss and their probability of occurrence can enhance the understanding of the potential acoustic fields that are contained within the forecast ocean field ensembles.

6.3 Coupled 4D Ocean Field and 3D Acoustic Field Uncertainty Evaulation

6.3.1 3D Acoustic Clusters

The acoustic fields for the 3D downslope propagation were analyzed and clustered using the same technique that was used to cluster the 2D acoustic slices. The k-means algorithm was used and again a k-value of 3 was used to generate representative clusters of the data. Each of the 3 clusters can be seen in the plots displayed in Figure 6-9. The transmission loss plots are depicted by a 3D representation in the upper

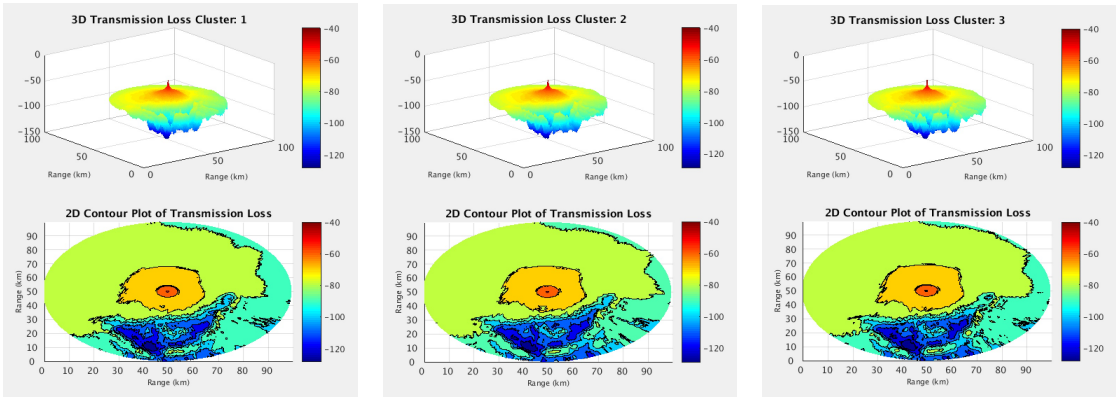

(a) Cluster 1 (b) Cluster 2 (c) Cluster 3

Figure 6-9: Transmission Loss Cluster Plots

subplot and by a contour plot in the lower subplot of Figure 6-9. The variations between plots can be identified through close inspection of these figures. However, to more easily highlight the variations generated between the clusters a set of difference

plots are used.

6.3.2 Cluster Difference Plots

The clustered difference plots highlight the range in transmission loss that can be generated by the ocean uncertainty within the ensembles. The cluster difference plots show the range in decibels of transmission loss between clusters. Additionally, the difference plots show the variation for the given transition from one cluster to another and highlights the expected variations. The three cluster difference plots for the downslope propagation can be seen in Figure 6-10.

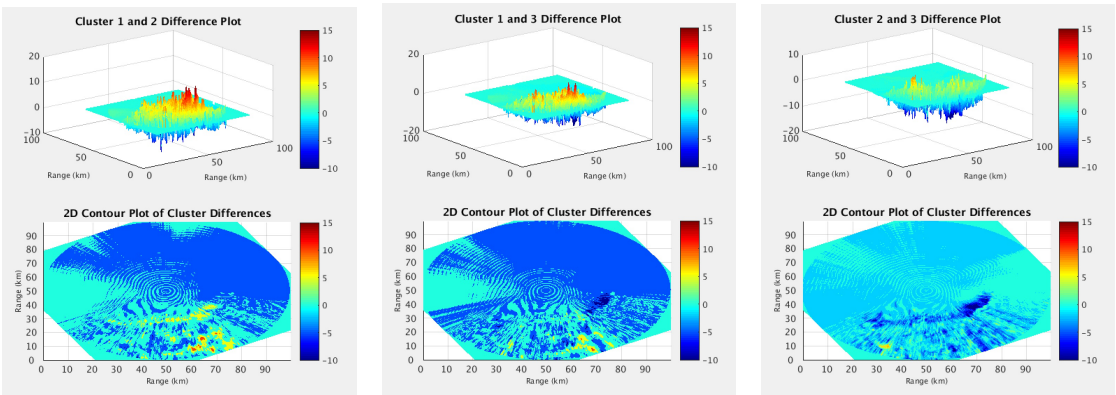

(a) Clusters 1 and 2 (b) Clusters 1 and 3 (c) Clusters 2 and 3

Figure 6-10: Cluster Difference Plots

The difference plots show that range in transmission loss levels between two clusters varies from approximately -10 dB to +15 dB. The regions of peak variability differs from one cluster to another. Therefore, the probability of detection may be significantly affected in those regions. The differences between clusters 1 and 2 shown in plot (a) identify several regions of higher transmission loss levels, which would indicate an increased probability of detection in those regions. When compared to the differences between clusters 2 and 3 in plot (c) there are predominantly regions of reduced transmission loss, which would indicate a reduced risk of detection for a transition from cluster 2 to 3. To represent the variations in probability of detection the 3D acoustic fields will be used to generate both a Gaussian probability of detection plot and a clustered probability of detection plot to highlight the regions of

variation in the acoustic fields with increased fidelity.

6.3.3 3D Gaussian Probability of Detection Plots

The first probability of detection plots are generated using a Gaussian representation of the entire ensemble generated from the ocean acoustic fields. Again at a transceiver depth of 100 m and a frequency of 150 hz the transmission loss of the acoustic field ensembles that were generated from the forecast 4D ocean fields are used to generate a Gaussian distribution at each grid point. The background noise is assumed to be a constant level for the entire region, although this is not necessary. Various background noise profiles could be utilized; however, these examples are only displayed with constant noise level of -80 dB, -90 dB and -100 dB. If the transmission loss for all fields in the ensemble are greater than the noise level then a probability of detection is assumed to be greater than 95%. For regions where only some of the acoustic fields generated in the Gaussian probability distribution then they are weighted by their percentage to determine a more accurate probability of detection in that region. The probability of detection plots for the various background noise levels can be seen in Figure 6-11. The benefit of using the ensemble of ocean acoustic fields is

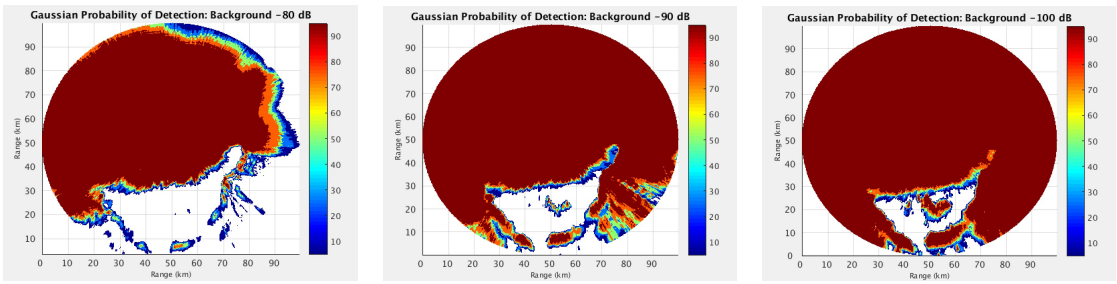

(a) Background -80 dB (b) Background -90 dB (c) Background -100 dB

Figure 6-11: 3D Gaussian Probability of Detection Plots

easily seen in the Probability of Detection plots. For example, in subplot (a) of Figure 6-11 there are regions ranging up to 15 km along the eastern boundary where the probability of detection is variable based on the distribution generated from the ensembles. For a single deterministic run this range of possible detection would not be identified. Therefore, this example provides an increased fidelity to show regions

where variations in the ocean field may alter the state of the acoustic field enough to have implications on the detectability of a target. This same process was completed using the clustered fields in lieu of the Gaussian probability distributions.

6.3.4 3D Clustered Probability of Detection Plots

The 3D acoustic fields were clustered as shown in section 6.3.1. These clusters each have an expected probability based on the acoustic field ensembles. The future cluster probabilities can also be estimated based on the cluster transition matrices. The probabilities can be used to determine the probability of detection in the same manner as the Gaussian probability distribution method. The regions where all cluster transmission loss values are above the background noise level then the expected probability of detection is assumed to be greater than 95%. If less then the maximum number of clusters and greater than one cluster are above the background noise level then the probability of detection is determined based on the summation of the expected probability of occurrence of those clusters. For the example generated from the test data, which have been divided into three clusters, the expected probability of detection plots are displayed in Figure 6-12. The clustered probability of detection

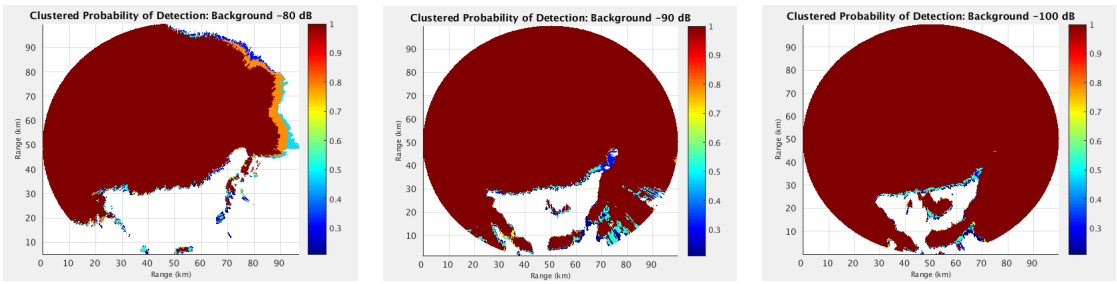

(a) Background -80 dB (b) Background -90 dB (c) Background -100 dB

Figure 6-12: 3D Clustered Probability of Detection Plots

plots represent the same general regions where the variable detection probabilities exist. The clusters do not provide the same level of fidelity as the Gaussian representation; however, they do capture the major regions where the variability in the acoustic field is changing. To increase the fidelity of the variations of the clustered plots a greater number of clusters could be used. This method could also be employed

in regions where greater variability is expected. For example, in regions surrounding steep bathymetric features or, large gradients in the ocean parameters then a greater number of clusters could be employed to better resolve those features.

Chapter 7

Conclusion

The ocean is a complex medium for sound propagation. Accurately modeling the nonlinear multi-scale processes of the ocean is an area of continued research and progress. Progress in the development of coupled ocean acoustic propagation models is also an ongoing endeavor, which has seen large advances due to the development of supercomputer technology to facilitate large scale computing. The coupled 4D ocean modeling with 3D acoustic propagation was performed and analyzed to better understand the transmission of uncertainties from the ocean field to the resulting acoustic transmission loss fields. This research has demonstrated the effects of ocean variability in complex littoral regions and how this can generate significant effects on the acoustic propagation in the region. This variability can alter the acoustic transmission loss in certain dynamic regions by greater than 20 dB. An acoustic propagation variability of this magnitude and occurring over long ranges can have impacts on the probability of detection and knowledge of regions that exhibit this variation may be beneficial for operational planning.

Uncertainty in the ocean fields is generated due to the nonlinearities and multi-scale processes that cannot be fully represented by the mathematical models. Data assimilation techniques and stochastic forcing of the models are helpful in accounting for these uncertain processes. The generation of an ensemble of ocean fields can be used to more adequately simulate the range of possible ocean states that may develop in the forecast models. Employing the MIT Multidisciplinary Environmental

Assimilation System (MSEAS) primitive equation ocean model, and generating an ensemble of forecast ocean states using the Error Subspace Statistical Estimation scheme (ESSE) the uncertainty in the ocean state was able to be captured and used to generate the 3D uncertain acoustic field ensembles. The ensembles of 3D acoustic transmission loss fields can then be represented by using the clustered reduced order techniques.

The cluster based reduced order modeling was employed to generate reduced order representative states that can be used to evaluate the effects of the uncertainty within the ensembles that were generated. The optimized k-means clustering algorithm was used to determine the representative reduced order acoustic transmission loss fields. This analysis was performed initially for the 2D acoustic field slices and then modified to enable clustering of 3D acoustic fields. Once the cluster centroids were identified, temporal relationships between the cluster transitions were modeled as a Markov process. The probability of expected cluster transitions was represented by a cluster transition matrix to provide a representation of the forecast acoustic field. With the model of the forecast acoustic field developed these were applied to generate enhanced probability of detection plots in the 2D and 3D cases.

The probability of detection plots were generated using the acoustic field ensembles that represented the uncertainty of the ocean state. The benefit gained by including the uncertain fields is best seen in the region along the shelf-break zone. Complex bathymetry and areas of high ocean field variation due to currents and multi-scale process interactions generated the largest fluctuations in the acoustic field. These regions could produce acoustic transmission loss variations of up to 20 dB that ranged over 5-10 km. A completely deterministic model would not adequately represent the acoustic state in these regions and the increased fidelity provided by incorporating the uncertain fields may be useful for operational planning. The 2D slice uncertain acoustic fields highlighted critical areas where the ranges of the acoustic field was either above or below a critical signal to noise ratio. The 3D probability of detection plots highlighted zones where certain clusters represent much higher peak acoustic levels or zones of increased loss. The fidelity of these probability of detection could

be further increased in future work.

The methods of ensemble analysis using cluster based reduced order modeling could be improved a number of ways. First, increasing the ensemble size would provide more accurate results. The acoustic ensemble could also be generated at shorter time intervals to further study and evaluate the temporal evolution of the uncertainty. For instance, the effects of internal waves on the acoustic field uncertainty would require a much shorter time window, but these same techniques could be applied to analyze possible ocean acoustic effects. Second, the clusters were optimized across the full range, which may not provide adequate fidelity at certain ranges that exhibit large ocean field variations and multiple acoustic modes are generated. To overcome this challenge the heuristic approach of determining the optimal k-value to cluster the data could be partitioned at various ranges in the 2D case or for certain zones in the 3D example. These regions could be determined based on a certain critical bathymetric slope or based on critical sound speed variability to trigger the heuristically determined k-value to be recomputed in those ranges. This method would enable regions of high variability to ensure the clustered reduced order model accurately captures the various modes that are present.

The methods and techniques studied in this research can be used to assess the forecast probabilities of the performance of systems that operate in the complex ocean environment. Increased computing capability will facilitate more advanced studies to be completed in the ocean acoustic field. The continued study and development of improved ocean models will provide more accurate simulations. Additionally, advances in stochastic modeling of the ocean and acoustic propagation will also improve capability to quantify uncertainties in these highly complex non-linear systems. The need to continue to improve understanding and ascertain the interaction of ocean acoustics uncertainties will continue to increase as the importance of unmanned underwater systems continues to develop and the relevance of the complex littoral ocean regions is continuing to grow. The development of advanced ocean acoustic navigation systems, acoustic countermeasures and acoustic communications systems deployed in complex ocean regions will greatly benefit from an enhanced understanding of the

uncertainties in the acoustic environment. These factors will drive future advances in coupled ocean acoustic modeling and further studies will continue to progress the ocean acoustic field of study.

Appendix A

Method of Runs

A.1 2D Acoustic Slice Run Commands

```
./peregrine lon 122d48m44s lat 25d22m50s bearing 344d
range_limits 0,55e3 depth_limits 0,-1500 tx_depth -100 fc
150 time 20090904T210000Z path_water ../envs/mseas01.oof

cat out.obb | tenlog | flipdim 0|transpose| obb2imageeps
climit -110,-50 ylimit 2,0 ytick -1 xlimit 0,50 xlabel
'Range (km)' ylabel 'Depth (m)' title 'Environment 1
Time 1' show_colorbar 1 ctick 10 > env_01_time_01.eps

./peregrine lon 122d48m44s lat 25d22m50s bearing 344d
range_limits 0,55e3 rx_depth -100 depth_extent 10
tx_depth -100 fc 150 path_output single_depth.obb
path_output_range range.obb

cat single_depth.obb | tenlog | interleave range.obb
/dev/stdin | obb2lineeps xdatascale 6371 ylimit -114,-60
ytick 6 title 'TL vs Range' xlabel 'Range (km)' ylabel
'TL (dB)' > tl_vs_range.eps
```

A.2 3D Acoustic Run Commands

```
set peregrine_home="/file_location "
set peregrine_data="$peregrine_home/envs"
set peregrine_bin="$peregrine_home/peregrine"

$peregrine_bin/peregrine fc 150 time 20090904T210000Z rx_depth
-100 depth_extent 120 ppwx 2 pade_terms_horizontal 2 pixels 720
lon 122d40m52s lat 25d47m41s range 50e3 tx_depth -100
path_water ${peregrine_data}/mseas$1.oof path_seafloor
${peregrine_data}/etopo.oof sediment_phi 5 path_output out.obb

cat out.obb | trim 0 0 1 | mergedims 0 | tenlog | obb2kmz
climit -90,-30 lonlimit 122.182d,123.181d latlimit
25.3451d,26.2444d

cat out.obb | tenlog | obb2dms > output_file_name$1.txt

sed -i -e 's/;/ /g' output_file_name $1.txt

sed -i -e 's/-inf/NaN/g' output_file_name $1.txt
```

Bibliography

Abbot, P. and Dyer, I. (2002). Sonar performance predictions incorporating environmental variability. In *Impact of Littoral Environmental Variability of Acoustic Predictions and Sonar Performance*, pages 611–618. Springer.

Amante, C. and Eakins, B. W. (2009). ETOPO1 1 arc-minute global relief model: procedures, data sources and analysis. Colorado: US Department of Commerce, National Oceanic and Atmospheric Administration, National Environmental Satellite, Data, and Information Service, National Geophysical Data Center, Marine Geology and Geophysics Division.

Bachman, R. T. (1985). Acoustic and physical property relationships in marine sediment. *The Journal of the Acoustical Society of America*, 78(2):616–621.

Berkooz, G., Holmes, P., and Lumley, J. L. (1993). The proper orthogonal decomposition in the analysis of turbulent flows. *Annual review of fluid mechanics*, 25(1):539–575.

Byfield, V. (2016). Current Map, National Oceanography Center, Southampton. Retrieved From http://www.seos-project.eu/modules/oceancurrents/oceancurrents-c02-p04.html//.

Chapra, S. C. and Canale, R. P. (1998). *Numerical methods for engineers*, volume 2. McGraw-Hill.

Chiu, L., Chang, A., Lin, Y.-T., and Liu, C.-S. (2015). Estimating geoacoustic properties of surficial sediments in the North Mien-Hua canyon region with a chirp sonar profiler. *Oceanic Engineering, IEEE Journal of*, 40(1):222–236.

Cococcioni, M., Lazzerini, B., and Lermusiaux, P. (2015). Adaptive sampling using fleets of underwater gliders in the presence of fixed buoys using a constrained clustering algorithm. In *Proceedings of IEEE OCEANS'15 Conference*, Genoa. IEEE.

Colin, M. E. G. D., Duda, T. F., te Raa, L. A., van Zon, T., Haley, Jr., P. J., Lermusiaux, P. F. J., Leslie, W. G., Mirabito, C., Lam, F. P. A., Newhall, A. E., Lin, Y.-T., and Lynch, J. F. (2013). Time-evolving acoustic propagation modeling in a complex ocean environment. In *OCEANS - Bergen, 2013 MTS/IEEE*, pages 1–9.

Collins, M. D. and Westwood, E. K. (1991). A higher-order energy-conserving parabolic equqation for range-dependent ocean depth, sound speed, and density. *The Journal of the Acoustical Society of America*, 89(3):1068–1075.

Coppens, A. B. (1981). Simple equations for the speed of sound in neptunian waters. *The Journal of the Acoustical Society of America*, 69(3):862–863.

Crocker, M. J. (1998). *Handbook of acoustics*. John Wiley & Sons.

Cushman-Roisin, B. and Beckers, J.-M. (2011). *Introduction to geophysical fluid dynamics: physical and numerical aspects*, volume 101. Academic Press.

Davis, J. (2016). Great Southern Route, Third Edition, East Asian Weather Conditions. Weather Routing, Inc. Retrieved from http://greatsouthernroute.com/weather-routing/east-asian-weather-conditions//.

Duda, T. F., Lin, Y.-T., Newhall, A. E., Helfrich, K. R., Zhang, W. G., Badiey, M., Lermusiaux, P. F. J., Colosi, J. A., and Lynch, J. F. (2014a). The "Integrated Ocean Dynamics and Acoustics" (IODA) hybrid modeling effort. In *Proceedings of the international conference on Underwater Acoustics - 2014 (UA2014)*, pages 621–628.

Duda, T. F., Lin, Y.-T., Zhang, W., Cornuelle, B. D., and Lermusiaux, P. F. J. (2011). Computational studies of three-dimensional ocean sound fields in areas of complex seafloor topography and active ocean dynamics. In *Proceedings of the 10th International Conference on Theoretical and Computational Acoustics*, Taipei, Taiwan.

Duda, T. F., Zhang, W. G., Helfrich, K. R., Newhall, A. E., Lin, Y.-T., Lynch, J. F., Lermusiaux, P. F. J., Haley, Jr., P. J., and Wilkin, J. (2014b). Issues and progress in the prediction of ocean submesoscale features and internal waves. In *OCEANS'14 MTS/IEEE*.

Emerson, C., Lynch, J. F., Abbot, P., Lin, Y.-T., Duda, T. F., Gawarkiewicz, G. G., and Chen, C.-F. (2015). Acoustic propagation uncertainty and probabilistic prediction of sonar system performance in the southern east china sea continental shelf and shelfbreak environments. *Oceanic Engineering, IEEE Journal of*, 40(4):1003–1017.

Etter, P. C. (2013). *Underwater acoustic modeling and simulation*. CRC Press.

Ferla, C., Porter, M., and Jensen, F. (1993). C-snap: Coupled saclantcen normal mode propagation loss model. *Memorandum SM-274, SACLANTCEN Undersea Research Center, La Spezia, Italy*.

Gawarkiewicz, G., Bahr, F., Beardsley, R. C., and Brink, K. H. (2001). Interaction of a slope eddy with the shelfbreak front in the middle atlantic bight. *Journal of Physical Oceanography*, 31(9):2783–2796.

Gawarkiewicz, G., Jan, S., Lermusiaux, P. F. J., McClean, J. L., Centurioni, L., Taylor, K., Cornuelle, B., Duda, T. F., Wang, J., Yang, Y. J., Sanford, T., Lien, R.-C., Lee, C., Lee, M.-A., Leslie, W., Haley, Jr., P. J., Niiler, P. P., Gopalakrishnan, G., Velez-Belchi, P., Lee, D.-K., and Kim, Y. Y. (2011). Circulation and intrusions northeast of Taiwan: Chasing and predicting uncertainty in the cold dome. *Oceanography*, 24(4):110–121.

Gay, D. H. and Ray, W. H. (1995). Identification and control of distributed parameter systems by means of the singular value decomposition. *Chemical Engineering Science*, 50(10):1519–1539.

Ghanem, R. G. and Spanos, P. D. (1991). Spectral stochastic finite-element formulation for reliability analysis. *Journal of Engineering Mechanics*, 117(10):2351–2372.

Goff, J. A., Abbot, P., Lynch, J. F., and Hodgkiss, W. S. (2006). Guest editorial capturing uncertainty in the tactical ocean environment. *Oceanic Engineering, IEEE Journal of*, 31(2):245–248.

Griffies, S. M. and Adcroft, A. J. (2008). Formulating the equations of ocean models. *Ocean Modeling in an Eddying Regime*, pages 281–317.

Haley, P. J. and Lermusiaux, P. F. (2010). Multiscale two-way embedding schemes for free-surface primitive equations in the multidisciplinary simulation, estimation and assimilation system. *Ocean dynamics*, 60(6):1497–1537.

Haley, Jr., P. J., Agarwal, A., and Lermusiaux, P. F. J. (2015). Optimizing velocities and transports for complex coastal regions and archipelagos. *Ocean Modeling*, 89:1–28.

Hardin, R. and Tappert, F. (1973). Applications of the split-step fourier method to the numerical solution of nonlinear and variable coefficient wave equations. *Siam Rev*, 15(2):423.

Heaney, K. D. and Campbell, R. L. (2013). Measurement and modeling of deep water ocean acoustics. Technical report, DTIC Document.

Heaney, K. D. and Cox, H. (2006). A tactical approach to environmental uncertainty and sensitivity. *Oceanic Engineering, IEEE Journal of*, 31(2):356–367.

Hovem, J. M. and Ingram, G. D. (1979). Viscous attenuation of sound in saturated sand. *The Journal of the Acoustical Society of America*, 66(6):1807–1812.

Jensen, F. and Krol, H. (1975). The use of the parabolic equation method in sound propagation modelling. SACLANT ASW Res. Ctr, Memo. SM-72.

Jensen, F. B., Kuperman, W. A., Porter, M. B., and Schmidt, H. (2011). *Computational ocean acoustics*. Springer Science & Business Media.

Jones, R. M., Riley, J. P., and Georges, T. M. (1986). HARPO: A versatile three-dimensional Hamiltonian ray-tracing program for acoustic waves in an ocean with irregular bottom. NOAA Wave Propagation Laboratory, Boulder, Colorado.

Kaiser, E., Noack, B. R., Cordier, L., Spohn, A., Segond, M., Abel, M., Daviller, G., Östh, J., Krajnović, S., and Niven, R. K. (2014). Cluster-based reduced-order modelling of a mixing layer. *Journal of Fluid Mechanics*, 754:365–414.

Krumbein, W. C. and Sloss, L. L. (1951). Stratigraphy and sedimentation. *Soil Science*, 71(5):401.

Kuperman, W. and Roux, P. (2007). Underwater acoustics. In *Springer Handbook of Acoustics*, pages 149–204. Springer.

Lam, F.-P. A., Haley, P. J., Janmaat, J., Lermusiaux, P. F., Leslie, W. G., Schouten, M. W., te Raa, L. A., and Rixen, M. (2009). At-sea real-time coupled four-dimensional oceanographic and acoustic forecasts during battlespace preparation 2007. *Journal of Marine Systems*, 78:S306–S320.

Landry, J. J. (2014). Coastal Ocean Variability off the Coast of Taiwan in Response to Typhoon Morakot: River Forcing, Atmospheric Forcing, and Cold Dome Dynamics. Master's thesis, Massachusetts Institute of Technology, Department of Mechanical Engineering, Cambridge, Massachusetts.

Leontovich, M. and Fock, V. (1946). Solution of propagation of electromagnetic waves along the earth's surface by the method of parabolic equations. *J. Phys. Ussr*, 10(1):13–23.

Lermusiaux, P. F. (1997). *Error subspace data assimilation methods for ocean field estimation: theory, validation and applications*. Harvard University.

Lermusiaux, P. F. (2006). Uncertainty estimation and prediction for interdisciplinary ocean dynamics. *Journal of Computational Physics*, 217(1):176–199.

Lermusiaux, P. F., Chiu, C.-S., Gawarkiewicz, G. G., Abbot, P., Robinson, A. R., Miller, R. N., Haley, P. J., Leslie, W. G., Majumdar, S. J., Pang, A., et al. (2006). Quantifying uncertainties in ocean predictions. Technical report, DTIC Document.

Lermusiaux, P. F., Evangelinos, C., Tian, R., Haley, P. J., McCarthy, J., Patrikalakis, N. M., Robinson, A. R., and Schmidt, H. (2004). Adaptive coupled physical and biogeochemical ocean predictions: A conceptual basis. In *Computational Science-ICCS 2004*, pages 685–692. Springer.

Lermusiaux, P. F. and Robinson, A. (1999). Data assimilation via error subspace statistical estimation. part i: Theory and schemes. *Monthly Weather Review*, 127(7):1385–1407.

Lermusiaux, P. F., Xu, J., Chen, C.-F., Jan, S., Chiu, L. Y., and Yang, Y.-J. (2010). Coupled ocean–acoustic prediction of transmission loss in a continental shelfbreak region: Predictive skill, uncertainty quantification, and dynamical sensitivities. *Oceanic Engineering, IEEE Journal of*, 35(4):895–916.

Lermusiaux, P. F. J. (2006). Uncertainty estimation and prediction for interdisciplinary ocean dynamics. *Journal of Computational Physics*, 217(1):176–199.

Lermusiaux, P. F. J. and Chiu, C.-S. (2002). Four-dimensional data assimilation for coupled physical-acoustical fields. In Pace, N. G. and Jensen, F. B., editors, *Acoustic Variability, 2002*, pages 417–424, Saclantcen. Kluwer Academic Press.

Lermusiaux, P. F. J., Chiu, C.-S., Gawarkiewicz, G. G., Abbot, P., Robinson, A. R., Miller, R. N., Haley, Jr, P. J., Leslie, W. G., Majumdar, S. J., Pang, A., and Lekien, F. (2006). Quantifying uncertainties in ocean predictions. *Oceanography*, 19(1):92–105.

Lermusiaux, P. F. J., Chiu, C.-S., and Robinson, A. R. (2002). Modeling uncertainties in the prediction of the acoustic wavefield in a shelfbreak environment. In Shang, E.-C., Li, Q., and Gao, T. F., editors, *Proceedings of the 5th International conference on theoretical and computational acoustics*, pages 191–200. World Scientific Publishing Co. Refereed invited manuscript.

Lin, Y.-T., Newhall, A. E., Duda, T. F., Lermusiaux, P. F. J., and Haley, P. J. (2010). Merging multiple-partial-depth data time series using objective empirical orthogonal function fitting. *IEEE Journal of Oceanic Engineering*, 35(4):710–721.

Lloyd, S. (1957). Last square quantization in pcm's. *Bell Telephone Laboratories Paper*.

Lovett, J. R. (1978). Merged seawater sound-speed equations. *The Journal of the Acoustical Society of America*, 63(6):1713–1718.

Lynch, J., Gawarkiewicz, G., Chiu, C., Pickart, R., Miller, J., Smith, K., Robinson, A., Brink, K., Beardsley, R., Sperry, B., et al. (1997). Shelfbreak primer - an integrated acoustic and oceanographic field study in the mid-atlantic bight. *Shallow-Water Acoustics*, pages 205–212.

Mackenzie, K. V. (1981). Nine-term equation for sound speed in the oceans. *The Journal of the Acoustical Society of America*, 70(3):807–812.

Mirabito, C., Haley, Jr., P. J., Lermusiaux, P. F. J., and Leslie, W. G. (2012). A River Discharge Model for Coastal Taiwan during Typhoon Morakot. MSEAS Report 13, Department of Mechanical Engineering, Massachusetts Institute of Technology, Cambridge, MA.

Nihoul, J. and Djenidi, S. (1998). *Coupled physical, chemical and biological models*. J. Wiley and Sons.

Östh, J., Kaiser, E., Krajnović, S., and Noack, B. R. (2015). Cluster-based reduced-order modelling of the flow in the wake of a high speed train. *Journal of Wind Engineering and Industrial Aerodynamics*, 145:327–338.

Rixen, M., Lermusiaux, P. F. J., and Osler, J. (2012). Quantifying, predicting, and exploiting uncertainties in marine environments. *Ocean Dynamics*, 62(3):495–499.

Robinson, A. R., Abbot, P., Lermusiaux, P. F. J., and Dillman, L. (2002). Transfer of uncertainties through physical-acoustical-sonar end-to-end systems: A conceptual basis. In Pace, N. G. and Jensen, F. B., editors, *Acoustic Varibility, 2002*, pages 603–610. SCLANTCEN, Kluwer Academic Press.

Robinson, A. R. and Lermusiaux, P. F. (2002). Data assimilation for modeling and predicting coupled physical–biological interactions in the sea. *The sea*, 12:475–536.

Robinson, A. R. and Lermusiaux, P. F. J. (2004). Prediction systems with data assimilation for coupled ocean science and ocean acoustics. In Tolstoy et al, A., editor, *Proceedings of the Sixth International Conference on Theoretical and Computational Acoustics*, pages 325–342. World Scientific Publishing. Refereed invited Keynote Manuscript.

Rudnick, D. L., Jan, S., Centurioni, L., Lee, C. M., Lien, R.-C., Wang, J., Lee, D.-K., Tseng, R.-S., Kim, Y. Y., and Chern, C.-S. (2011). Seasonal and mesoscale variability of the kuroshio near its origin. *Oceanography*.

Sapsis, T. P. and Lermusiaux, P. F. (2009). Dynamically orthogonal field equations for continuous stochastic dynamical systems. *Physica D: Nonlinear Phenomena*, 238(23):2347–2360.

Sapsis, T. P. and Lermusiaux, P. F. (2012). Dynamical criteria for the evolution of the stochastic dimensionality in flows with uncertainty. *Physica D: Nonlinear Phenomena*, 241(1):60–76.

Shmueli, G., Patel, N. R., and Bruce, P. C. (2007). *Data mining for business intelligence: concepts, techniques, and applications in Microsoft Office Excel with XLMiner*. John Wiley & Sons.

Smith, K. B., Miller, C. W., D'Agostino, A. F., Sperry, B., Miller, J. H., and Potty, G. R. (2002). Three-dimensional propagation effects near the mid-atlantic bight shelf break (l). *The Journal of the Acoustical Society of America*, 112(2):373–376.

Tappert, F. D. (1977). The parabolic approximation method. In *Wave propagation and underwater acoustics*, pages 224–287. Springer.

Task Force, A. S. W. (2004). Anti-submarine warfare concept of operations for the 21 st century.

Thomson, D. and Chapman, N. (1983). A wide-angle split-step algorithm for the parabolic equation. *The Journal of the Acoustical Society of America*, 74(6):1848–1854.

Tibshirani, R., Walther, G., and Hastie, T. (2001). Estimating the number of clusters in a data set via the gap statistic. *Journal of the Royal Statistical Society: Series B (Statistical Methodology)*, 63(2):411–423.

Trauth, M. H., Gebbers, R., Marwan, N., and Sillmann, E. (2007). *MATLAB recipes for earth sciences*, volume 34. Springer.

Ueckermann, M. P., Lermusiaux, P., and Sapsis, T. (2011). *Numerical schemes and computational studies for dynamically orthogonal equations*. PhD thesis, Department of Mechanical Engineering, Massachusetts Institute of Technology.

Wang, D., Lermusiaux, P. F., Haley, P. J., Eickstedt, D., Leslie, W. G., and Schmidt, H. (2009). Acoustically focused adaptive sampling and on-board routing for marine rapid environmental assessment. *Journal of Marine Systems*, 78:S393–S407.

Xiu, D. and Karniadakis, G. E. (2002). The wiener–askey polynomial chaos for stochastic differential equations. *SIAM journal on scientific computing*, 24(2):619–644.

Xu, J., Lermusiaux, P. F. J., Haley Jr., P. J., Leslie, W. G., and Logutov, O. G. (2008). Spatial and Temporal Variations in Acoustic propagation during the PLUSNet-07 Exercise in Dabob Bay. In *Proceedings of Meetings on Acoustics (POMA)*, volume 4, page 11. Acoustical Society of America 155th Meeting.

Zabusky, N. J. (1987). Grappling with complexity. *Physics Today*, 40:25–27.

Ziomek, L. (1994). *Fundamentals of acoustic field theory and space-time signal processing*. CRC press.